

NASA  
CR  
61928  
v. 1  
c. 1

N69-33448

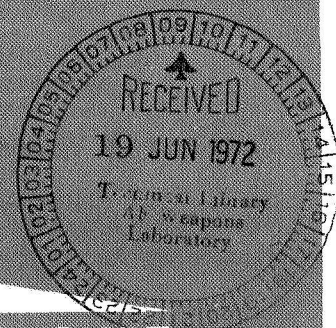
STUDY OF INDICIAL AERODYNAMIC FORCES ON MUL-  
TISTAGE SPACE VEHICLE SYSTEMS - VOLUME I -  
APPLICATION OF THEORY TO BASIC GEOMETRIES AND  
TO THE SATURN V

William D. Glauz, et al

September 1968

LOAN COPY: RETURN  
AFWL (DOUL)  
KIRTLAND AFB, N. M.

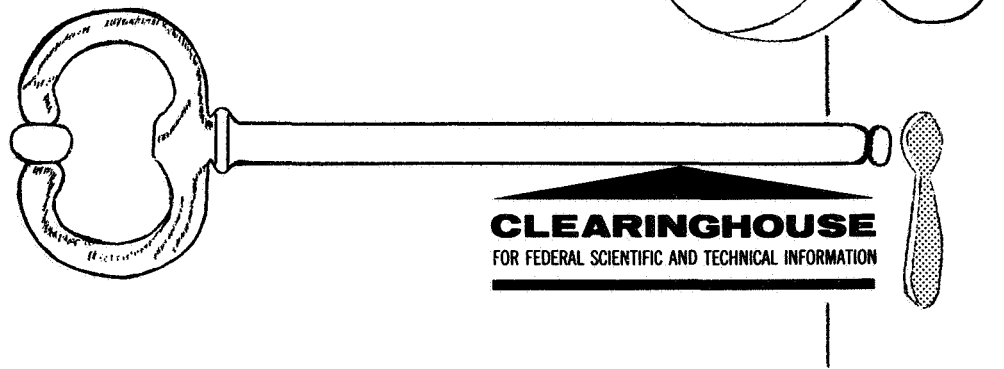
TECH LIBRARY KAFB, NM  
006254J



DISTRIBUTED BY: **CLEARINGHOUSE**  
FOR FEDERAL SCIENTIFIC AND TECHNICAL INFORMATION



# YOUR KEY...



*to scientific and technical advancement*

Mr. Scientist. . . Engineer. . . Businessman. . . the Clearinghouse for Scientific and Technical Information can serve as your key to progress in research and development. Each year, some 40,000 unclassified documents from more than 125 Government agencies enter our collection. The Clearinghouse announces, reproduces and sells these reports to the public at a nominal cost. To make this wealth of scientific and technical information readily available, we have tailored our services to meet the needs of the highly selective customer as well as the general user. Some of these services are listed below.

**U.S. GOVERNMENT RESEARCH AND DEVELOPMENT REPORTS (USGRDR).** This semimonthly journal abstracts approximately 40,000 new Government-sponsored reports and translations annually. Features a quick-scan format, cross references, edge index to subject fields, and a report locator list.

**U. S. GOVERNMENT RESEARCH AND DEVELOPMENT REPORTS INDEX (USGRDR-I).** Published concurrently with the USGRDR to index each issue by subject, personal author, corporate source, contract number and accession/report number. Quarterly Indexes and an Annual Cumulative also are available.

**CLEARINGHOUSE ANNOUNCEMENTS IN SCIENCE AND TECHNOLOGY.** A semimonthly current awareness announcement service in 46 separate categories representing complete coverage of all documents announced by the Clearinghouse. Highlights special interest reports.

**FAST ANNOUNCEMENT SERVICE (FAS).** Selective announcement service emphasizing commercial applications of report information. Covers approximately 10 percent of Clearinghouse document input. Compiled and mailed in 57 categories.

**SELECTIVE DISSEMINATION OF MICROFICHE (SDM).** Automatic distribution twice monthly of Government research and development reports on microfiche. Economical and highly selective. Several hundred categories from which to choose.

**ADDITIONAL INFORMATION** concerning these and other Clearinghouse services is available by writing to:

**Customer Services  
Clearinghouse  
U.S. Department of Commerce  
Springfield, Virginia 22151**



0062541

STUDY OF INDICIAL AERODYNAMIC FORCES  
ON MULTISTAGE SPACE VEHICLE SYSTEMS

VOLUME I

APPLICATION OF THEORY TO BASIC GEOMETRIES  
AND TO THE SATURN V

by

William D. Glauz  
Robert R. Blackburn



FINAL REPORT

28 June 1967 - 27 September 1968

Contract No. NAS8-21167

Control No. DCN 1-7-20085 S2(1F)

MRI Project No. 3089-P

FACILITY FORM 802	<b>N69-33448</b>	
	(ACCESSION NUMBER)	(THRU)
	119 (PAGES)	1 (CODE)
	CR-61928 (NASA CR OR TRX OR AD NUMBER)	01 (CATEGORY)

For

National Aeronautics and Space Administration  
George C. Marshall Space Flight Center  
Huntsville, Alabama 35812

Reproduced by the  
CLEARINGHOUSE  
for Federal Scientific & Technical  
Information Springfield Va. 22151

507-56087

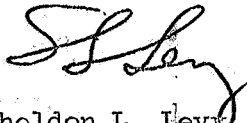
## PREFACE

This report was prepared by Midwest Research Institute under Contract No. NAS8-21167, "Study of Indicial Aerodynamic Forces on Multi-stage Space Vehicle Systems," for the George C. Marshall Space Flight Center of the National Aeronautics and Space Administration. The work was administered under the technical direction of the Aero-Astrodynamic Laboratory, George C. Marshall Space Flight Center, with Mr. Richard Beranek acting as Contracting Officer's Representative.

The authors wish to acknowledge the assistance of their co-workers, Mrs. Geraldine Coombs and Mr. W. Chauncey in parts of the analysis and programming. Also, the authors thank Mr. Donald Stout and the staff of the Computation Laboratory at the Marshall Space Flight Center who helped with the debugging and adapting of the programs to their data processing system.

Approved for:

MIDWEST RESEARCH INSTITUTE



Sheldon L. Levy, Director  
Mathematics and Physics Division

20 September 1968



TABLE OF CONTENTS

	<u>Page No.</u>
Nomenclature . . . . .	viii
Abstract . . . . .	x
I. Introduction . . . . .	1
A. Overview . . . . .	1
B. Report Organization. . . . .	3
II. Conclusions and Recommendations. . . . .	5
A. Conclusions. . . . .	5
B. Recommendations. . . . .	7
III. Review of Theory . . . . .	8
A. Formulation of Indicical Theory . . . . .	8
B. Integral Representation of Solution. . . . .	9
C. Linear (Gust Doublet) Solution . . . . .	12
D. Quadratic Solution . . . . .	13
E. "Corner" Solution. . . . .	14
F. Satisfaction of Boundary Conditions. . . . .	16
G. Aerodynamic Forces . . . . .	18
H. Equivalent Body Concept. . . . .	20
I. Duhamel Integral . . . . .	24
J. Stability Derivatives. . . . .	27
IV. Application to Simple Geometrical Shapes . . . . .	29
A. Introductory Remarks . . . . .	29
B. Cone Results . . . . .	30
C. Convex and Concave Parabolic Ogive Results . . . . .	41
D. Cone-Cylinder Results. . . . .	50
E. Ogive-Cylinder Results . . . . .	60
V. Frequency Response of Aerodynamic Forces for Saturn V. . .	71
VI. Response of Aerodynamic Forces on Saturn V to Inflight Winds. . . . .	84

TABLE OF CONTENTS (Continued)

	<u>Page No.</u>
Appendix I - Comparison of Aerodynamic Frequency Response Behavior with a Simple Spring-Mass Analogy . . .	89
Appendix II - Technique Used to Compute Wind Shear Data. . . . .	97
Bibliography . . . . .	108

List of Tables

<u>Table No.</u>	<u>Title.</u>	<u>Page No.</u>
I	Cone Angles Equivalent to Fin-Shroud Region . . . . .	24
II	Cone Configurations Examined. . . . .	30
III	$C_{N\alpha}$ Values for Various Cones at $M = 1.5$ . . . . .	35
IV	Cone-Cylinder Configurations Examined . . . . .	50
V	Ratios of Maximum Frequency Response to Zero-Frequency Response for Cone-Cylinders . . . . .	59
VI	Ratios of Maximum Frequency Response to Zero-Frequency Response for $\epsilon = 0.05$ Ogive-Cylinder. . . . .	67
VII	Wavelengths of Maximum Frequency Response of Total Normal Force for Saturn V . . . . .	76
VIII	Relative Response Amplitudes at Resonance for Saturn V . . . . .	77
IX	Frequency Response Type of Local Normal Forces for Selected Stations of Saturn V . . . . .	82
X	Saturn V Nominal Trajectory Data. . . . .	84



TABLE OF CONTENTS (Continued)

List of Figures

<u>Fig. No.</u>	<u>Title</u>	<u>Page No.</u>
1	Regions of Influence of Moving Point Source . . . . .	10
2	Representative Vehicle Showing Control Points . . . . .	17
3	Lift Distribution in Fin-Shroud Region at Mach Number 1.6 . . . . .	23
4	Steady-State Responses Versus Mach Number for Various Cone Angles . . . . .	32
5	Steady-State Slope of Normal Force Coefficient Versus Mach Number for $\epsilon = 0.05$ and $0.10$ Cones . . . . .	33
6	Aerodynamic Frequency Responses for a $2.87^\circ$ ( $\epsilon = 0.05$ ) Cone at $M = 1.5$ . . . . .	36
7	Aerodynamic Frequency Responses for a $5.72^\circ$ ( $\epsilon = 0.10$ ) Cone at $M = 1.5$ . . . . .	37
8	Aerodynamic Frequency Responses for a $10^\circ$ Cone at $M = 1.5$ . . . . .	38
9	Aerodynamic Frequency Responses for a $20^\circ$ Cone at $M = 1.5$ . . . . .	39
10	Aerodynamic Frequency Responses for a $30^\circ$ Cone at $M = 1.5$ . . . . .	40
11	Aerodynamic Frequency Responses for a $10^\circ$ Cone at Various Mach Numbers . . . . .	42
12	Steady-State Responses Versus Mach Number for $\epsilon = 0.05$ and $0.10$ Convex Ogives . . . . .	43
13	Steady-State Responses Versus Mach Number for $\epsilon = 0.05$ and $0.10$ Concave Ogives . . . . .	44
14	Aerodynamic Frequency Responses for an $\epsilon = 0.05$ Convex Ogive at $M = 1.5$ and $3.0$ . . . . .	46
15	Aerodynamic Frequency Responses for an $\epsilon = 0.10$ Convex Ogive at $M = 1.5$ and $3.0$ . . . . .	47
16	Aerodynamic Frequency Responses for an $\epsilon = 0.05$ Concave Ogive at $M = 1.5$ and $3.0$ . . . . .	48
17	Aerodynamic Frequency Responses for an $\epsilon = 0.10$ Concave Ogive at $M = 1.5$ and $3.0$ . . . . .	49
18	Local Normal Force Coefficient for a $5^\circ$ Cone-Cylinder at $M = 2.0$ . . . . .	51
19	Unsteady Normal Force for $15^\circ$ Cone-Cylinder at $M = 1.35$ .	53
20	Aerodynamic Frequency Responses for Various Cone- Cylinders at $M = 2.0$ as Predicted by Quasi-Steady Potential Theory . . . . .	54

TABLE OF CONTENTS (Continued)

List of Figures (Continued)

<u>Fig. No.</u>	<u>Title</u>	<u>Page No.</u>
21	Aerodynamic Frequency Responses for a 5° Cone-Cylinder at M = 2.0 . . . . .	55
22	Aerodynamic Frequency Responses for a 10° Cone-Cylinder at M = 2.0 . . . . .	56
23	Aerodynamic Frequency Responses for a 20° Cone-Cylinder at M = 2.0 . . . . .	57
24	Effects of Mach Number on Maximum Responses of 10° and 20° Cone-Cylinders . . . . .	58
25	Aerodynamic Frequency Responses of the Local Normal Force Coefficient at Various Station Locations for a 5° Cone-Cylinder at M = 2.0 . . . . .	61
26	Aerodynamic Frequency Responses for an $\epsilon = 0.05$ Ogive-Cylinder at Various Mach Numbers as Predicted by Quasi-Steady Potential Theory . . . . .	63
27	Aerodynamic Frequency Responses for an $\epsilon = 0.05$ Ogive-Cylinder at M = 1.6 . . . . .	64
28	Aerodynamic Frequency Responses for an $\epsilon = 0.05$ Ogive-Cylinder at M = 2.6 . . . . .	65
29	Effects of Mach Number on Maximum Responses of $\epsilon = 0.05$ Ogive-Cylinder . . . . .	66
30	Frequency Response of the Slope of the Pitching Moment Coefficient for an $\epsilon = 0.05$ Ogive-Cylinder at M = 2.0 . . . . .	68
31	Slope of Pitching Moment Coefficient Versus Mach Number for $\epsilon = 0.05$ Ogive-Cylinder and $\omega = 10$ Hz. . . . .	69
32	Steady Local Normal Force Coefficient for Saturn V at M = 1.3 . . . . .	72
33	Responses of Saturn V at M = 1.3 Entering a Unit Step Gust . . . . .	73
34	Frequency Responses of Saturn V at Various Mach Numbers . . . . .	75
35	Frequency Responses of Saturn V at M = 1.3 Using Two Aerodynamic Representations . . . . .	78
36	Frequency Response of Local Normal Force on Saturn V at Several Stations at M = 1.3 for Wind Half-Amplitude of 1 M/Sec . . . . .	80
37	Frequency Response of Local Normal Force on Saturn V at Station 43.735 Meters at Various Mach Numbers for Wind Half-Amplitude of 1 M/Sec . . . . .	80



TABLE OF CONTENTS (Concluded)

List of Figures (Continued)

<u>Fig. No.</u>	<u>Title</u>	<u>Page No.</u>
38	Frequency Response of Local Normal Force on Saturn V at Station 68.575 Meters at Various Mach Numbers for Wind Half-Amplitude of 1 M/Sec . . . . .	81
39	Frequency Response of Local Normal Force on Saturn V at Station 27.000 Meters at Various Mach Numbers for Wind Half-Amplitude of 1 M/Sec . . . . .	81
40	Growth of Lift at Station 27.000 Meters of Saturn V at Different Mach Numbers . . . . .	83
41	Normalized Responses of Saturn V to a Measured Wind Profile . . . . .	86
42	Effect of Wind Shear and Aerodynamic Inertia on Local Normal Force at Station 43.735 Meters of Saturn V . .	88
43	Spring-Mass-Damper System . . . . .	89
44	Comparison of Frequency Response of Simple Spring-Mass Analogy with Actual Aerodynamic Frequency Response . .	95
45	Typical Wind Data for Eight-Point Fit . . . . .	98
46	Procedure Used to Calculate 8-Point Curve Fit Wind Shears . . . . .	102
47	Typical Wind Data for Three-Point Fit . . . . .	103
48	Procedure Used to Calculate 3-Point Curve Fit Wind Shears . . . . .	106
49	Comparison of Integrated 3-Point Curve Fit Wind Shears with Actual Wind Data . . . . .	107

## NOMENCLATURE

This list contains all symbols except those infrequently used and clearly defined in the text.

A, B, C, D, E	= regions defined by Figure 1
a	= speed of sound in the undisturbed fluid (m/sec)
$C_{N_\alpha}, C_{M_\alpha}$	= slope of normal force and moment coefficients ( $\text{rad}^{-1}$ )
$C_p$	= pressure coefficient
D	= reference diameter
f	= frequency (Hz)
$f(\xi)$	= an arbitrary function, determined so as to satisfy a boundary condition
$H(t)$	= unit step function, = 1 if $t \geq 0$ and zero otherwise
L	= characteristic body length (m)
M	= Mach number, $U/a$
$R(x)$	= equation of the body surface
r	= radial coordinate
S	= Shrouhal number ( $= fL/U$ )
$S_b$	= base area of body ( $\text{m}^2$ )
t	= time (sec.)
U	= upstream velocity (m/sec)
V	= strength of an elementary point source
$v_o$	= velocity of the side gust
$\bar{v}$	= half-amplitude of wind velocity (m/sec) (see (53))



- $x$  = axial coordinate, measured from nose of body  
 $x_g$  = pitch axis location (nondimensionalized with respect to body length)  
 $\beta$  =  $(M^2 - 1)^{\frac{1}{2}}$   
 $\epsilon$  = fineness ratio (ratio of base radius to body length)  
 $\theta$  = angular coordinate  
 $\xi$  = axial coordinate, or location of a point on the x-axis  
 $\tau$  = time (sec.)  
 $\phi, \phi, \Psi, \psi$  = velocity potentials, whose negative gradient yields a corresponding velocity vector  
 $\omega$  = angular frequency (rad/sec)

#### Subscripts

- $a$  = axial flow  
 $c$  = cross flow  
 $r, x, t, \tau, \theta$  = derivative with respect to  $r, x, t, \tau$ , or  $\theta$

## ABSTRACT

This two-volume report contains the results of a study of unsteady aerodynamics of axially symmetric vehicles. The work is based on an indicial potential theory which yields the aerodynamic forces resulting from a unit step side wind gust. The theory is linear and is applicable in the low supersonic speed range to body geometries which possess axial symmetry. The indicial results, in turn, are used with a Duhamel or convolution integral approach to obtain frequency response data and aerodynamic responses to measured wind profiles.

It was found that resonances may occur, the major factor being the vehicle shape. In particular for profiles containing conic and cylindrical portions the local normal forces on the cylindrical areas are likely to have a resonant frequency; whereas, the local normal forces on the conic portions do not.

The total normal force and pitching moment for the Saturn V exhibit a resonance to winds with a spatial wavelength of about 80 meters, as well as several other resonances at shorter wavelengths which roughly correspond to the interstage lengths. All of these resonances are of approximately the same magnitude as the zero-frequency response. Additionally, the vehicle's geometry is such that wind wavelengths of 100-200 meters are effectively filtered out by the aerodynamics. These filtered wavelengths correspond to frequencies of 2-4 Hz. in the low supersonic Mach number range.



## I. INTRODUCTION

### A. Overview

Aerospace launch vehicles of the Saturn V class are potentially vulnerable to side wind loads in ways which have not been of concern previously. Vehicles of this class are, first of all, rather flexible and massive, meaning that the bending modes of the configuration are of relatively low frequency (on the order of 1 to 10 Hertz). Secondly, the geometric configuration, consisting of several stages of different diameters joined by conic frustrums, leads to large, localized aerodynamic side forces rather than relatively uniformly distributed forces. Thirdly, the length of the vehicles (in excess of 100 meters) is such that the vertical profile of the horizontal winds must be considered (i.e., vertical wind shears are of concern). A fourth point is that the "skin" of such vehicles is relatively thin so that the possibility of damage due to large, localized unsteady forces caused by oscillatory or transient winds must be considered.

In view of the above remarks, a research program was carried out with the following objectives:

1. To extend a previously developed aerodynamic theory, an indicial theory, so that it may be applied to both sinusoidal wind profiles as well as arbitrary, numerically defined wind profiles;
2. To obtain pitching moment and normal force frequency response data for simple aerodynamic bodies, such as cones, ogives, and cone-cylinders; and
3. To obtain aerodynamic forces and moments for the Saturn V vehicle in response to sinusoidal and measured, in-flight wind profiles.

The most critical flight regime is the low supersonic portion of the flight, during which the peak dynamic pressure (maximum  $Q$ ) occurs and during which the side wind velocities are generally at their peak. The theory developed in this report applies to this flight regime.

The principal difficulty which arises when one attempts to study the aerodynamic forces of the types just mentioned is that most aerodynamic theories are not applicable. The reasons are twofold: (1) the vehicle is not slender in the sense required of "slender body" theories (e.g., the overall diameter-to-length ratio is 0.1, local surface slopes may be on the order of 0.5); and (2) the vehicle profile is not smooth, but contains slope discontinuities or sharp corners. Therefore, it was necessary to develop

a new basic theory; this was done in earlier studies by MRI. Before discussing this theory, it is instructive to briefly mention earlier steady and unsteady flow theories.

Theodor von Karman and Norton B. Moore<sup>1/</sup> developed a method for obtaining the steady axial potential flow over a pointed body of revolution traveling at supersonic speed. The method was based on the superposition of basic solutions which represent the flow over a cone. This method, which has become widely known as the Karman-Moore theory, was extended to the steady cross flow problem by Tsien.<sup>2/</sup>

This work was extended, as a numerical technique, by Van Dyke.<sup>3/</sup> He considered the Karman-Moore and Tsien solutions as being of first order compared to the exact solution of the full nonlinear potential equation. He then proceeded to show that a second order theory produces a marked improvement for the axial flow case, but that a second order cross flow theory is not obtainable in general. Van Dyke also presented other, more useful basic solutions for the first order problem.

Many authors have made slender body approximations and obtained solutions of higher order along these lines. However, such approaches for the case of bodies with slope discontinuities were questioned by Lighthill<sup>4/</sup> who then presented a modification using Stieltje's integrals, to properly account for these corners. Adams and Sears<sup>5/</sup> have developed a quite general scheme for dealing with so-called not-so-slender bodies. Several authors, and most recently Platzler and Hoffman,<sup>6/</sup> have extended their work, particularly in the solution for oscillating bodies.

Previous work in the field of unsteady or transient aerodynamic loading of axisymmetric bodies involves many assumptions and simplifications. First, it is assumed that the flow field can be described by a potential function. The resulting potential equation is then simplified by neglecting all nonlinear terms, implying that disturbances are small. Furthermore, certain terms in the linearized equation are normally dropped by assuming the body to be slender and/or the reduced frequency to be very large or very small. Also, an approximate boundary condition is normally used, again implying that the body is slender.

In the field of nonsteady problems, the case of oscillatory motions offers the greatest abundance of work. Platzler<sup>7/</sup> presents a generalization of the Karman-Moore technique which is applied to slowly oscillating bodies. Not so much work has been done, however, with the indicial case. Miles<sup>8/</sup> considers the transient motion of a body of revolution, assuming the body to be very slender and using a high-frequency approximation. This idea was applied to cone-cylinder bodies by Yates<sup>9/</sup> and Blackburn and St. John.<sup>10/</sup>

These latter studies all were concerned with both unit step and unit impulse responses. Also, Strang<sup>11/</sup> investigated some basic transient solutions of the linearized potential equation.

At Midwest Research Institute, under NASA support, Glauz et al. developed a more accurate theory for predicting aerodynamic forces on bodies of revolution traveling at supersonic speed and encountering a step side gust.<sup>12, 13/</sup> The theory satisfies the full linearized potential equation as well as the exact boundary condition when steady-state flow has been achieved. This boundary condition is satisfied in an approximate sense in the transient region of flow. The theory may be considered to be an extension of the steady-state theory previously developed by Van Dyke.<sup>3/</sup> A computer program was written by Glauz and Coombs<sup>14/</sup> to apply this technique to axisymmetric shapes of arbitrary profile, including those with slope discontinuities. Results obtained indicate excellent agreement with exact, nonlinear theory for steady flow. Steady and nonsteady data further indicate that the conventional slender body theory underestimates observed forces and may be misleading. For the transient force coefficients a simpler, quasi-steady potential theory was derived from the unsteady potential theory. Results showed that the simpler theory may prove adequate for engineering calculations.

This unsteady potential theory, termed an indicial theory, is linear. It represents the response to a unit step wind. Just as any arbitrary wind profile can be generated by superposition or integration of a large number of such step winds, the linear property of the indicial theory allows the response to likewise be generated by integration. This approach, the Duhamel or convolution integral approach, is applied in the present study.

## B. Report Organization

This final report is organized into two volumes. This volume (Volume I) contains the methodology and results obtained using the programs. The second volume<sup>15/</sup> contains the detailed descriptions and instructions for use of the various computer programs developed and used during this project.

The next section, Section II, of this volume presents the conclusions and recommendations developed from the study. Section III contains a review of the indicial aerodynamic theory and its application through use of the Duhamel integral technique. Section IV presents and discusses results of a study of several simple geometries subjected to sinusoidal winds. The geometries include cones, ogives, cone-cylinders, and ogive-cylinders. The frequency responses of local normal forces, total normal forces, and pitching moments are considered.

Finally, application of the preceding to the Saturn V launch vehicle is reported in Sections V and VI. Section V considers the frequency response characteristics, while Section VI gives the aerodynamic responses when the vehicle is exposed to measured wind profiles.

Appendices contain additional information utilized in the obtaining and analyzing of results. Appendix I presents a discussion of how simple mass-spring-damper concepts can aid in estimating the sinusoidal responses from the indicial aerodynamic loading. Appendix II presents the details of our technique of adapting NASA's wind data (obtained with the FPS-16 Radar/Jimsphere<sup>16/</sup>) to our study.

## II. CONCLUSIONS AND RECOMMENDATIONS

### A. Conclusions

It should be emphasized that the results obtained and reported here pertain to aerodynamic responses to winds, not to any subsequent vehicle responses such as rigid body pitching or elastic bending. Furthermore, these aerodynamic forces are responses to wind gusts of various types and should not be confused with various stability derivatives of a different origin. The latter are defined in terms of responses to rigid body motions, the body being immersed in a steady flow.

Before detailing the many specific findings and conclusions, two general statements concerning the responses in general are in order. One of the first questions an engineer will probably ask concerning frequency response data is, "Is a resonance condition possible; and if so, at what frequency?" It was found that, generally speaking, examination of the indicial response curve in relation to a simple, single-degree-of-freedom, spring-mass-damper system would enable this question to be answered in a qualitative way. That is, one could generally determine if a dominant resonance would occur, and often estimate the frequency of this first resonance. Other peaks may occur in the frequency response curve, but they are not easily predictable.

The second statement concerns the comparison of the results of using the full potential theory and the simpler, quasi-steady theory. No gross differences were found, although often the simpler theory slightly underestimated the response and may be even less accurate at higher frequencies. Since the indicial responses using the full theory require an order of magnitude more computer time than those using the simpler theory, it may often be advisable to perform initial studies using the quasi-steady theory.

The conclusions presented below are organized by vehicle geometry. They are, of course, limited in scope to the parameter range investigated. The pertinent range is thus indicated here also.

Cones ( $1.25 \leq M \leq 3.0$ ; semi-vertex angles up to  $33^\circ$ ;  $S \leq 2$ ): No resonance of total or local normal forces, or of pitching moment occurs. The quasi-steady theory predicts results which are nearly independent of Mach number. The full potential theory leads to frequency responses which attenuate more rapidly with frequency, but which approach the simpler, quasi-steady responses at higher speeds.



Convex and Concave Ogives ( $1.2 \leq M \leq 3.0$ ;  $\epsilon = 0.05, 0.10$ ;  $S \leq 2$ ):

No significant resonances of total normal forces or moments were observed, although a very low peak for the convex ogive did occur. This peak was at a level well below the zero-frequency response and occurred for Strouhal numbers between 1.5 and 2. The quasi-steady theory gave slight underestimates for the convex ogives and overestimates for the concave ogives, compared to the full potential theory. No large Mach number or slenderness ratio effects were observed among the total responses, beyond the obvious effects on the overall response level which may be obtained from consideration of steady flow. The local normal force for the convex ogives exhibited a resonance, the frequency of which increased with Mach number. The concave ogive local normal forces showed no resonances.

Cone Cylinders ( $1.25 \leq M \leq 3$ , cone semi-vertex angles up to  $20^\circ$ ,  $S \leq 2$ ): All responses exhibited resonance phenomena except for the local normal forces on the conic portion and on the cylindrical portion near the cone-cylinder junction. The quasi-steady theory underestimated the peak  $C_{N\alpha}$  by less than 4 percent and the peak  $C_{M\alpha}$  by, typically, less than 15 percent. The resonance occurs at lower frequency, and is of larger relative magnitude, at the large cone angles. The resonance peak exceeds the zero-frequency level by less than 11 percent for  $C_{N\alpha}$  and as much as 92 percent for  $C_{M\alpha}$ . The highest resonances occur at or near a Mach number of 2.

Ogive Cylinders ( $1.1 \leq M \leq 2.6$ ;  $\epsilon = 0.05$ ;  $S \leq 2$ ): All results were similar to the cone-cylinder results, except that at very low Mach numbers (1.1 to 1.2) the quasi-steady theory underestimated the peak response by as much as 30 percent.

Saturn V ( $1.3 \leq M \leq 1.8$ , simulated fins and shrouds,  $S < 7$ ):

The vehicle staging is such that gust wavelengths of 100 to 200 meters are effectively filtered out and not seen as part of the aerodynamic total normal force and pitching moment. In this Mach number range the corresponding frequencies are from 2 to 4 Hz. On the other hand, aerodynamic resonances do occur, roughly at wavelengths equal to the interstage distances. Specifically, peaks occurred at about 80, 50, 30, 20, and 15 meters, and an additional peak may be present at about 95 meters; but if so, it is overshadowed by the nearby peak at 80 meters. (This 80-meter peak corresponds to a frequency of 5 to 6 Hz.) All of these resonance peaks are of amplitudes on the order of or less than the zero-frequency response amplitude.

The resonant wavelengths for the total normal force and pitching moment are essentially independent of Mach number and type of aerodynamics (quasi-steady or full potential theory). However, there is evidence (inconclusive) that the more accurate theory leads to the prediction of a resonance of large amplitude of about 20 meters wavelength.

The local normal force frequency responses are strongly dependent on station location and Mach number. Resonances are not likely on the conic sections, but do occur generally on the cylindrical portions. Many of these peaks are several times the amplitude of the steady or zero-frequency response amplitude. The local frequency responses do depend strongly on Mach number, but not in a consistent fashion.

The aerodynamic response to winds shows two effects of importance. First, a time lag is evident which is accounted for by penetration effects. Secondly, a small effect arising from the aerodynamic transients (or aerodynamic inertia) is observed. This latter effect is correlated with the wind shear.

#### B. Recommendations

The integration of the indicial responses is currently performed using a step size which depends on the spacing of the indicial responses. This placed a restriction on the validity of some of the high frequency results obtained in this study. Either the computer program should be modified or finer intervals should be used in evaluating the indicial responses. Then, the high-frequency results, where important, should be checked for validity. Of particular concern is the Saturn V response, using the full potential theory, at a wavelength of about 20 meters ( $S = 6$ ).

Currently available wind data are at intervals (25 meters) which are too coarse to elicit resonance responses. Should more detailed data become available, it would be of interest to re-examine the Saturn V behavior.

It would be of great benefit to compare the current theories with wind tunnel results. Of course, the experiments must involve gust responses, and thus are different from the more routine oscillating body experiments.

The coupling of aerodynamics and the vehicle rigid body and elastic degrees of freedom has been studied previously. However, it might be of considerable interest to re-examine this coupling in light of the findings of the present study. In particular, the aerodynamic excitation of the lower bending modes may be fortuitously light since these model frequencies are under 5 Hz. But, the fifth and sixth modes, which to our knowledge have not been examined in detail, may suffer direct aerodynamic excitation.

The present computer programs have been run on the IBM 7094. They should be made operable on the newer machines (e.g., Univac 1108). This would be a minor undertaking.

### III. REVIEW OF THEORY

In this section we briefly review the development of the indicial theory and present the Duhamel integral approach utilizing the indicial results. The indicial theory has been described previously in some detail<sup>12,13,17</sup>; the presentation here will thus be brief. The extension of this axially symmetric theory to wing-body configurations,<sup>18</sup> through the "equivalent body" concept, will also be indicated.

#### A. Formulation of Indicial Theory

The indicial problem to be solved can be stated as follows: find the transient flow field, pressure, etc., on a pointed body of revolution encountering a side gust while traveling at supersonic speed. Using linearized potential theory, the problem may be separated into an axial flow and a cross-flow problem. The latter, which is of prime concern here, may be stated mathematically as follows:

Find the solution to the linearized potential equation

$$\Phi_{rr} + \frac{1}{r} \Phi_r + \frac{1}{r^2} \Phi_{\theta\theta} - \beta^2 \Phi_{xx} - 2M^2 \Phi_{x\tau} - M^2 \Phi_{\tau\tau} = 0 \quad , \quad (1)$$

with the boundary conditions

$$\frac{1}{\cos \theta} \Phi_r = -v_0 H(\tau-x) \text{ at } r = \infty \text{ , and}$$

$$\Phi_r - R^2 \Phi_x = 0 \text{ at surface of the body.}$$

The velocity vector is the negative gradient of the velocity potential,  $\Phi$ .

We will write the solution as

$$\Phi = \Psi + \phi \quad (2)$$

where

$$\Psi \equiv -v_0 r \cos \theta H(\tau-x) \quad (3)$$

Now,  $\Psi$  satisfies Eq. (1) and likewise,  $\phi$  must satisfy (1). The boundary conditions for  $\phi$  become

$$\phi_r = 0 \quad \text{at} \quad r = \infty \quad (4)$$

$$\phi_r - R'\phi_x = v_0 \cos \theta H(\tau-x)$$

$$\text{at the body, } r = R(x) \quad (5)$$

The associated problem to the cross-flow situation which has just been formulated is the axial flow problem. The steady axial flow solution is also needed to obtain the required force coefficients. For completeness, this solution, which is presented by Van Dyke<sup>3</sup> is also included here. The axial flow potential is a function which satisfies (1) and (4), but in place of (5), we require

$$-\phi_{ar} + R'\phi_{ax} = R'U \quad \text{at the body,}$$

$$r = R(x) \quad (6)$$

For clarity, the subscript  $a$  (and subsequently,  $c$ ), denoting axial and cross-flow potentials, will be used unless the context makes the distinction unnecessary.

## B. Integral Representation of Solution

To solve the transient cross-flow problem, a generalization of the method of Karman and Moore<sup>1</sup> is used. This technique involves a superposition of basic solutions of (1) and (4), done in such a manner as to satisfy relation (5) at a discrete number of points. The basic solutions used were developed in a fashion similar to the method used by Strang.<sup>11</sup> We will first look at solutions to an axial flow problem, which are essentially time-dependent sources. Cross-flow solutions can then be easily found as doublets, by means of the relation

$$\phi_c = \cos \theta \frac{\partial}{\partial r} \theta_a \quad (7)$$

Our basic solution, called a gust source, can be conceived of physically as follows. Consider a coordinate system fixed to the vehicle, with its origin at the nose of the vehicle. The x-axis lies along the vehicle axis, pointing aft. The vehicle is moving in the negative x-direction with supersonic speed, U. At time t = 0 the nose of the vehicle encounters a disturbance in the otherwise uniform upstream flow.

Now, consider an arbitrary, supersonic point source located at  $x = \xi$ . This source starts "emitting" at time  $\xi/U$ ; that is, at the time required for the disturbance to move a distance,  $\xi$ , relative to the vehicle. The various regions of influence of this source, denoted by lower case letters, are shown in Figure 1, after it has started emitting.

The smaller sphere has the equation

$$(x-Ut)^2 + r^2 = a^2(t-\xi/U)^2 \quad (8)$$

while the cone has the equation

$$x = \xi + \beta r \quad (9)$$

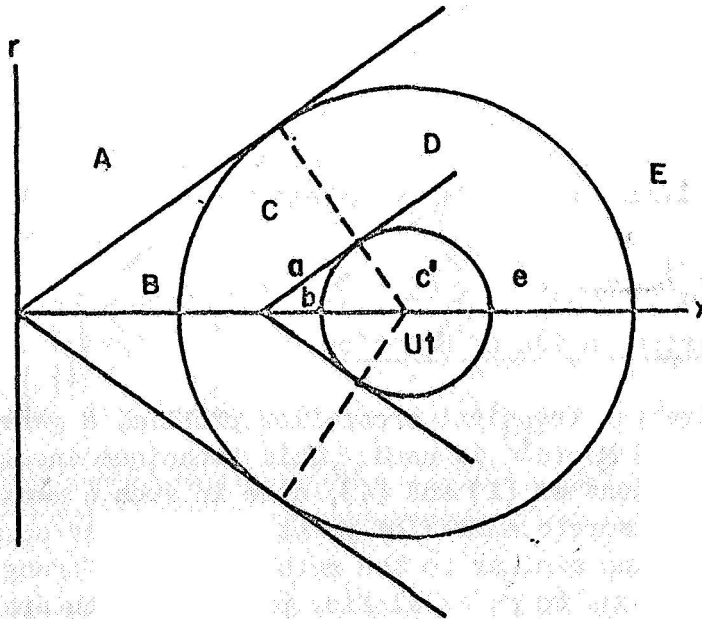


Figure 1 - Regions of Influence of Moving Point Source



The dotted lines represent the locus of intersections of the spheres and associated cones, and have the equation

$$x = Ut - r/\beta \quad (10)$$

These lines divide the large sphere into two regions, C and D.

This point source at  $x = \xi$  has the potential  $\phi_1$  given by

$$\left. \begin{aligned} \phi_{1b} &= \frac{v}{2\pi [(x-\xi)^2 - \beta^2 r^2]^{1/2}} \text{ in (b)} \\ \phi_{1c} &= \frac{v}{4\pi [(x-\xi)^2 - \beta^2 r^2]^{1/2}} \text{ in (c')} \\ \phi_1 &= 0 \text{ elsewhere} \end{aligned} \right\} \quad (11)$$

A distribution of sources along the x-axis, where each source starts emitting as it crosses a gust front is called a gust source. It is this type of distribution that is used to find a solution to the problem of interest. This gust source includes sources located on the axis between  $x = 0$  and  $x = Ut$ . To obtain the total source potential,  $\phi_a$ , we evaluate the integral

$$\phi_a(x, r, t) = \int_0^\infty \phi_1(x, r, ; \xi) f(\xi) d\xi \quad (12)$$

where  $\phi_1$  is given in (11). The function  $f(\xi)$ , which may be chosen arbitrarily, represents a possible variation of source strength with position.

At a point fixed on the vehicle, the integral (12) takes on a succession of forms as time increases. At first, the point is in Region E of Figure 1, it has not yet been affected by the disturbance, and  $\phi_1 \equiv 0$ . Later, the point becomes engulfed by the disturbance as Region D, then C move by the point as they expand. During this time  $\phi_s$  has a transient character. Finally, Region C moves by and the point is left in Region B.

At this time,  $\phi_s$  becomes a constant value (i.e., steady state). It is never in Region A since the Mach cone defining Region A does not move relative to the vehicle.

The disturbances of interest here are cross winds; hence, the only transient solutions of interest are the cross-flow solutions, obtained utilizing (12) and (7). We do need, however, the axial steady-flow solutions, so they are given subsequently with the cross-flow case.

At this point the function  $f(\xi)$ , which is the local source strength, is still arbitrary. In theory,  $f(\xi)$  is that function which leads to the satisfaction of the surface boundary condition (either (5) or (6)). If the general solution is placed into the appropriate boundary condition equation, an integral equation in  $f(\xi)$  results. The integral equation developed in this way cannot be solved analytically except for certain special body shapes. Therefore, recourse is made to approximate techniques; in our case, an extension of the method of Karman and Moore.<sup>1/</sup>

Three different forms of the function  $f(\xi)$  are used, for both the axial as well as the cross-flow solutions. These three forms are now presented.

### C. Linear (Gust Doublet) Solution

One useful form of  $f(\xi)$  to be used in Eq. (12) is the linear form where  $f(\xi)$  is proportional to  $\xi$ . The resulting potential is

$$\phi_a = A \left\{ x \cosh^{-1}(x/\beta r) - \beta r \left[ (x/\beta r)^2 - 1 \right]^{\frac{1}{2}} \right\} . \quad (13)$$

This is the exact solution for axial flow over a cone. The constant,  $A$ , is to be determined from the boundary condition (6). The associated exact solution for steady cross flow over a cone can be obtained using  $f(\xi)$  proportional to  $\xi^2$  and then differentiating according to Eq. (7). The solution is extended to the transient case also. The result is termed the gust doublet solution and is summarized below.

For Region B,

$$\phi_c = C \left\{ r \cosh^{-1}(x/\beta r) - (x/\beta) \left[ (x/\beta r)^2 - 1 \right]^{\frac{1}{2}} \right\} , \quad (14)$$

and for Regions C and D,

$$\phi_c = (C/2\beta^2) \left\{ \frac{1}{r \left[ (x-Ut)^2 + r^2 \right]^{\frac{1}{2}}} \left[ r^2(x+Ut) + x^2(x-Ut) - Mr^2 \left[ (x-Ut)^2 + r^2 \right]^{\frac{1}{2}} \right] \right. \\ \left. \pm \beta^2 r \cosh^{-1} \left[ \frac{x-Ut + M \left[ (x-Ut)^2 + r^2 \right]^{\frac{1}{2}}}{\beta r} \right] \right. \\ \left. + \beta^2 r \cosh^{-1}(x/\beta r) - \frac{x}{r} (x^2 - \beta^2 r^2)^{\frac{1}{2}} \right\} \quad (15)$$

In Eqs. (14) and (15) the constant, C, is to be determined from condition (5). (A factor,  $\cos \theta$ , has also been incorporated into C for convenience.) Where a choice of signs is given, the upper sign is to be used in Region C, the lower in Region D.

The axial flow solution given in (13) is the one used by Karman and Moore,<sup>1/</sup> while the steady portion of the cross-flow solution, as given in (14), is the one used by Tsien.<sup>2/</sup> It is thus the exact cross-flow solution for a cone. In principle, these solutions, together with the unsteady portion given in (20), are sufficient for use in a Karman-Moore type superposition for solving for the flow over axially symmetric bodies of arbitrary shape. It is more convenient and economical, however, to make use of the more sophisticated solutions presented next.

#### D. Quadratic Solution

The linear-type solution just given is the exact solution for a cone, and provides an excellent start for obtaining the flow over arbitrary, pointed bodies. However, the derivatives of the velocity components are discontinuous along the Mach line  $x = \beta r$ . When this type of solution is used in a Karman-Moore scheme, therefore, a "smooth" result is not obtained. To obtain reasonable accuracy, many such solutions must be used to make the irregularities small.

To avoid this problem, a smoother basic solution may be used. This idea was first used by Van Dyke<sup>3/</sup> where he sought the second-order steady flow based on using solutions of (1) as the first-order approximations. A convenient steady axial flow solution is obtained by using a quadratic function for  $f(\xi)$  in Eq. (12). The result so obtained is

$$\phi_a = Ax^2 \left\{ \left[ 1 + 0.5(\beta r/x)^2 \right] \cosh^{-1}(x/\beta r) - 1.5 \left[ 1 - (\beta r/x)^2 \right]^{\frac{1}{2}} \right\}, \quad (16)$$

where A is a constant.

The corresponding cross flow is obtained by using  $f(\xi)$  proportional to  $\xi^3$  in (12) and applying (7). For Region B the result is

$$\phi_c = C \left\{ 3xr \cosh^{-1}(x/\beta r) - (x^2 + 2\beta^2 r^2) \left[ x^2 - \beta^2 r^2 \right]^{\frac{1}{2}} / r\beta^2 \right\}. \quad (17)$$

For Regions C and D

$$\begin{aligned} \phi_c = (C/2) \left\{ 3xr \cosh^{-1}(x/\beta r) - (x^2 + 2\beta^2 r^2) \left[ x^2 - \beta^2 r^2 \right]^{\frac{1}{2}} / r\beta^2 \right. \\ \left. + 3xr \cosh^{-1}[(x-\Lambda)/\beta r] + [2M^2(x-Ut) - 3x] Mr/\beta^2 \right. \\ \left. + (1/r\beta^2) \left[ x^3(x-Ut) + 3xUtr^2 + r^2(x-Ut)^2 \right] / \left[ (x-Ut)^2 + r^2 \right]^{\frac{1}{2}} \right. \\ \left. + (r/\beta^2)(1+3\beta^2) \left[ (x-Ut)^2 + r^2 \right]^{\frac{1}{2}} \right\}, \quad (18) \end{aligned}$$

where

$$\Lambda = Ut - M \left[ (x-Ut)^2 + r^2 \right]^{\frac{1}{2}}. \quad (19)$$

### E. "Corner" Solution

The two basic solutions presented thus far are continuous and serve well for determining the flow over smooth, pointed bodies of revolution. However, current space vehicle designs are not smooth bodies but have several slope discontinuities (or corners). These corners occur between stages and cause aerodynamic discontinuities. Rather than approximate a discontinuity with several continuous solutions, it is more reasonable to use a third basic solution which inherently contains such a behavior.

Van Dyke<sup>3/</sup> first presented such a solution for the case of steady flow. We give his results here together with the extension to unsteady cross flow. For axial flow,  $f(\xi)$  is chosen proportional to  $\xi^{\frac{3}{2}}$ , yielding

$$\phi_a = 2A(x+\beta r)^{\frac{1}{2}} [K(k) - E(k)] \quad (20)$$

where A is a constant. K(k) and E(k) are the complete elliptic integrals of the first and second kind with

$$k^2 = \frac{x-\beta r}{x+\beta r} \quad (21)$$

For the cross-flow problem  $f(\xi)$  is taken proportional to  $\xi^{3/2}$  in (12). After application of (7), the result for Region B is

$$\phi_c = -C(x/\beta r)(x+\beta r)^{\frac{1}{2}} \{E(k) - (\beta r/x)K(k)\} \quad (22)$$

In Region C,

$$\begin{aligned} \phi_c = -C \left\{ (x/\beta r)(x+\beta r)^{\frac{1}{2}} [E(k) - (\beta r/x)K(k)] \right. \\ \left. - \frac{1}{2}(x/\beta r)(x+\beta r)^{\frac{1}{2}} [E(\alpha, k) - (\beta r/x)F(\alpha, k)] \right. \\ \left. - (\frac{1}{2}\beta r)\Lambda^{\frac{1}{2}} [x(x-Ut)+r^2] / [(x-Ut)^2+r^2]^{\frac{1}{2}} \right\} \quad (23) \end{aligned}$$

And, in Region D,

$$\begin{aligned} \phi_c = -C \left\{ \frac{1}{2}(x/\beta r)(x+\beta r)^{\frac{1}{2}} [E(\alpha, k) - (\beta r/x)F(\alpha, k)] \right. \\ \left. - (\frac{1}{2}\beta r)\Lambda^{\frac{1}{2}} [x(x-Ut)+r^2] / [(x-Ut)^2+r^2]^{\frac{1}{2}} \right\} \quad (24) \end{aligned}$$

In the above  $F(\alpha, k)$  and  $E(\alpha, k)$  are the incomplete elliptic integrals of the first and second kind with

$$\alpha = \sin^{-1} \left\{ \Lambda^{\frac{1}{2}} / [x-\beta r]^{\frac{1}{2}} \right\} \quad (25)$$



F. Satisfaction of Boundary Conditions

The three basic types of solutions are now to be superimposed in such a way as to satisfy the appropriate boundary conditions.

The above elementary gust solutions have their space and time origins both at zero. A more general solution is obtained by locating the space origin at  $x = \xi_k$  and the time origin at

$$t = t_k \equiv \xi_k/U \quad (26)$$

This is precisely the time required for a vehicle (or part thereof) of length  $\xi_k$ , and traveling at speed  $U$ , to penetrate a gust front. The corresponding solution is simply obtained from the previous expressions by replacing  $x$  by  $x - \xi_k$  and  $t$  by  $t - t_k$ . Let us write such a solution for axial flow as

$$\phi_{a_k} = A_k \psi_{a_k} \quad (27)$$

The complete solution may then be written

$$\phi_a = \sum_{k=1}^N A_k \psi_{a_k} \quad , \quad (28)$$

$$\phi_c = \sum_{k=1}^N C_k \psi_{c_k} \quad . \quad (29)$$

The  $C_k$  and  $A_k$  are to be determined by applying the boundary conditions at  $N$  points on the surface of the body.

To aid in determining the constants, consider Figure 2. A sequence of values of  $\xi_k$  is shown on a representative vehicle. Through each point,  $\xi_k$ , is drawn a Mach line,

$$x - \xi_k = \beta r \quad . \quad (30)$$

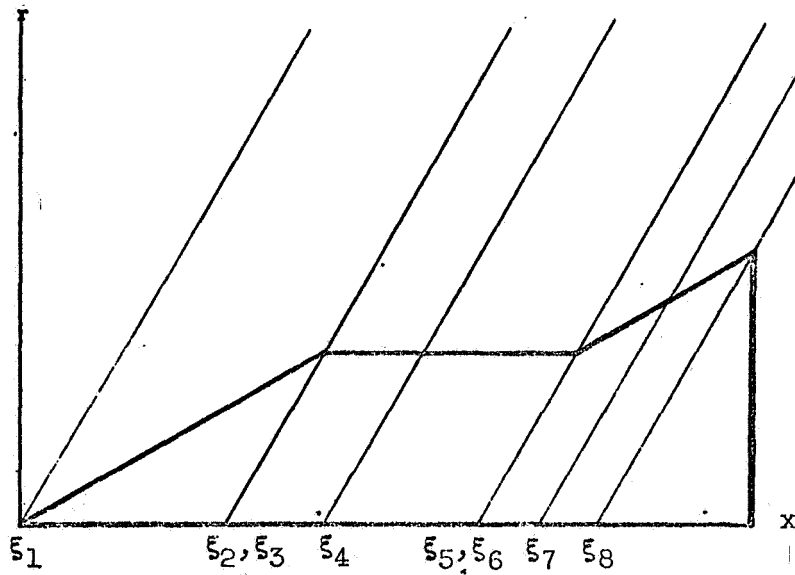


Figure 2 - Representative Vehicle Showing Control Points

Consider the intersection of the  $(n+1)$ th Mach line with the body profile. Call this point  $P_{n+1}$  with coordinates  $(x_{n+1}, r_{n+1})$ . By evaluating the appropriate boundary condition at this point, the unknown coefficients,  $A_n$  and  $C_n$  may be determined. For, upon substituting (28) into (6) and rearranging,

$$A_n = - \frac{\sum_{k=1}^{n-1} A_k \psi_{ar_k} + R' \left[ U - \sum_{k=1}^{n-1} A_k \psi_{ax_k} \right]}{\psi_{ar_n} - R' \psi_{ax_n}}, \quad (31)$$

and in a similar fashion, using (29) in (5),

$$C_n = - \frac{-v_0 \cos \theta + \sum_{k=1}^{n-1} C_k \psi_{cr_k} - R' \sum_{k=1}^{n-1} C_k \psi_{cx_k}}{\psi_{cr_n} - R' \psi_{cx_n}}. \quad (32)$$

The second subscript (r or x) indicates partial differentiation with respect to r or x. The functions  $\psi_{ar_k}$ , etc., and R' (the slope of the vehicle surface) are all to be evaluated at the point  $P_{n+1}$ , or, more precisely, an infinitesimal distance upstream of  $P_{n+1}$ , and under steady-state conditions. All basic solutions for which  $k \geq n+1$  have the value zero so they do not appear in the above equations. Assuming the coefficients for  $k < n$  are all known, the (n)th set can be computed directly. Thus, by starting at  $P_2$ , and progressing downstream, all coefficients may be obtained.

The choice of types and locations of solutions to be used for a given body geometry is best made in the following manner. Starting at  $\xi_1$  is a linear-type solution. Following this is a sequence of quadratic-type solutions, with a corner-type solution added for each slope discontinuity. Referring again to Figure 2,  $\xi_2$  is the origin of a corner solution,  $\xi_3$  and  $\xi_4$  are the quadratic types,  $\xi_5$  a corner type, etc. In practice,  $\xi_2$  and  $\xi_3$  are considered to be separated by an infinitesimal distance so that Eqs. (31) and (32) may be applied uniformly, regardless of the solution type. Van Dyke<sup>19</sup> suggests, as a rule of thumb for spacing between the other  $\xi$ 's, a value

$$\Delta\xi = \beta R, \text{ approximately} \quad , \quad (33)$$

except for immediately downstream of a corner, where one-half this spacing is advisable.

### G. Aerodynamic Forces

The unsteady pressure coefficient may be written as

$$C_P = \frac{1}{U^2} \left\{ 2U\phi_x - \phi_r^2 - \frac{1}{r^2} \left( \phi_\theta^2 + \beta^2 \phi_x^2 + 2\phi_t \right) \right\} \quad , \quad (34)$$

where terms of order higher than 2 in the derivatives of  $\phi$  have been neglected. Now, the potential function,  $\phi$ , is the complete perturbation potential and may be written as

$$\phi = \phi_a + \phi_c \cos \theta + \psi \cos \theta \quad , \quad (35)$$

where all  $\theta$ -dependence is shown explicitly.

The end result which is desired here is not the pressure coefficient itself, but rather generalized force coefficients, such as

$$C_{F_l} = \frac{1}{S_b L^l} \int_0^{2\pi} \int_0^L C_P x^l \cos \theta \, dx d\theta, \quad (36)$$

where

$$C_{F_0} \equiv C_N,$$

the normal force coefficient, and

$$C_{F_1} \equiv C_M,$$

the pitching moment coefficient about the apex.

Due to the integration on  $\theta$ , the only portions of  $C_P$  which have a nonzero contribution to (36) are those terms involving  $\cos \theta$ . Defining that part, then, as  $C_P^*$ , yields

$$C_P^* = \frac{2 \cos \theta}{U^2} \left\{ U \phi_{cx} + \phi_{ct} - \phi_{ar} (\phi_{cr} + \psi_r) + \beta^2 \phi_{ax} \phi_{cx} \right\}. \quad (37)$$

Inserting (37) into (36) gives

$$C_{F_l} = \frac{2\pi}{U^2 S_b L^l} \left\{ \int (\phi_{ct} + U \phi_{cx}) x^l R(x) dx - \int \phi_{ar} \phi_{cr} x^l R(x) dx \right. \\ \left. + v_0 \int \phi_{ar} x^l R(x) H(Ut-x) dx + \beta^2 \int \phi_{ax} \phi_{cx} x^l R(x) dx \right\}. \quad (38)$$

The first line of (38) contains the contribution of the linearized pressure coefficient. The rest is the result of retaining quadratic terms. The third line is often considered small compared to the second line and, hence, neglected. Such is not always the case, however, and it is retained in the present work.

The local normal force,  $dC_N/dx$ , is obtained by differentiating  $C_{F_0}$  or, in practice, by evaluating the integrand of (38).

The theory which involves the use of Eqs. (14)-(25) in Eq. (38) is termed the full indicial potential theory. A simplified version is also utilized which uses only the steady-state (Region B) equations from the set (14)-(25). This "quasi-steady" theory implies that the flow over the portion of the vehicle immersed in the gust is at steady-state conditions, whereas the remainder of the vehicle is not yet affected by the gust. Thus, the theory accounts for gust penetration but not for the aerodynamic inertia.

## H. Equivalent Body Concept

The indicial solution presented above holds only for bodies possessing complete axial symmetry. A method for inclusion of the effect of nonaxially symmetric protuberances is necessary to handle certain geometries. For example, the fins and shrouds of the Saturn V generate over half the total lift of the vehicle, and cannot be ignored. Thus, the technique of an equivalent body was evolved.<sup>18/</sup>

This concept, simply stated, is to replace the finned vehicle with an artificial body of revolution. The latter is designed so as to have the same steady-state normal force distributions as the original winged vehicle. The hypothesis, then, is that the lift growth of the equivalent body of revolution approximates the lift growth of the body with wings to engineering accuracy.

The application of this concept involves rewriting the expressions given earlier. From Eq. (38), using (28) and (29), the steady local normal force, at the point  $(x_{n+1}, R_{n+1})$ , may be written in the form

$$\left. \frac{dC_{N\alpha}}{d(x/D)} \right|_{n+1} = F(R_0) \left\{ v_0 \sum_{k=1}^n A_k \psi_{ak_r} - \sum_{k=1}^n A_k \psi_{ak_r} \sum_{k=1}^n C_k \psi_{ck_r} + \beta^2 \sum_{k=1}^n C_k \psi_{ck_x} \sum_{k=1}^n A_k \psi_{ak_x} + \sum_{k=1}^n C_k \psi_{ck_x} \right\}, \quad (39)$$

where  $F(R_0)$  is a function of the reference area. Now, if one considers  $R$  and  $R'$  as being unknown at the axial position,  $x_{n+1}$ , then  $A_n$  and  $C_n$  are also unknown. However, they may be eliminated by means of Eqs. (31) and (32).

Using the notation

$$S_{an_x} = \sum_{k=1}^{n-1} A_k \psi_{ak_x}, \text{ etc.}, \quad (40)$$

Eq. (39) reduces to

$$a_n R_{n+1}^2 + b_n R_{n+1}' + c_n = 0, \quad (41)$$

where

$$a_n(x, R_{n+1}) = \frac{dC_{N\alpha}}{d(x/D)} (\psi_{an_x} \psi_{cn_x}) - F(R_0) \left\{ S_{cn_x} \psi_{cn_r} + (v_0 - S_{cn_r}) \psi_{cn_x} \right\} \left\{ S_{an_r} \psi_{an_x} + (U - S_{an_x}) \psi_{an_r} \right\}, \quad (42)$$

$$b_n(x, R_{n+1}) = - \frac{dC_{N\alpha}}{d(x/D)} (\psi_{an_r} \psi_{cn_x} + \psi_{an_x} \psi_{cn_r}) + F(R_0) \left\{ S_{cn_x} \psi_{cn_r} + (v_0 - S_{cn_x}) \right\} (1 + \beta^2 U) \psi_{an_x}, \quad (43)$$

$$c_n(x, R_{n+1}) = \frac{dC_{N\alpha}}{d(x/D)} (\psi_{an_r} \psi_{cn_r}) - F(R_0) \left\{ S_{cn_x} \psi_{cn_r} + (v_0 - S_{cn_r}) \psi_{cn_x} \right\} \left\{ (1 + \beta^2 S_{an_x}) \psi_{an_r} - \beta^2 S_{an_r} \psi_{an_x} \right\}, \quad (44)$$



and the  $Y$ 's are explicit (albeit complicated) functions of  $R_{n+1}$ . Thus, Eq. (41) represents a relation between the unknowns  $R_{n+1}$  and  $R'_{n+1}$  and the knowns  $dC_{N_Q}/d(x/D)$  and the  $A_k$  and  $C_k$  for  $k \leq n$ . A second equation may be written using the definition of a derivative. Assuming  $x_n$  and  $x_{n+1}$  to be close together, we have

$$R_{n+1} \simeq R_n + (x_{n+1} - x_n) \frac{R'_n + R'_{n+1}}{2}, \quad (45)$$

or

$$R'_{n+1} = -R'_{n+2} \frac{R_{n+1} - R_n}{x_{n+1} - x_n}. \quad (46)$$

Equations (41) and (46) are then to be solved simultaneously for  $R_{n+1}$  and  $R'_{n+1}$ . The solution is carried out by varying  $R_{n+1}$  until the difference,  $E_{n+1}$ , between the solutions of (46) and (41) is zero (or sufficiently small). Care is needed with (41) to insure that the two roots are not inadvertently interchanged.

This procedure worked well in previous studies,<sup>18/</sup> but is limited to configurations where the local forces are not too large. The limitation is that  $R'_{n+1}$  must not exceed the slope of the Mach cone,  $1/\beta$ . Initial attempts at application of the method to the Saturn V lead to difficulties.

Published data<sup>20/</sup> indicated that the lift generated by the Saturn V shrouds could be approximated by a triangular lift distribution, varying linearly from zero at the leading edge of the shroud to a maximum at the rear of the shroud. We envisioned approximating the lift of the fins in the same fashion, and superimposing the two lift distributions. First, it was found that the lift over the forward portion of the shrouds (ahead of the fin location) could be used and an equivalent body geometry generated. (It was, however, approaching the Mach cone limit and the numerics showed signs of instability.) Secondly, in stepping the solution toward larger  $x$ -values, the limit of acceptable  $R'$  values was exceeded when the fins were encountered. Thus, there was too much lift to be handled in this way, to this degree of approximation.

The following alternative approach was followed in the present study. The entire fin-shroud region was replaced by a single conic section. This conic section was selected (by trial and error) so as to generate the same total lift as the published data<sup>20/</sup> required (Figure 3). The section

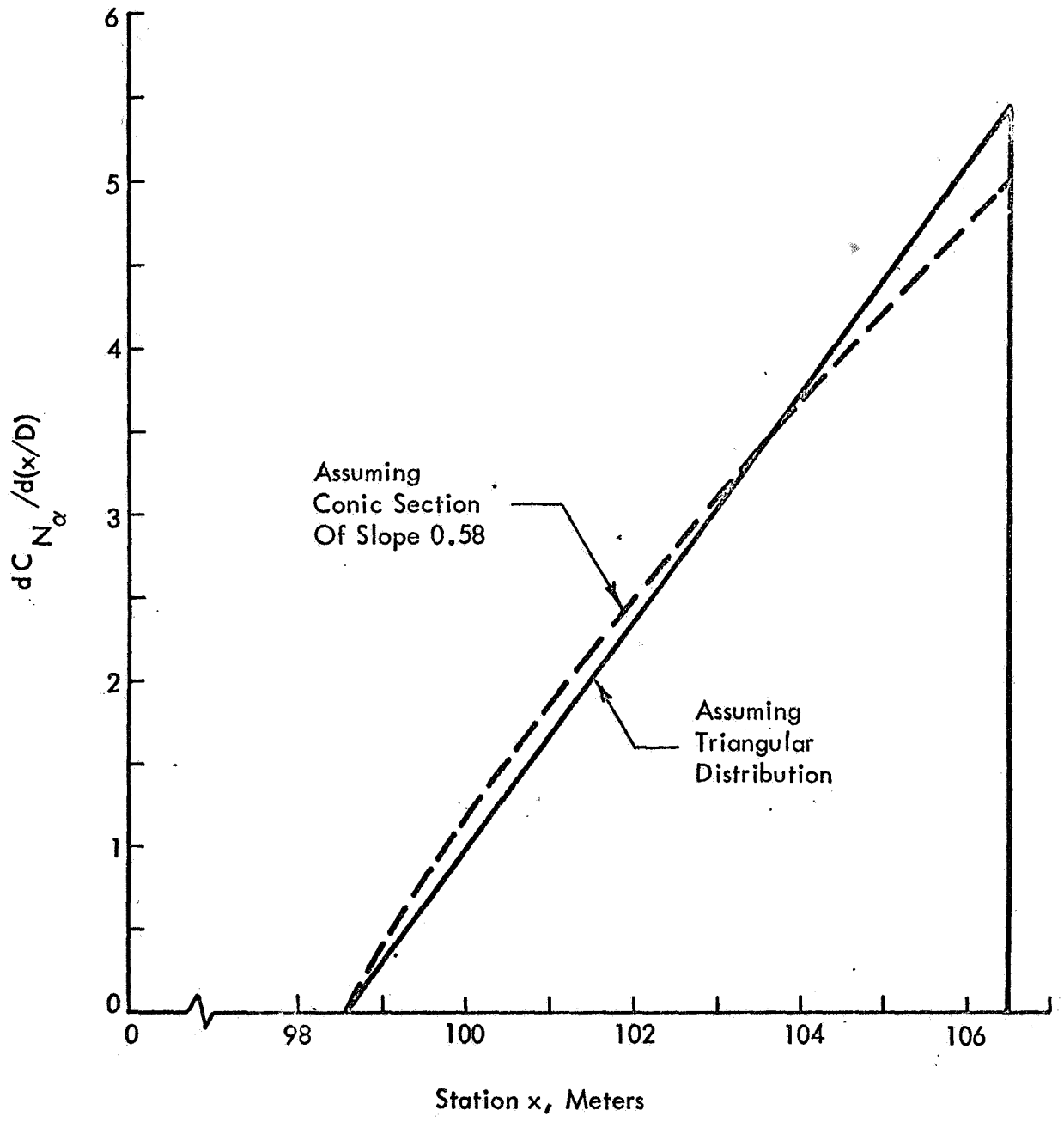


Figure 3 - Lift Distribution in Fin-Shroud Region at Mach Number 1.6

started at the forward edge of the shroud; the cone angles used are given in Table I. An indication of the lift distribution so calculated is given in Figure 3. It would be desirable to have experimental data to compare this with, but data do not appear to exist which give the detailed lift distribution in this region. In any case, we believe that any differences which may exist between the lift distribution used here and the true distribution would have negligible effect on the vehicle frequency responses in the Strouhal number range investigated (up to  $S = 7$ ), since the fin-shroud region occupies less than  $1/13$  of the total vehicle length.

TABLE I

CONE ANGLES EQUIVALENT TO FIN-SHROUD REGION

<u>Mach No.</u>	<u>R'</u>	<u><math>\theta</math></u>
1.3	0.71	35.4
1.4	0.65	33.0
1.5	0.61	31.4
1.6	0.58	30.1
1.7	0.56	29.2
1.8	0.54	28.4

I. Duhamel Integral

The indicial force coefficients (38) are linear functions of  $v_0$ , the magnitude of the wind gust. Therefore, the Duhamel integral may be used to obtain force coefficients resulting from arbitrary winds.

Given an indicial response function  $f(x, \tau)$ , the response  $F(x, t)$  to any arbitrary forcing function is computed as a convolution integral,

$$F(x, t) = v(0)f(x, t) + \int_0^t v'(\bar{\tau})f(x, t-\bar{\tau})d\bar{\tau} \quad , \quad (47)$$

where  $v(\bar{\tau})$  is an arbitrary forcing function (wind profile) and the prime denotes the time derivative.\*

\* Equation (47) involves the response to the unit step,  $f(x, t)$ , and the derivative of the wind profile. An alternate formulation could be written which involves the response to a unit impulse (the time derivative of  $f$ ) and the wind profile. It was deemed easier in this study to differentiate the wind profile rather than the indicial response.

By replacing  $t-\bar{\tau}$  with  $\tau$ , the integral may be rewritten

$$F(x,t) = v(0)f(x,t) + \int_0^t f(x,\tau) \frac{dv(t-\tau)}{dt} d\tau \quad (48)$$

Now, dropping the x-dependence, nondimensionalizing the wind velocity with  $U$ , and introducing  $C(t)$  as a general force coefficient (e.g.,  $C_{N\alpha}(t)$ ,  $C_{M\alpha}(t)$ , etc.), we have

$$c(t) = \frac{v(0)}{U} C_s(t) + \frac{1}{U} \int_0^t C_s(\tau) \frac{dv(t-\tau)}{dt} d\tau \quad (49)$$

where  $C_s(\tau)$  is the indicial force coefficient which corresponds to the wind-induced force coefficient,  $C(t)$ .

Since our functions,  $C_s(\tau)$ , all reach a steady-state value (say,  $\bar{C}_s$ ) in a finite time, it is convenient to deal with the difference between the transient indicial response and its steady-state value. That is, we introduce

$$g(t) = \bar{C}_s - C_s(t) \quad (50)$$

and obtain

$$c(t) = \frac{v(t)}{U} \bar{C}_s - \frac{v(0)}{U} g(t) - \frac{1}{U} \int_0^t g(\tau) \frac{dv(t-\tau)}{dt} d\tau \quad (51)$$

It is implicitly assumed above that the response is desired to a wind which has a velocity of zero for  $\tau < 0$ , and of  $v(\tau)$  for  $\tau \geq 0$ . The response thus includes, in general, a transient portion caused by the "jump" in wind velocity at  $\tau = 0$ . But, this is usually not of physical interest. It is furthermore clear that if the indicial response  $C_s$  reaches steady state in time  $t_s$ , the vehicle wind response at time  $t$  is influenced only by the winds from  $t-t_s$  to  $t$ . Thus (provided  $t > t_s$ ), there should be no transient portion of  $C(t)$  caused by the jump at  $\tau = 0$ . This can be easily shown, mathematically, by simply noting from (50) that, for  $t \geq t_s$ ,  $g(t) \equiv 0$ . We thus have

$$C(t \geq t_s) = \frac{v(t)}{U} \bar{C}_s - \frac{1}{U} \int_0^{t_s} G(\tau) \frac{dv(t-\tau)}{dt} d\tau \quad (52)$$

This form of the integral is the one of most use in the present study. It involves only a finite integral, backward in time, over the range  $0 \leq \tau \leq t_s$ , regardless of the range of  $t$ , provided, of course,  $t \geq t_s$ . The latter assumption simply means, physically, that we require the wind  $v(t)$  to be defined for a period of at least  $t_s$  prior time  $t$ .

A wind profile of particular interest is the sinusoidal wind

$$v(t) = \bar{v} \cos \omega t \quad (53)$$

Substituting (53) into (52) yields the special case

$$C(t) = C_i \cos \omega t + C_o \sin \omega t \quad , \quad (54)$$

where  $C_i$  and  $C_o$  are constants given by

$$C_i = \frac{\bar{v}}{U} \left[ \bar{C}_s - \omega \int_0^{t_s} G(\tau) \sin \omega \tau d\tau \right] \quad , \quad (55)$$

$$C_o = \frac{\bar{v}}{U} \left[ \omega \int_0^{t_s} G(\tau) \cos \omega \tau d\tau \right] \quad . \quad (56)$$

These are the in- and out-of-phase components of the response, respectively. The magnitude of the response is given by

$$|C|^2 = C_i^2 + C_o^2 \quad , \quad (57)$$

whereas the phase angle between the response and the wind is given by

$$\theta = \tan^{-1} (C_o/C_i) \quad . \quad (58)$$

In conclusion, Eq. (52) gives the form of the convolution integral used for arbitrary wind profiles,  $v(t)$ , whereas Eqs. (54)-(56) are used for the special case of sinusoidal winds. In either case, the indicial response (actually the difference between the transient and steady-state values) is integrated, after being multiplied by the time derivative of the wind profile. The method of differentiating the wind profile is given in Appendix II.

## J. Stability Derivatives

The derivatives of the total normal force and pitching moment coefficients,  $C_{N\alpha}$  and  $C_{M\alpha}$ , are interpreted as responses to a sinusoidal wind in this study. These quantities are computed by the computer programs, where the wind is written as

$$v(t) = \bar{v} \cos \omega t \quad . \quad (53)$$

Since the vehicle velocity is  $U$ , the cross flow at any station,  $x$ , could be written

$$v(x) = \bar{v} \cos(\omega x/U) \quad (59)$$

Thus, the cross flow varies, at any instant of time, with vehicle station location. The angle of attack,  $\alpha$ , used in defining  $C_{N\alpha}$  and  $C_{M\alpha}$  is determined from the magnitude of the cross-flow wind

$$\alpha = \tan^{-1}(\bar{v}/U) \quad . \quad (60)$$

From the above discussion it is obvious that these quantities, which are computed from a gust penetration approach, differ from the so-called stability derivatives. To review briefly, stability derivatives are based on three types of vehicle motions.<sup>21/</sup> First, a pure pitching motion may be defined, in which a reference point on the vehicle describes a sinusoidal path in space as the vehicle moves ahead, but the vehicle axis is always aligned tangentially with the path. The angle of attack,  $\alpha$ , is always zero and the angle of pitch,  $\theta$ , varies sinusoidally. The derivatives usually computed for this motion are  $C_{Nq}$  and  $C_{Mq}$ , where  $q = \dot{\theta}$ .

A second motion, called pure plunging motion, requires the vehicle axis to remain at fixed attitude (say, horizontal) while a reference point describes a sinusoid in space (i.e., a purely translatory motion). Here, the pitch is zero and the angle of attack varies. The stability derivatives, here, are  $C_{N\dot{\alpha}}$  and  $C_{M\dot{\alpha}}$ . The third motion is most easily described by imagining a model mounted in a wind tunnel with uniform upstream flow. The model is then forced to undergo sinusoidal rotary oscillations about a reference point. It may be shown in this case that  $\alpha$  and  $\theta$  are equal, and the stability derivatives are obtainable from the other two motions as  $C_{Nq} + C_{N\dot{\alpha}}$  and  $C_{Mq} + C_{M\dot{\alpha}}$  (the so-called pitch damping coefficient).

The point we wish to stress is that none of these three situations are physically the same as sinusoidal gust penetration. Thus, the derivatives cannot correctly be compared, except in the limit as the frequency approaches zero. It is unfortunate that even the interpretation of the symbol for angle of attack,  $\alpha$ , is not consistent. For the three motions just discussed,  $\alpha$  is constant along the vehicle length (although it may be time-dependent), whereas it varies along the vehicle during gust penetration.

#### IV. APPLICATION TO SIMPLE GEOMETRICAL SHAPES

##### A. Introductory Remarks

Numerical results are presented in the following sections which illustrate the effect of frequency of sinusoidal winds on the aerodynamic characteristics for various body geometries. Frequency response calculations were carried out for five typical pointed bodies of revolution. The body geometries considered are as follows:

1. Right circular cone
2. Convex parabolic ogive
3. Concave parabolic ogive
4. Cone-cylinder
5. Ogive-cylinder

These body shapes were chosen, first, because they possess the basic types of curvature, and second, because some theoretical results are available with which to make comparisons.

The frequency response of the slope of the normal force coefficient,  $C_{N_\alpha}$ , the slope of the pitching normal coefficient,  $C_{M_\alpha}$ , and the local normal force coefficient,  $dC_{N_\alpha}/d(x/D)$ , were computed for each configuration. Both the full potential theory (noted by  $K=5$ ) and the quasi-steady potential theory ( $K=3$ ) were used in calculating  $C_{N_\alpha}$  and  $C_{M_\alpha}$ , while  $dC_{N_\alpha}/d(x/D)$  was computed using only the full potential theory.

The frequency range used corresponded to a Strouhal number range of  $0 \leq fL/U \leq 2$ , where  $f$  = frequency (Hz.),  $U$  = free stream velocity, and  $L$  = characteristic length, taken as unity. (A value of  $fL/U = 1$  corresponds to a frequency with wavelength equal to  $L$ .) The cones, ogives and nose sections of the cone-cylinders and ogive-cylinders were of unit length.

Before proceeding to a discussion of the various results obtained, we first point out a common feature which was observed and must be kept in mind in examining all of the frequency response data.

The frequency response curves obtained of the simple geometries can be cast into two main types: (1) those curves which have a maximum response at zero impressed frequency, and (2) those curves which have a



maximum response at nonzero impressed frequency. In general, the curves of the type 1 are associated with the indicial responses which reach steady-state values without undergoing an overshoot. The type 2 curves are associated with the indicial curves which exhibit an overshoot. (See Refs. 13 and 17 for the type of indicial responses indicated, and Appendix I for further discussion of the relationship between indicial and sinusoidal responses.)

The presence of a maximum response value at nonzero frequency is important. It indicates those geometries and Mach number ranges for which frequency effects are important. An underestimation of the aerodynamic coefficient could ensue if a low order frequency expansion theory were used to calculate an aerodynamic coefficient which should exhibit a maximum frequency response at a nonzero frequency. Conversely, a conservative estimation of the aerodynamic coefficient could ensue if the frequency response attenuated rapidly from a maximum value at zero impressed frequency.

#### B. Cone Results

The numerical results for the frequency response of right circular cones are presented in this section. The cone configurations considered are presented in Table II along with the Mach number range investigated.

TABLE II

CONE CONFIGURATIONS EXAMINED

<u>Semi-Vertex Angle</u>	<u>Mach Number Range</u>
2.87° ( $\epsilon = 0.05$ )*	1.25 to 3.0
5.72° ( $\epsilon = 0.10$ )	1.25 to 3.0
10°	1.25 to 3.0
15°	1.25 to 3.0
20°	1.25 to 2.5
30°	1.5 to 1.9
33°	1.667 and 1.82

\*  $\epsilon$  is the ratio of the base radius to body length (finesness ratio).

The local normal force coefficients were evaluated at the end of each cone. A pitch axis location at the nose was chosen for the cones and other simple geometries.

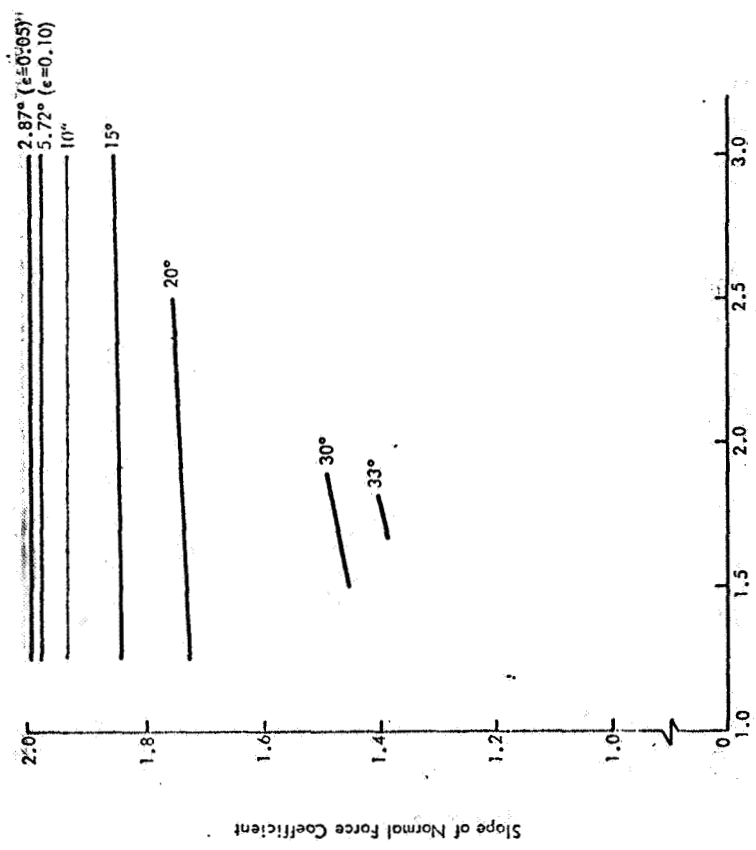
First, the zero-frequency results are examined, as a review, since this allows a direct comparison of the present results with those of other investigators.

Plots of  $C_{N_\alpha}$  and  $C_{M_\alpha}$  at zero frequency are presented in Figures 4a and 4b, respectively, for the cones examined. These plots show the influence of Mach number and cone angle on these stability derivatives.  $C_{N_\alpha}$  and  $C_{M_\alpha}$  for cones up to and including  $15^\circ$  semi-vertex angle are almost insensitive to Mach number while they tend to increase with Mach number for the  $20^\circ$ ,  $30^\circ$  and  $33^\circ$  cones. For a given Mach number the values of  $C_{N_\alpha}$  and  $C_{M_\alpha}$  are seen to become smaller with increasing semi-vertex angle. These zero-frequency values of  $C_{N_\alpha}$  and  $C_{M_\alpha}^*$  are also the maximum response values for the frequency range investigated. The only exceptions found to this were the  $K = 5$   $C_{M_\alpha}$  values for  $2.87^\circ$  cone at  $M = 1.25$  and  $1.5$ ; and the  $5.72^\circ$ ,  $10^\circ$ , and  $15^\circ$  cones at  $M = 1.25$ . The maximum  $C_{M_\alpha}$  values for these cases were not larger than 5 percent of the zero-frequency values and generally occurred at a Strouhal number of 0.15. Thus, it can be said that the frequency response curves for the cones are of type 1 with the exception of  $C_{M_\alpha}$  for slender cones at low Mach number, using the full potential theory.

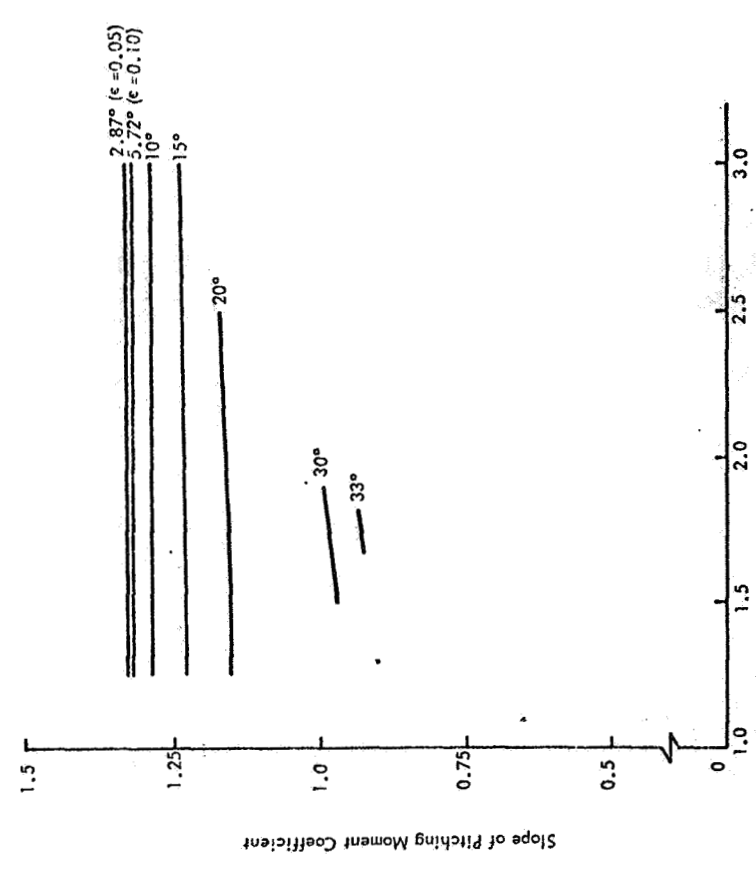
Plots of  $C_{N_\alpha}$  versus Mach number for  $2.87^\circ$  ( $\epsilon = 0.05$ ) and  $5.72^\circ$  ( $\epsilon = 0.10$ ) cones, using several theories, are presented in Figures 5a and 5b (note the expanded scale). The present zero-frequency results (noted by a solid line) are compared with the quasi-slender-body theory of Platzter-Hoffman,<sup>6</sup> Sims' exact results,<sup>22</sup> the "exact" first-order theory of Tobak and Wehrend<sup>23</sup> and slender body theory. The Platzter-Hoffman work is based on an expansion of the cross-flow potential with respect to frequency. Their results are restricted (including those restrictions imposed by linearized theory) to a value of the hypersonic similarity parameter  $2Mc < 0.3$  and by  $kM \ll (M - 1)$ . Sims' results are based on the exact nonlinear cone solution.

Slender-body theory, as to be expected, becomes more conservative (larger  $C_{N_\alpha}$  values) compared to the more accurate theories as both Mach number and cone semi-apex angle increase. The present zero-frequency results

\* The present theory dictates that the  $K = 3$  and  $5$  aerodynamic representation yield the same steady-state or zero-frequency value.

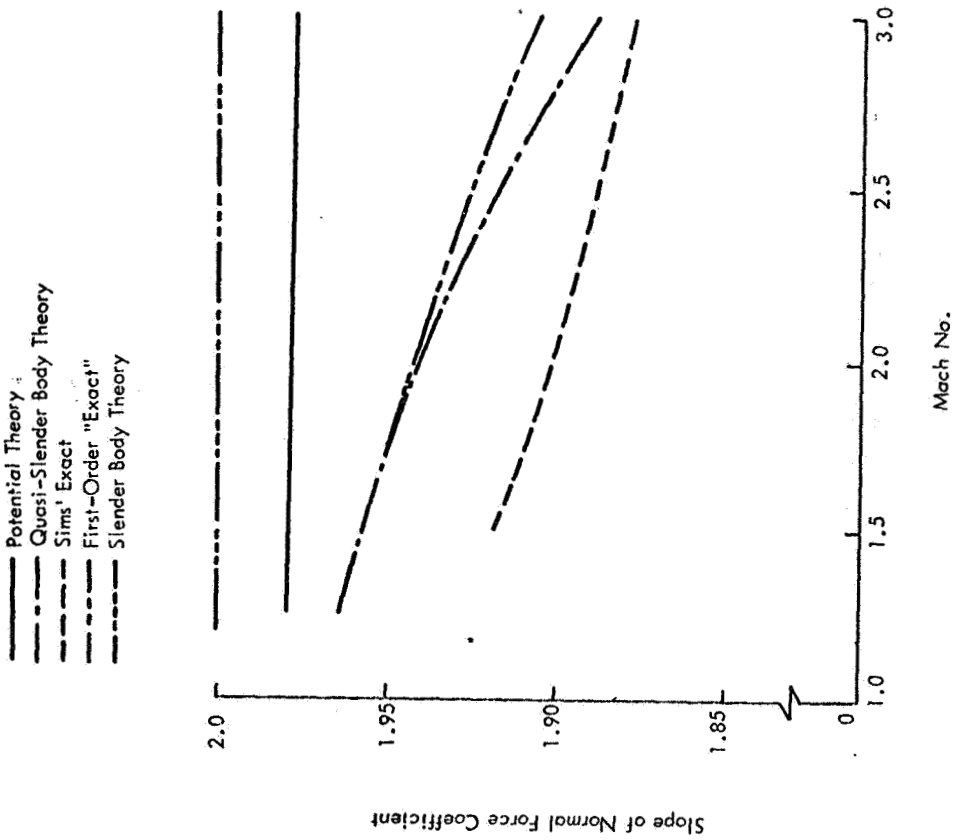


(a) Slope of Normal Force Coefficient

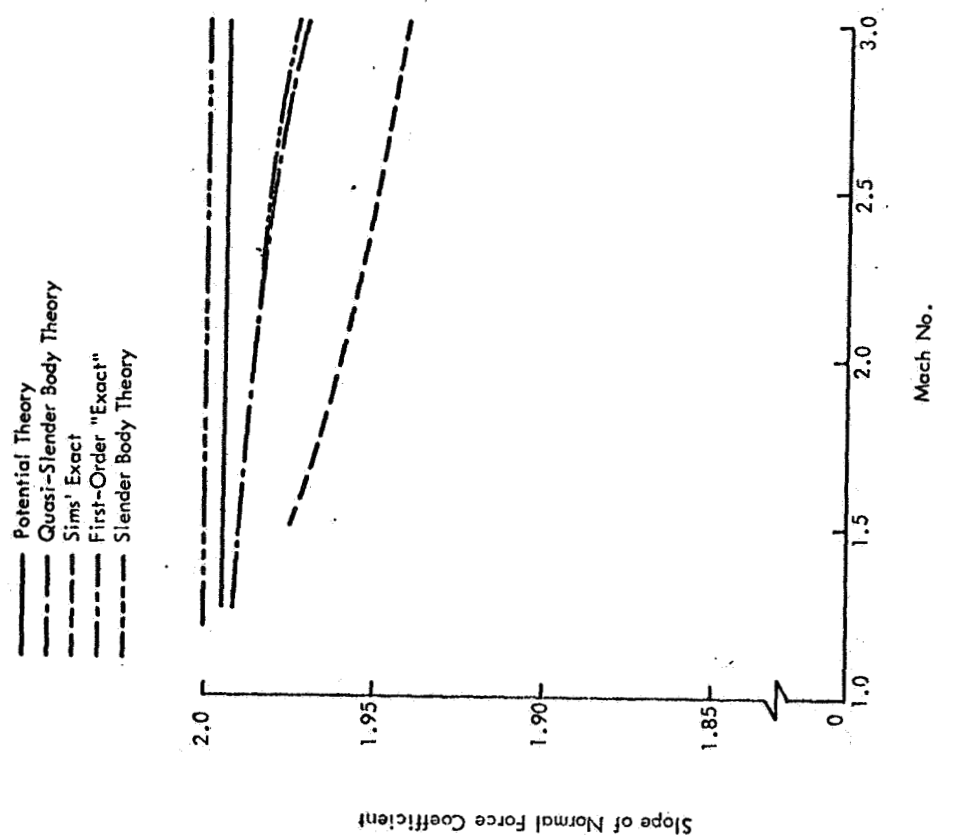


(b) Slope of Pitching Moment Coefficient

Figure 4 - Steady-State Responses Versus Mach Number for Various Cone Angles



(a) 2.87° Cone ( $\epsilon = 0.05$ )



(b) 5.72° Cone ( $\epsilon = 0.10$ )

Figure 5 - Steady-State Slope of Normal Force Coefficient Versus Mach Number for  $\epsilon = 0.05$  and  $0.10$  Cones

are slightly more conservative than the first order "exact", quasi-slender-body theory and Sims' "exact" for these two cones.

A comparison of  $C_{N_\alpha}$  values obtained from the present potential theory, with those obtained by other investigators, is given in Table III for various cones at  $M = 1.5$ . It can be seen that the agreement of the potential theory with the results of Platzter and Hoffman and Tobak and Wehrend is good for cones of semi-vertex angles up to about  $5^\circ$  to  $10^\circ$ . For cone angles of  $10^\circ$  and larger,\* the present potential theory becomes more conservative compared to those above mentioned investigators' results. However, for the larger cone angles, the potential results have the same trend and compare favorably with those obtained by Sims<sup>22/</sup> and Brong<sup>24/</sup>

The effect of frequency on the aerodynamic characteristics will now be discussed.

Plots of the frequency response of  $C_{N_\alpha}$  and  $C_{M_\alpha}$  are presented in Figures 6a through 10b for various cones at Mach number of 1.5. The results obtained from the quasi-steady potential theory ( $K = 3$ ) are given by the solid line while the full potential theory results ( $K = 5$ ) are given by the dashed line.

All of the  $C_{N_\alpha}$  curves have about the same character. The response attenuates with increasing frequency; and the rate of attenuation is greater with the full potential theory. No resonances occur in the frequency range investigated.

The  $C_{M_\alpha}$  curves also have about the same character. Again, no resonances are observed. For slender cones the  $K = 5$  response is nearly flat for low frequencies, and then drops off rapidly. For the larger cones the response attenuates with frequency more rapidly for  $K = 5$  than for the quasi-steady case.

Values of  $C_{N_\alpha}$  and  $C_{M_\alpha}$  are predicted by the exact theory of Sims<sup>6,22/</sup> are plotted on the zero-frequency axis in Figures 6 through 9 for purposes of comparison.

---

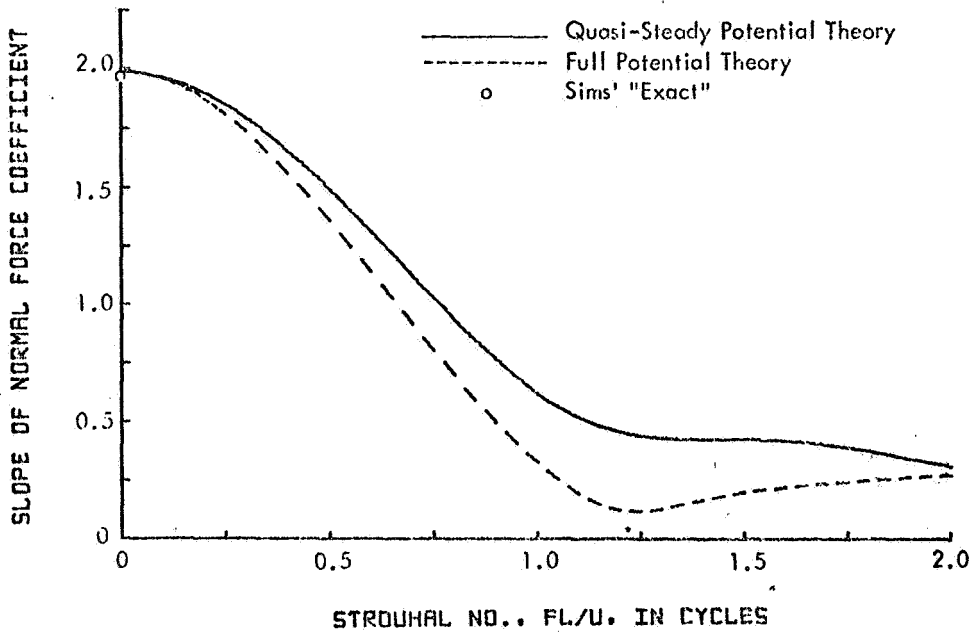
\* The deviation of the potential theory results from those of Platzter and Hoffman for cone angles of  $10^\circ$  and larger is to be expected since  $2Mc > 0.3$  for these cone angles at  $M = 1.5$ .

TABLE III

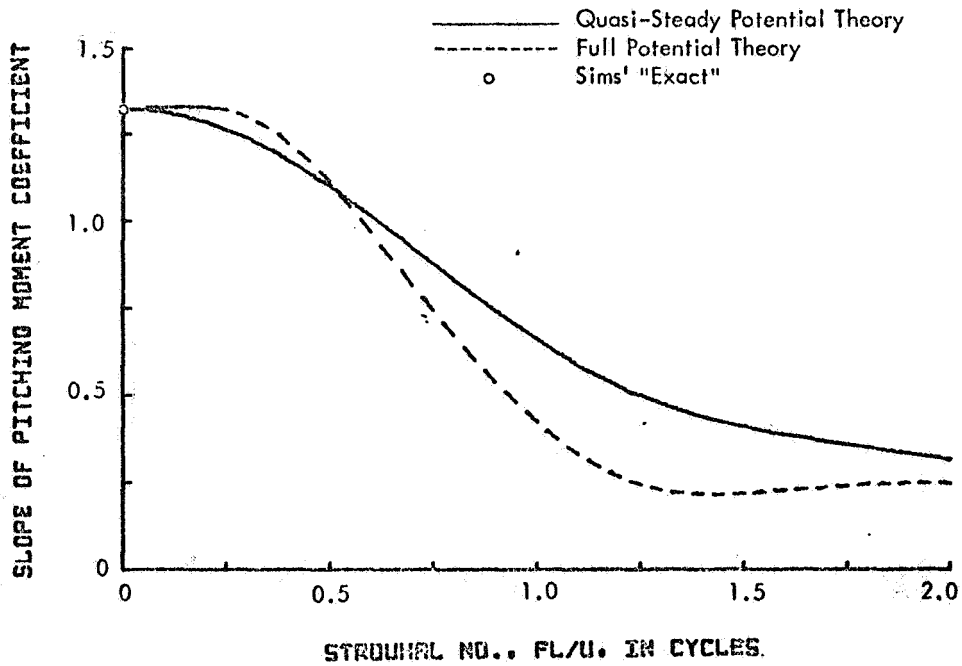
$C_{N\alpha}$  VALUES FOR VARIOUS CONES AT  $M = 1.5$

Cone Semi-Vertex Angle	Full Potential Theory ( $w = 0$ )	Platzner & Hoffman (Ref. 6)	Tobak & Wehrend (Refs. 6 & 23)	Sims (Refs. 6 & 22)	Brong* (Ref. 24)	Slender- Body Theory
2.87°	1.9948	1.989	1.989	1.9725	-	2.0
5.72°	1.9786	1.956	1.956	1.918	-	2.0
10°	1.9316	1.8679	1.87	1.83	1.84	2.0
15°	1.8447	1.6949	-	1.718	1.71	2.0
20°	1.7306	1.4370	1.50	1.605	1.60	2.0
30°	1.4563	0.5833	-	-	-	2.0

\* The analysis of Brong is based on a time-dependent perturbation about the nonlinear Taylor-Moccoll-solution.

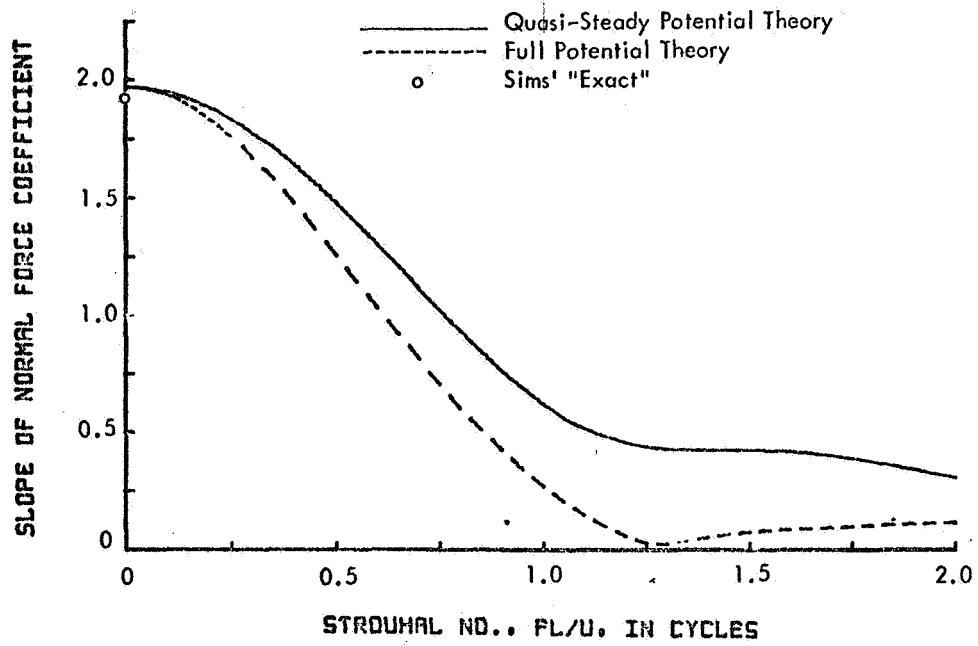


(a) Slope of Normal Force Coefficient

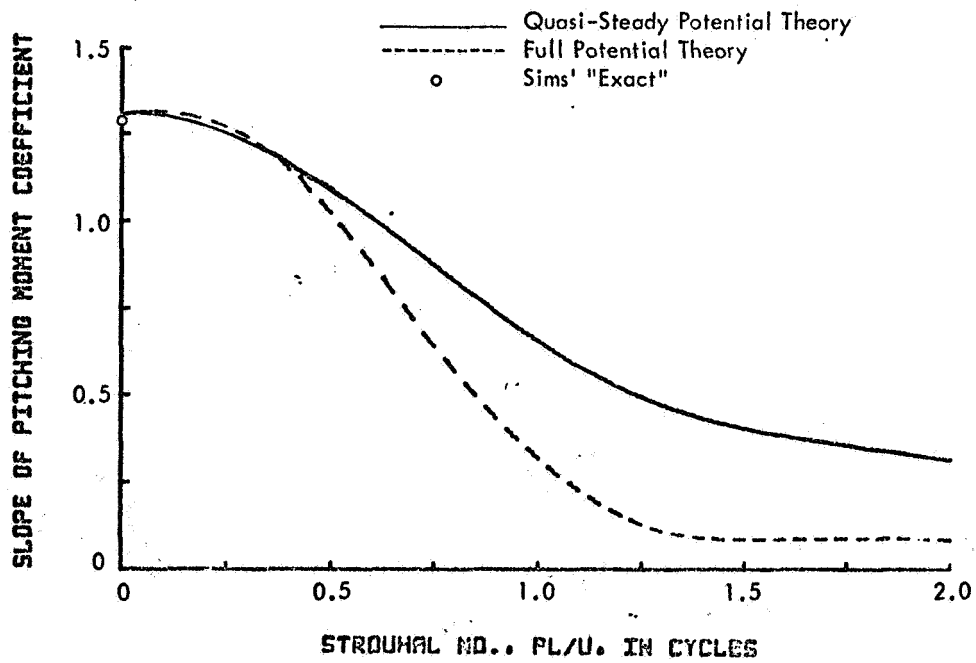


(b) Slope of Pitching Moment Coefficient

Figure 6 - Aerodynamic Frequency Responses for a  $2.87^\circ$   
 $(\epsilon = 0.05)$  Cone at  $M = 1.5$



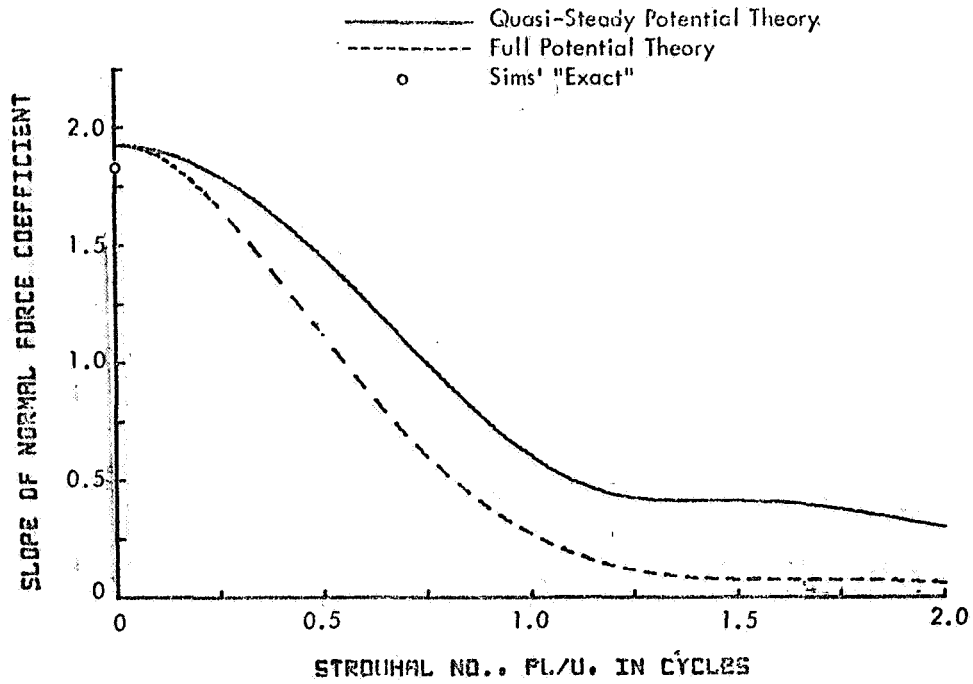
(a) Slope of Normal Force Coefficient



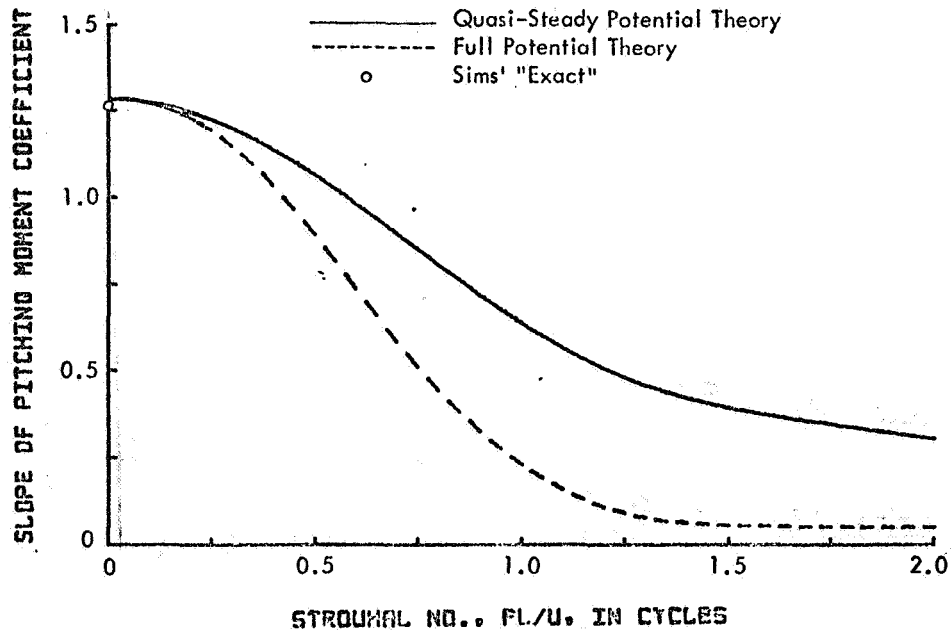
(b) Slope of Pitching Moment Coefficient

Figure 7 - Aerodynamic Frequency Responses for a  $5.72^\circ$   
 ( $\epsilon = 0.10$ ) Cone at  $M = 1.5$



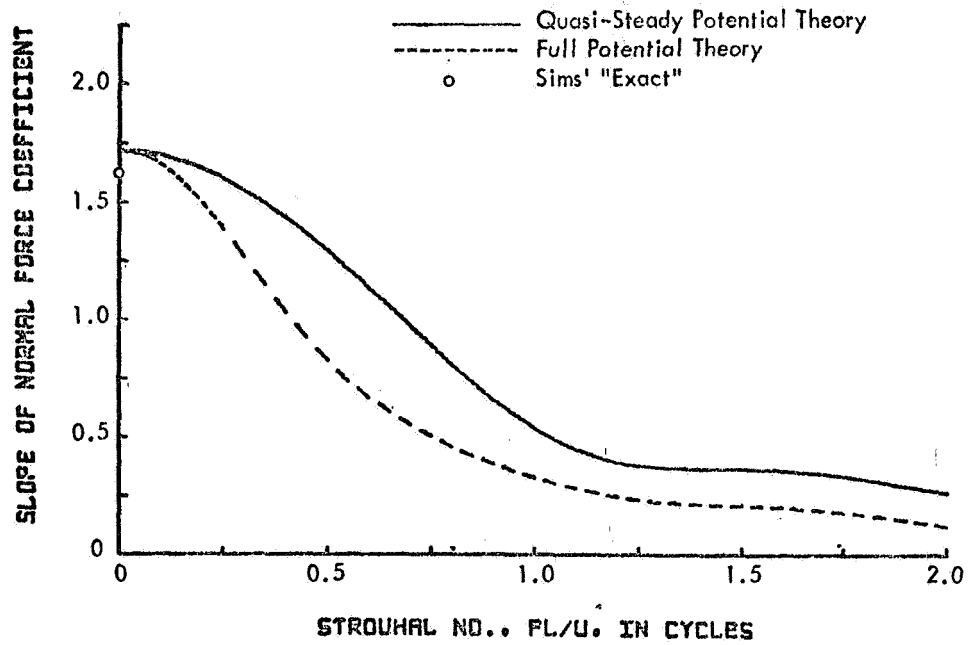


(a) Slope of Normal Force Coefficient

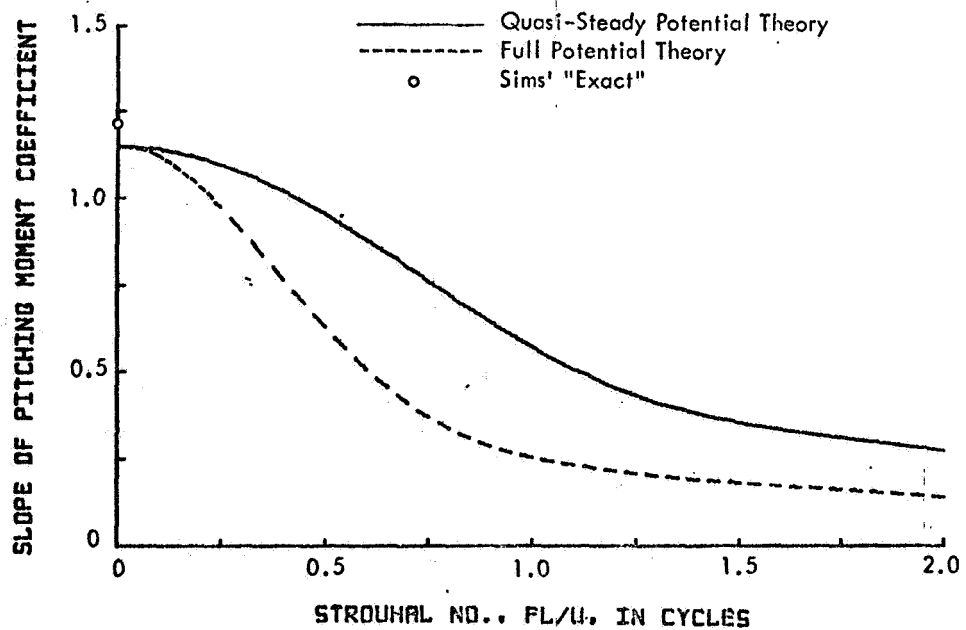


(b) Slope of Pitching Moment Coefficient

Figure 8 - Aerodynamic Frequency Responses for a  $10^\circ$  Cone at  $M = 1.5$

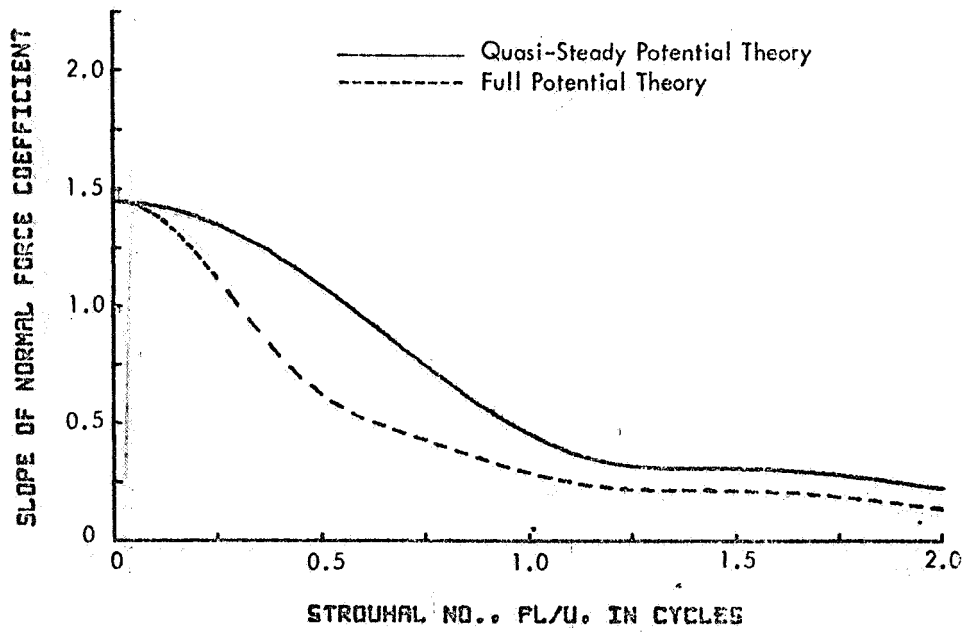


(a) Slope of Normal Force Coefficient

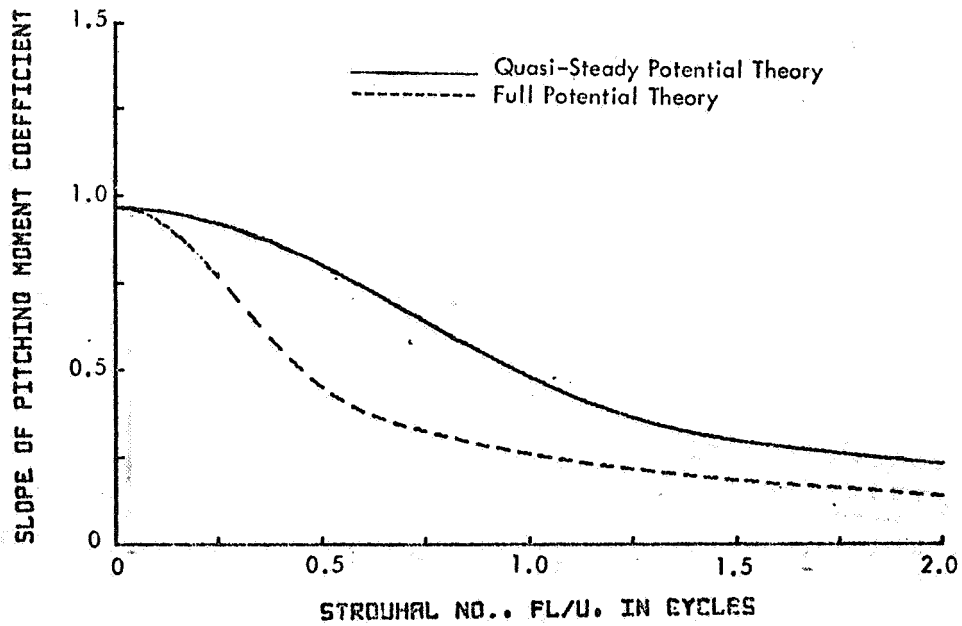


(b) Slope of Pitching Moment Coefficient

Figure 9 - Aerodynamic Frequency Responses for a 20° Cone at M = 1.5



(a) Slope of Normal Force Coefficient



(b) Slope of Pitching Moment Coefficient

Figure 10 - Aerodynamic Frequency Responses for a  $30^\circ$  Cone at  $M = 1.5$

The effects of Mach number on the frequency response of  $C_{N_\alpha}$  and  $C_{M_\alpha}$  for a  $10^\circ$  cone are shown in Figure 11. The quasi-steady theory is insensitive to Mach number; however, the  $K = 5$  curves are dependent on Mach number. It is seen that as the Mach number increases, the  $K = 5$  curve approaches the  $K = 3$  curve. This is to be expected since the aerodynamic inertia effects tend to decrease with increasing Mach number.

The frequency response curves of  $dC_{N_\alpha}/d(x/D)$  for all the cones are of the type 1 curve, i.e., the curves have a maximum value at zero-frequency, then attenuate as frequency increases. The zero-frequency values of  $dC_{N_\alpha}/d(x/D)$  increase with increasing cone angle (0.3990 for  $\epsilon = 0.05$  and 3.61 for  $33^\circ$ ). The attenuation of the frequency response curves has a tendency to become more rapid as cone angle increases. For each individual cone, the shape and rate of attenuation of the frequency response curves are almost independent of Mach number.

### C. Convex and Concave Parabolic Ogive Results

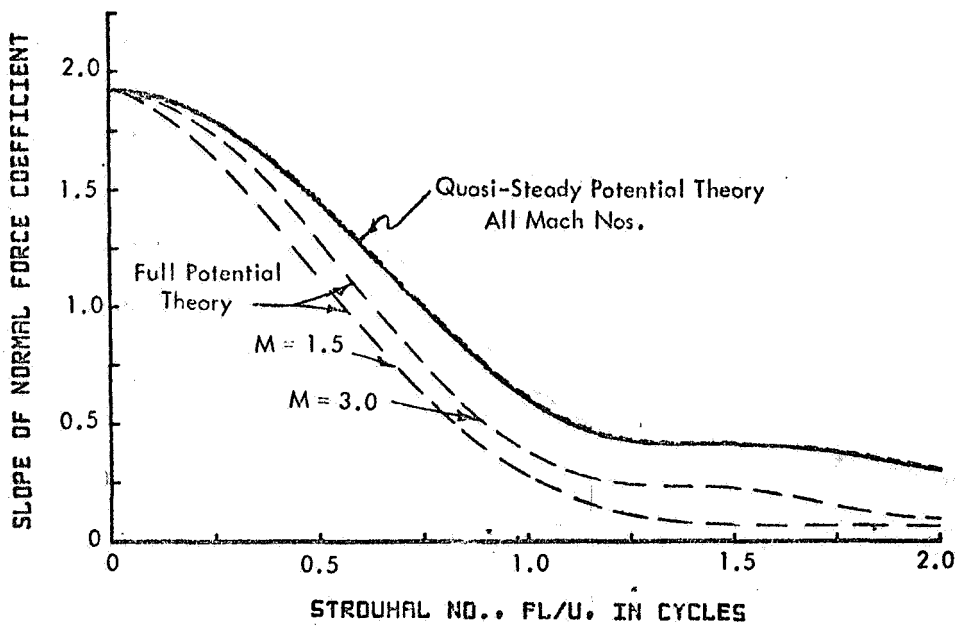
The numerical results for the frequency response of convex and concave ogives are presented in this section. The body geometry of the ogives is the same as that used in Ref. 6:

$$\begin{aligned} \text{Convex ogive, } R(x) &= \epsilon x(2-x) & 0 \leq x \leq 1 \\ \text{Concave ogive, } R(x) &= \frac{\epsilon x}{2} (1+x) & 0 \leq x \leq 1 \end{aligned} ,$$

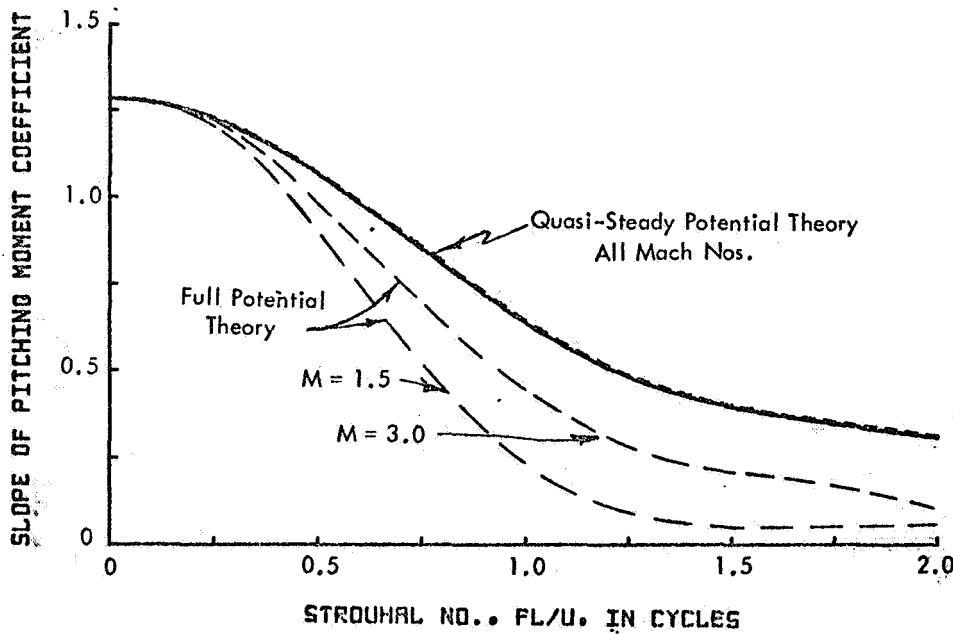
where  $\epsilon$  is the fineness ratio. Two values of body fineness ratio,  $\epsilon = 0.05$  and  $0.10$  were investigated for each type of ogive. Frequency response calculations for the aerodynamic characteristics were carried out for each of the four configurations over a Mach number range from 1.2 to 3.0. The local normal force coefficients were evaluated at the end of each body geometry ( $x = 1$ ).

Plots of  $C_{N_\alpha}$  and  $C_{M_\alpha}$  at zero frequency versus Mach number for the convex ogives are presented in Figures 12a and 12b and for the concave ogives in Figures 13a and 13b, respectively. The present zero-frequency results\* (noted by a solid line) are composed with quasi-slender-body theory results,<sup>2</sup> Sims' method of characteristics,<sup>6,25</sup> and slender-body theory.

\* The zero-frequency values of  $C_{N_\alpha}$  and  $C_{M_\alpha}$  are also the maximum response values for the frequency range investigated. The effect of frequency on the ogive stability derivatives will be discussed shortly.

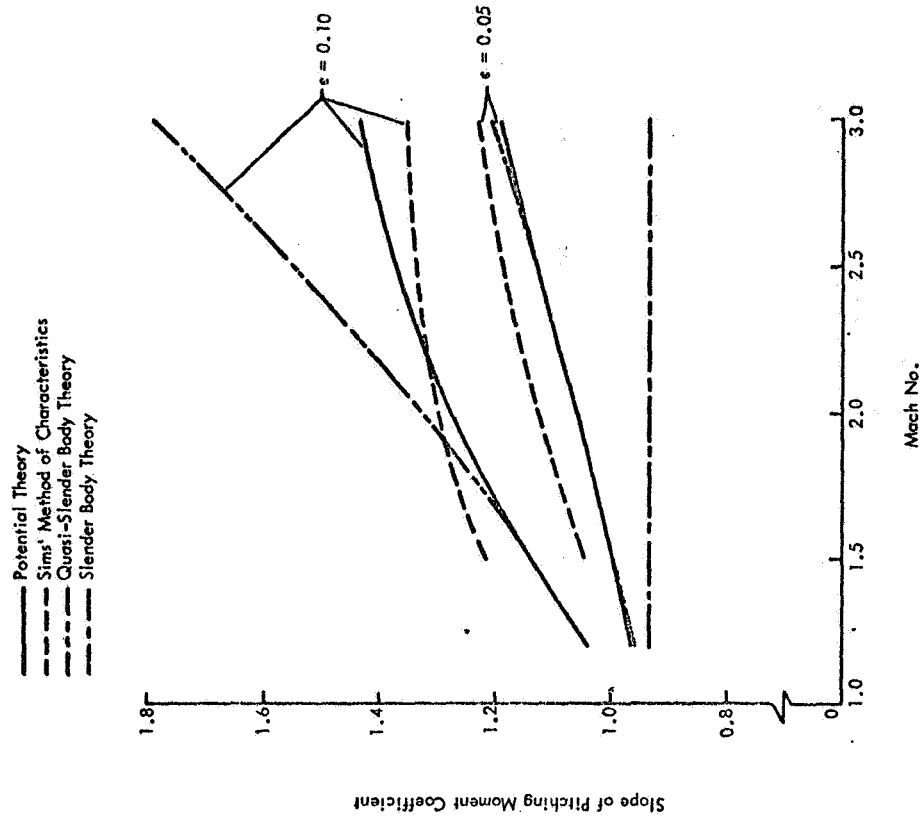


(a) Slope of Normal Force Coefficient

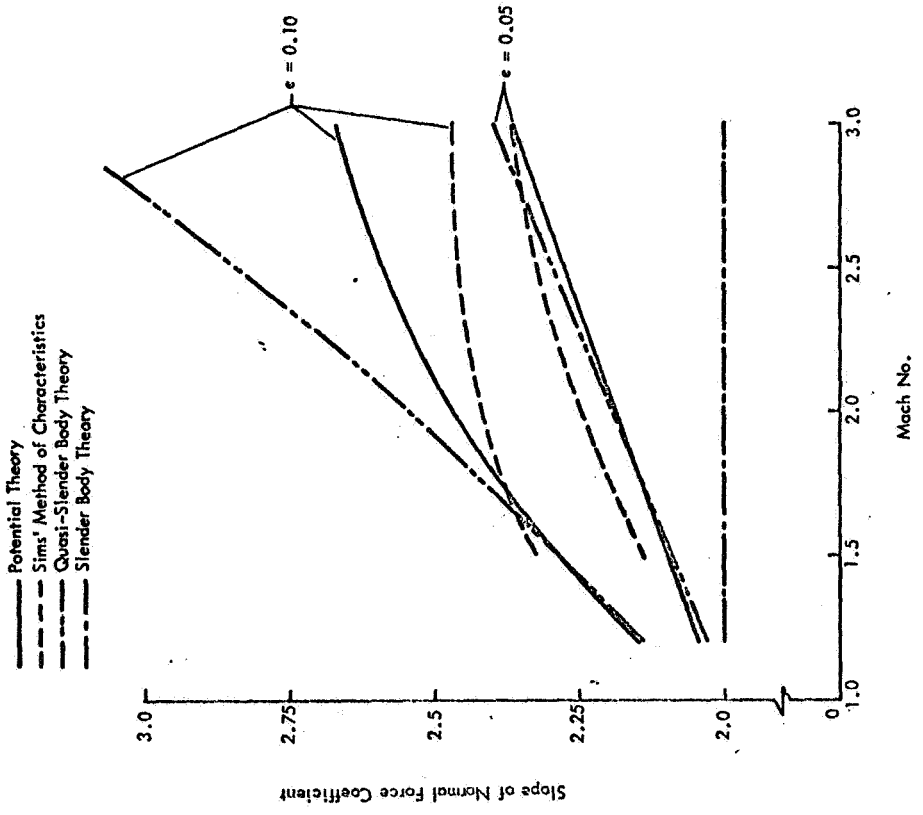


(b) Slope of Pitching Moment Coefficient

Figure 11 - Aerodynamic Frequency Responses for a  $10^\circ$  Cone at Various Mach Numbers

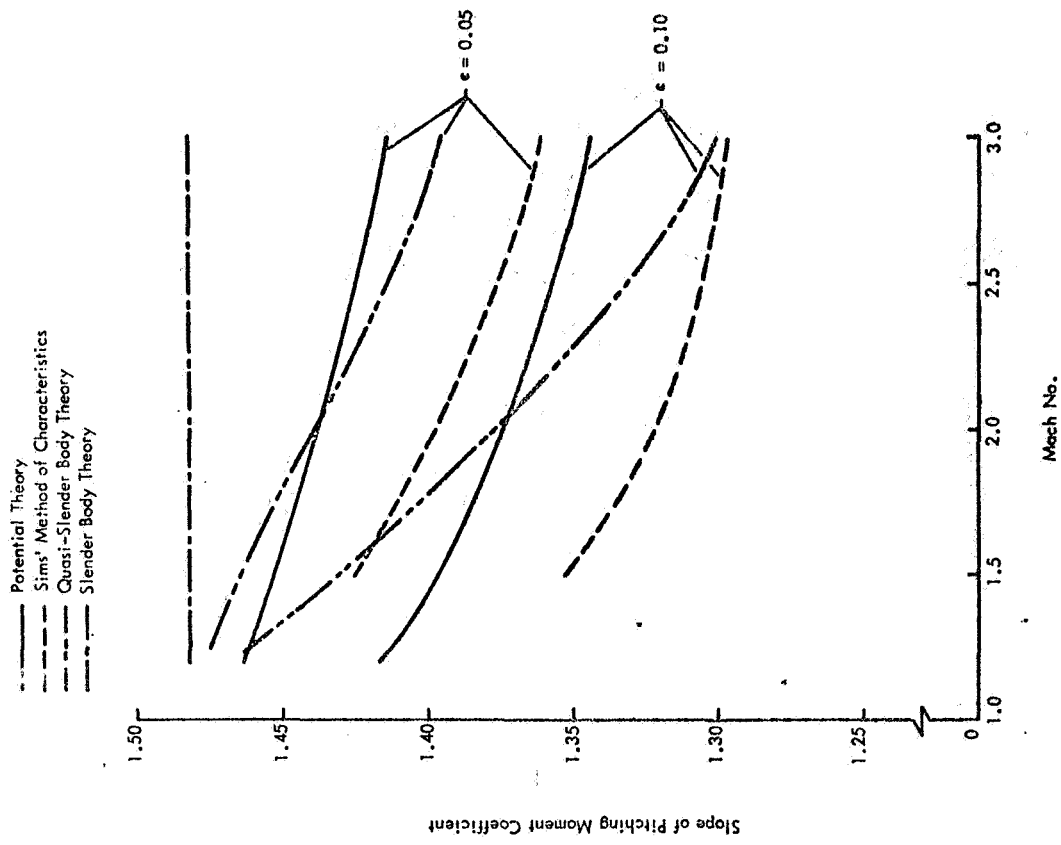


(a) Slope of Normal Force Coefficient

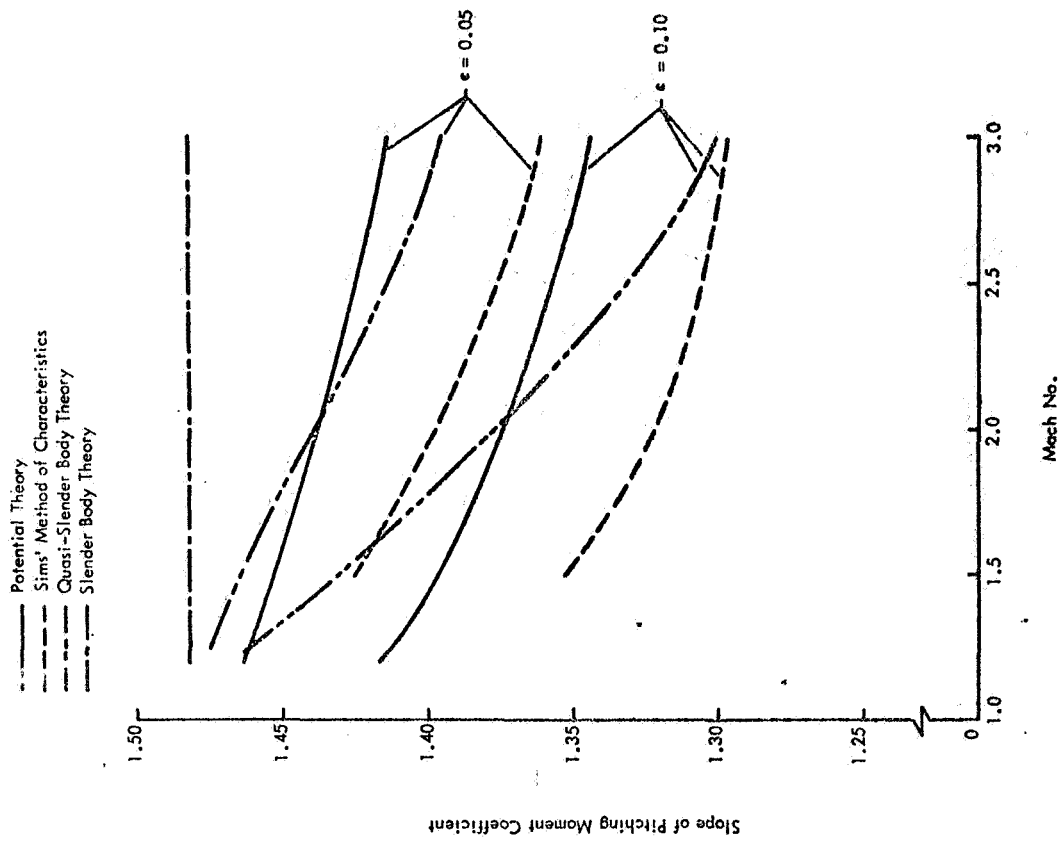


(b) Slope of Pitching Moment Coefficient

Figure 12 - Steady-State Responses Versus Mach Number for  $\epsilon = 0.05$  and  $0.10$  Convex Ogives



(a) Slope of Normal Force Coefficient



(b) Slope of Pitching Moment Coefficient

Figure 13 - Steady-State Responses Versus Mach Number for  $\epsilon = 0.05$  and  $0.10$  Concave Ogives

These plots show a significant influence of Mach number and body thickness on the two stability derivatives (except for slender-body theory which is independent of both Mach number and body thickness). The three more accurate theories show that the convex ogive  $C_{N_\alpha}$  and  $C_{M_\alpha}$  values increase with both Mach number and body thickness, while the opposite is true for the concave ogives. Closer agreement between the present results and those of quasi-slender-body theory is obtained for the  $\epsilon = 0.05$  ogives than for the  $\epsilon = 0.10$  ogives.

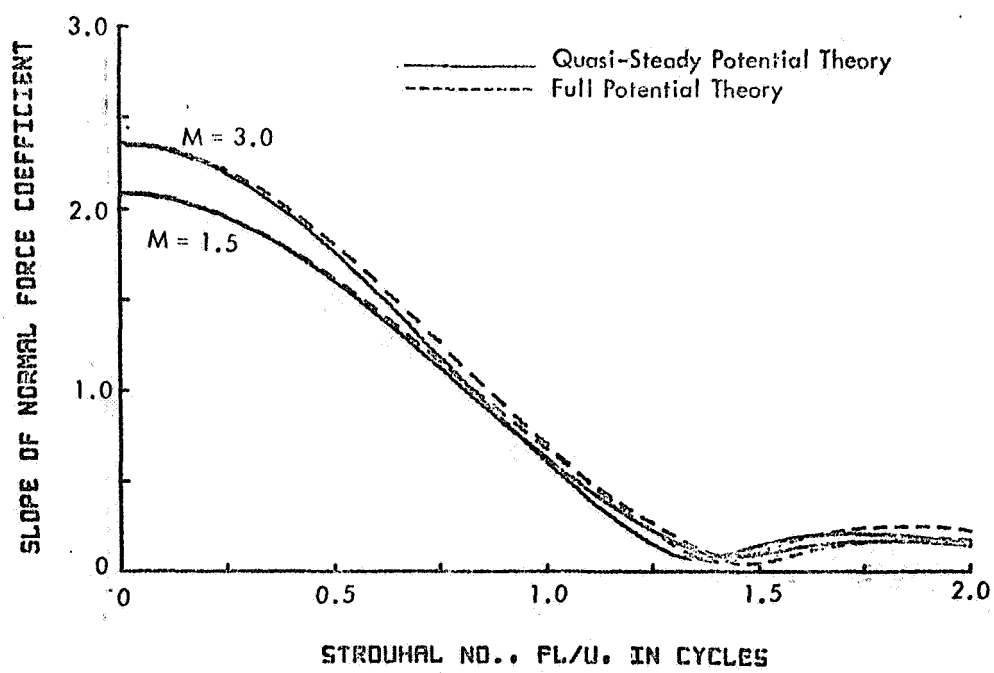
The zero-frequency potential theory results for both ogives exhibit about the same trend with Mach number and body thickness as do the exact results of Sims. For the convex ogives the present  $C_{N_\alpha}$  and  $C_{M_\alpha}$  results agree well with Sims' results, with the worst agreement being an 8 percent overestimate of  $C_{N_\alpha}$  at  $M = 3$  for the 0.10 fineness ratio.  $C_{N_\alpha}$  and  $C_{M_\alpha}$  for the concave ogives, as predicted by potential theory, are consistently conservative compared to Sims' results for the Mach number range investigated; the largest discrepancies are 4 percent for  $\epsilon = 0.05$  and 4.6 percent for the  $\epsilon = 0.10$  concave ogive, occurring near the high Mach number end.

The effects of frequency on the ogive stability derivatives will now be discussed. Plots of the frequency response of  $C_{N_\alpha}$  and  $C_{M_\alpha}$  for the ogives are presented in Figures 14a through 17b for  $M = 1.5$  and  $3.0$ . The results obtained from the quasi-steady potential theory ( $K = 3$ ) are given by the solid line while the full potential theory results ( $K = 5$ ) are given by the dashed line.

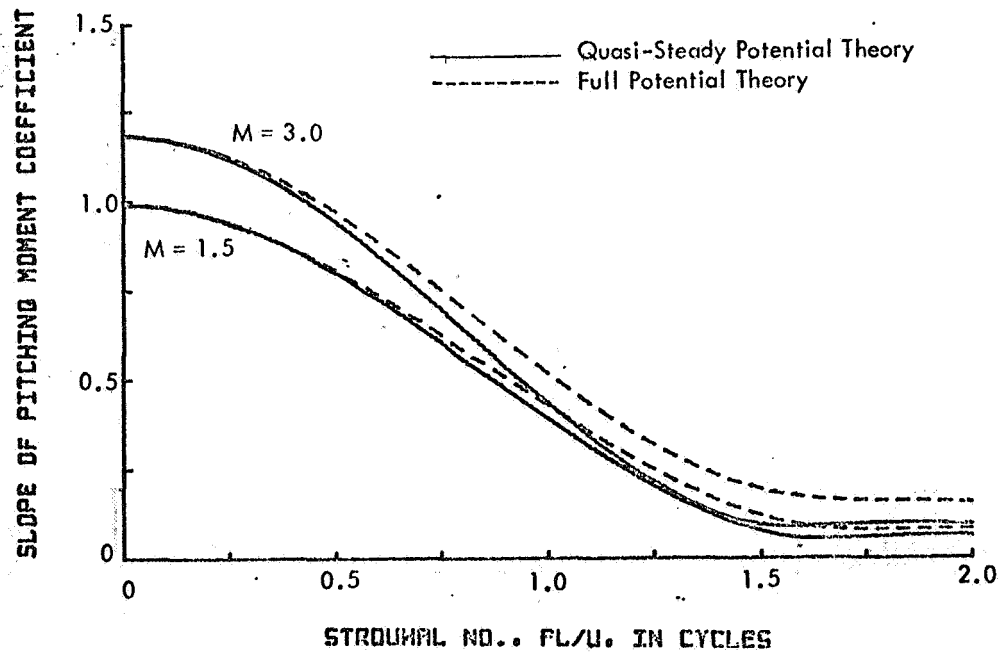
All of the ogive frequency response curves are of type 1 in that the maximum response occurs at zero frequency. The  $C_{N_\alpha}$  curves for the convex ogives attenuate to a minimum value (between a Strouhal number of 1.25 and 1.5) followed by a small rise to a second maximum. The  $C_{M_\alpha}$  convex ogive curves behave similarly, except that the minimum occurs (if one is present) at higher Strouhal numbers. The more accurate theory, full potential theory, tends to give slightly higher results than the quasi-steady theory.

The  $C_{N_\alpha}$  and  $C_{M_\alpha}$  curves for the concave ogives also attenuate as frequency increases. The full potential theory here leads to values which are smaller than the corresponding quasi-steady results. The stability derivative curves are seen to be almost independent of Mach number, with the exception of the  $K = 5$  curves for  $\epsilon = 0.10$ , which show a mild Mach number dependence at the very high frequencies.



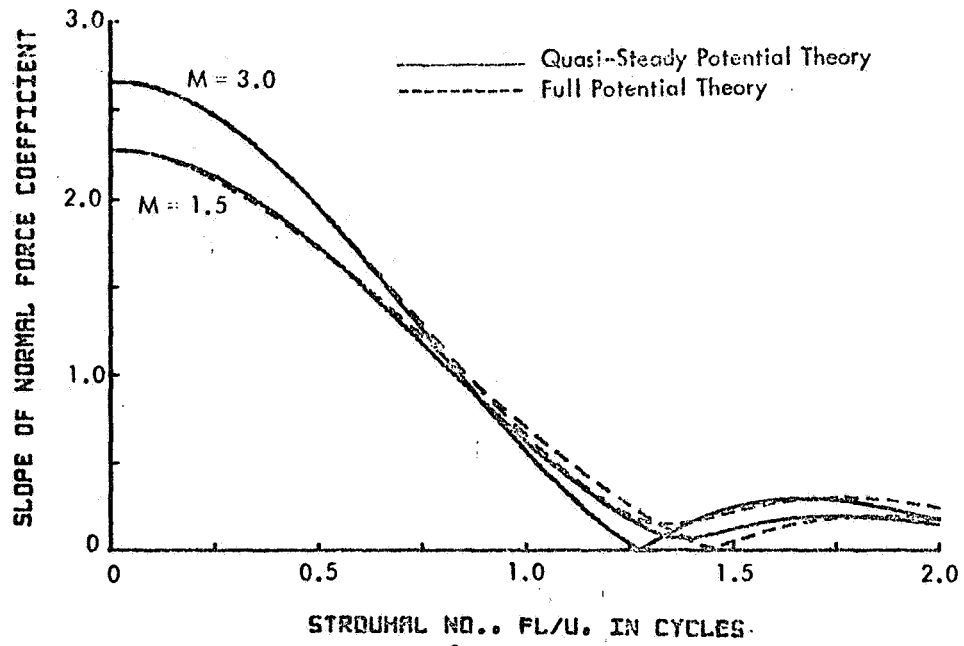


(a) Slope of Normal Force Coefficient

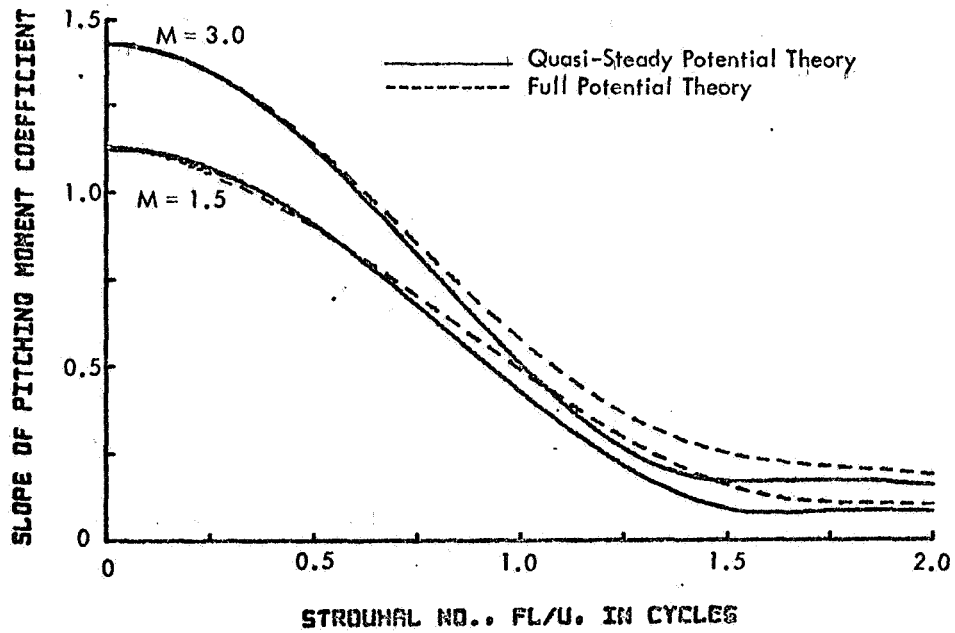


(b) Slope of Pitching Moment Coefficient

Figure 14 - Aerodynamic Frequency Responses for an  $\epsilon = 0.05$  Convex Ogive at  $M = 1.5$  and  $3.0$

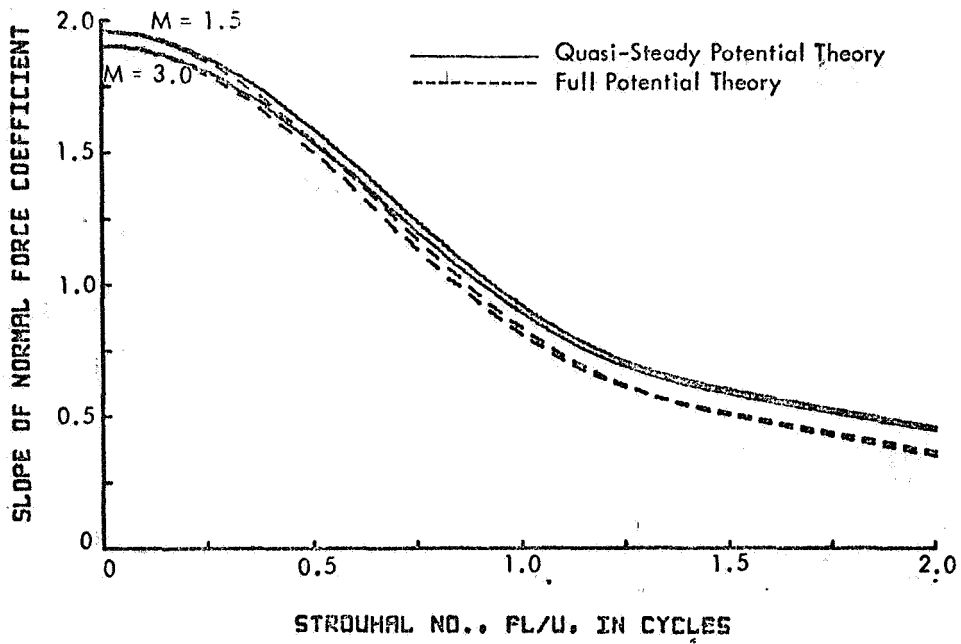


(a) Slope of Normal Force Coefficient

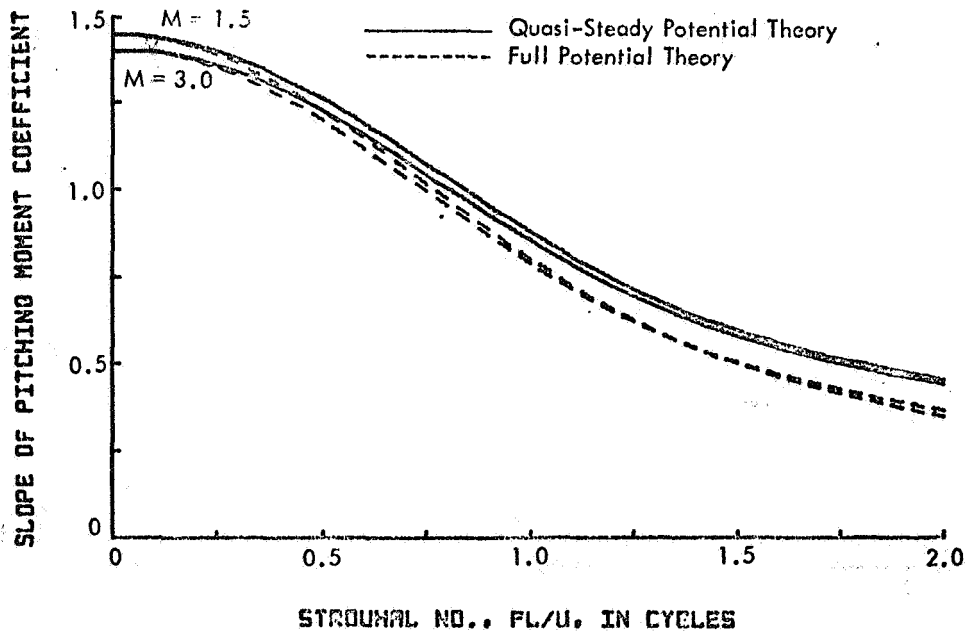


(b) Slope of Pitching Moment Coefficient

Figure 15 - Aerodynamic Frequency Responses for an  $\epsilon = 0.10$  Convex Ogive at  $M = 1.5$  and  $3.0$

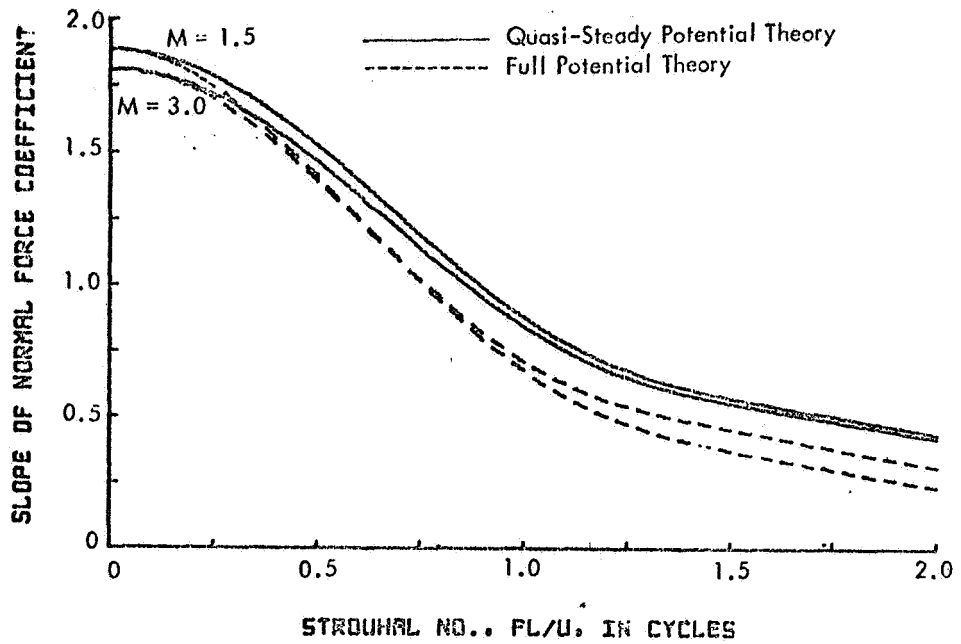


(a) Slope of Normal Force Coefficient

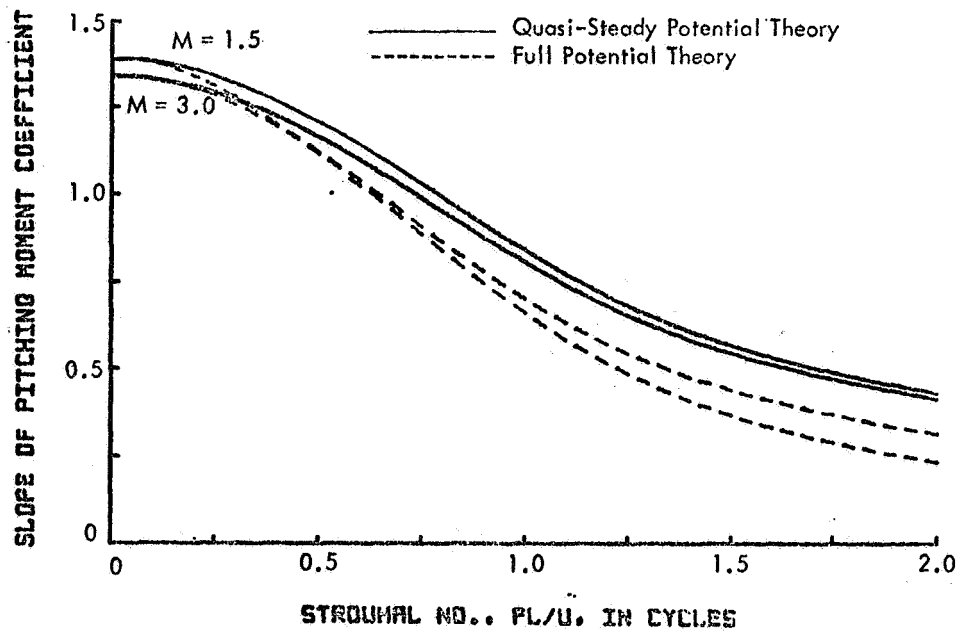


(b) Slope of Pitching Moment Coefficient

Figure 16 - Aerodynamic Frequency Responses for an  $\epsilon = 0.05$   
Concave Ogive at  $M = 1.5$  and  $3.0$



(a) Slope of Normal Force Coefficient



(b) Slope of Pitching Moment Coefficient

Figure 17 - Aerodynamic Frequency Responses for an  $\epsilon = 0.10$  Concave Ogive at  $M = 1.5$  and  $3.0$

The frequency response curves of  $dC_{N\alpha}/d(x/D)$  for the convex ogives (not reproduced here) are of type 2 (maximum response value located at nonzero frequency), while the concave ogives are of type 1. For a given Mach number, the maximum value of  $dC_{N\alpha}/d(x/D)$  for the convex ogives increases as  $\epsilon$  increases. Also, the maximum value increases in magnitude and moves toward higher frequencies as the Mach number increases. The frequency responses of  $dC_{N\alpha}/d(x/D)$  for the concave ogives are very similar to those found for cones. However, here, the curves are slightly more Mach number dependent as fineness ratio increases.

#### D. Cone-Cylinder Results

The numerical results for the frequency response of cone-cylinders are presented in this section. The cone-cylinder configurations considered are presented in Table IV along with the Mach number range investigated.

TABLE IV

CONE-CYLINDER CONFIGURATIONS EXAMINED

<u>Semi-Vertex Angle</u>	<u>Mach Number Range</u>
5°	2.0
10°	1.25 to 3.0
20°	1.25 to 2.5

The 5° cone-cylinder was 20 calibers (diameters) long, while the 10° and 20° cone-cylinders were each 10 calibers long. The slope of the pitching moment coefficient,  $C_{M\alpha}$ , uses the cylinder diameter as a reference length.

Figure 18 shows the steady-state local normal force coefficient on a 5° cone-cylinder for Mach number 2.0, and indicates excellent agreement between the present potential theory and the exact solution.<sup>25/</sup> (See Refs. 6 and 17 for a complete discussion of the steady-state results.) Also shown in the figure is a half cross section of the configuration with various station locations indicated. Station 1 corresponds to the shoulder, while station 8 is at the aft end of the configuration. The frequency responses of the local normal force coefficients were evaluated at  $M = 2.0$  for these various stations from the shoulder to the end of the configuration. In addition, the local normal force coefficients were computed near the point of maximum negative steady-state  $dC_{N\alpha}/d(x/D)$  for the 10° and 20° cone-cylinder.

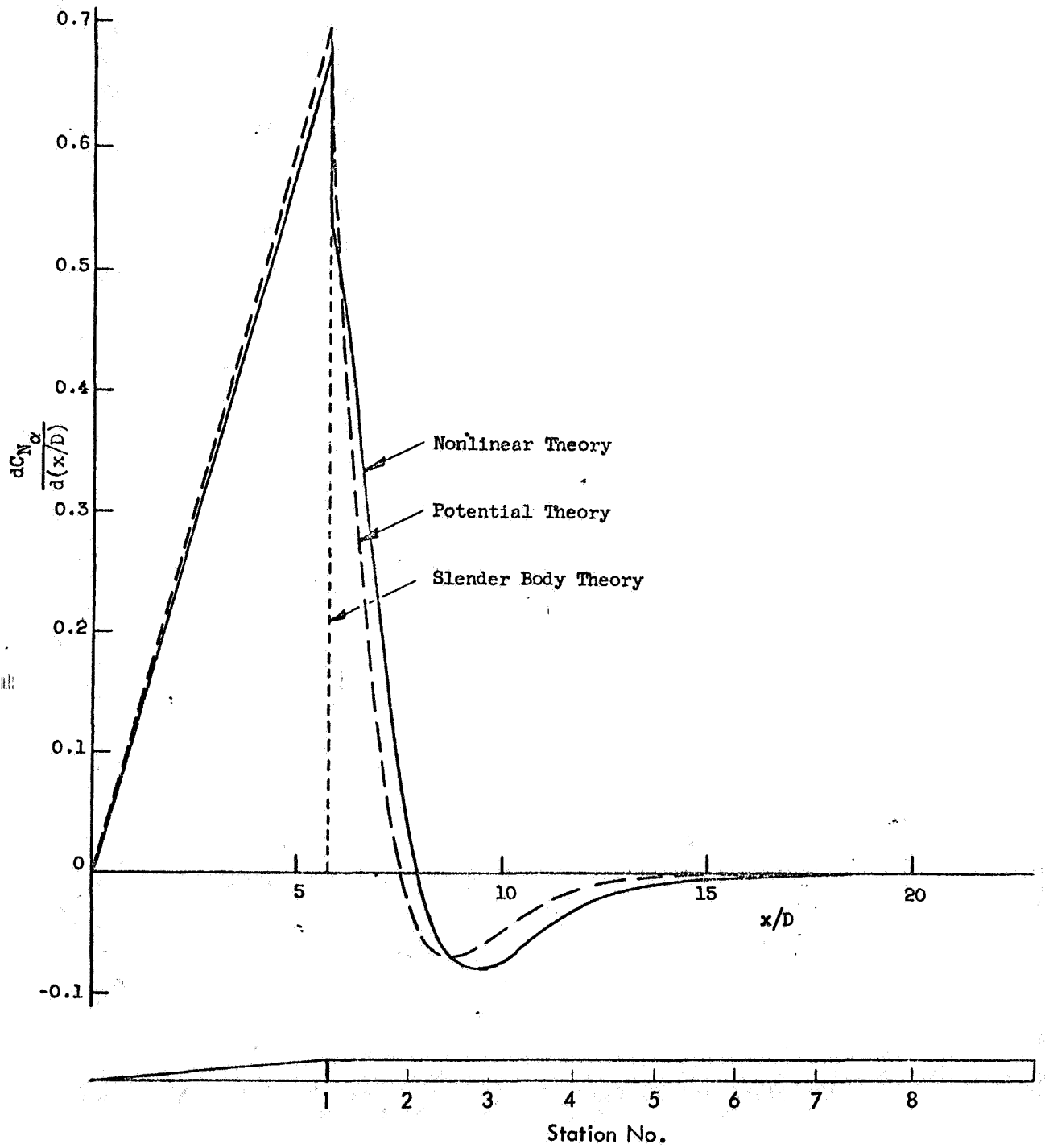


Figure 18 - Local Normal Force Coefficient for a 5° Cone-Cylinder at  $M = 2.0$

Typical steady-state, total indicial response results for the cone-cylinders examined were presented in previous publications 6,17/ These results were compared with slender-body theory and with the exact results of Sims.<sup>25/</sup> The present potential theory and Sims' exact method were found to yield nearly the same  $C_{N\alpha}$  values for the  $5^\circ$  cone-cylinder, whereas the slender-body theory is more than 10 percent low. Similar results were found for the  $10^\circ$  cone-cylinder  $C_{N\alpha}$  values, where slender-body theory was unconservative by over 30 percent.

Figure 19 shows a typical indicial lift growth curve for a cone-cylinder. The overshoot in the response to a unit step is indicative of an underdamped system (see Appendix I). Thus, a type 2 frequency response curve (exhibiting a resonance condition) is to be expected. The following discussion exemplifies this prediction.

Typical plots of the frequency response of  $C_{N\alpha}$  and  $C_{M\alpha}$  are presented in Figures 20a and 20b for the three cone-cylinder configurations at  $M = 2.0$ . (These results are obtained from the quasi-steady potential theory.) The results indicate that the response amplification at resonance increases with increasing cone angle. Furthermore, the resonance occurs at lower frequency for the larger cone angles. More will be said concerning the maximum response values of  $C_{N\alpha}$  and  $C_{M\alpha}$  after the effect of aerodynamic representation is discussed.

The effects of the aerodynamic representation on the frequency responses of  $C_{N\alpha}$  and  $C_{M\alpha}$  for the three cone-cylinders are shown in Figures 21a through 23b for  $M = 2.0$ . The quasi-steady ( $K = 3$ ) results are given by the solid curves, while the full potential theory ( $K = 5$ ) results are given by the dashed curves. The latter results, for the  $20^\circ$  cone-cylinder, are questionable beyond a Strouhal number of about 1.0 because of loss of numerical resolution. The other curves are considered valid for the frequency range shown.

In general, the  $K = 5$  curves for both  $C_{N\alpha}$  and  $C_{M\alpha}$  have slightly larger maximum response values than their  $K = 3$  counterpart. There is a tendency toward a frequency shift for the maximum values in going from the  $K = 3$  to the  $K = 5$  curves.

The dominant features of the  $C_{N\alpha}$  and  $C_{M\alpha}$  frequency response data for the  $10^\circ$  and  $20^\circ$  cone-cylinder data are summarized in Figures 24a and 24b.

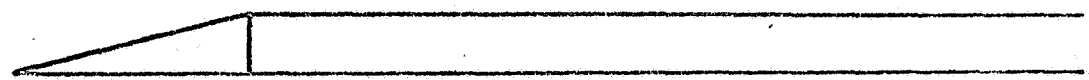
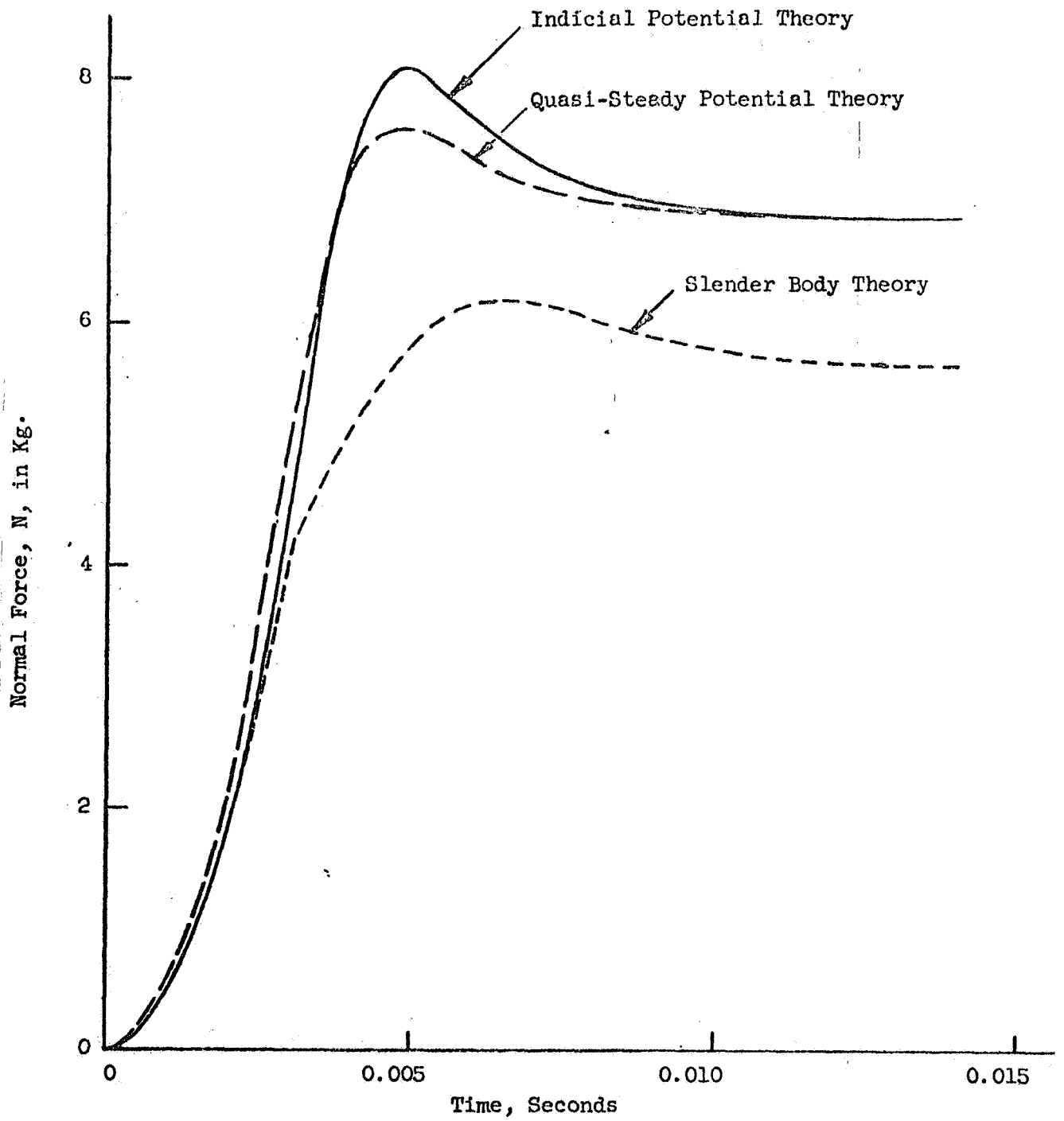
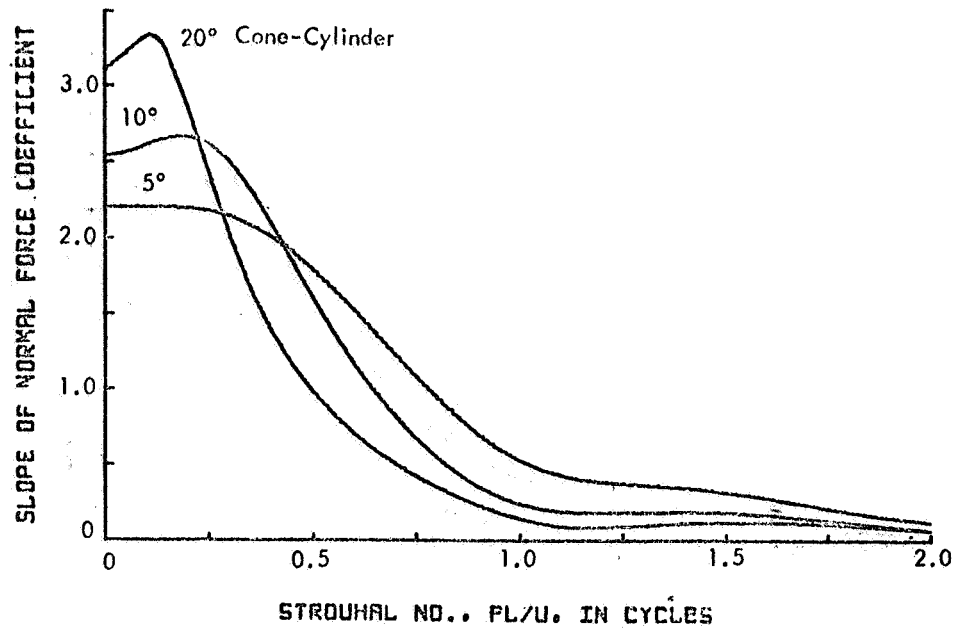
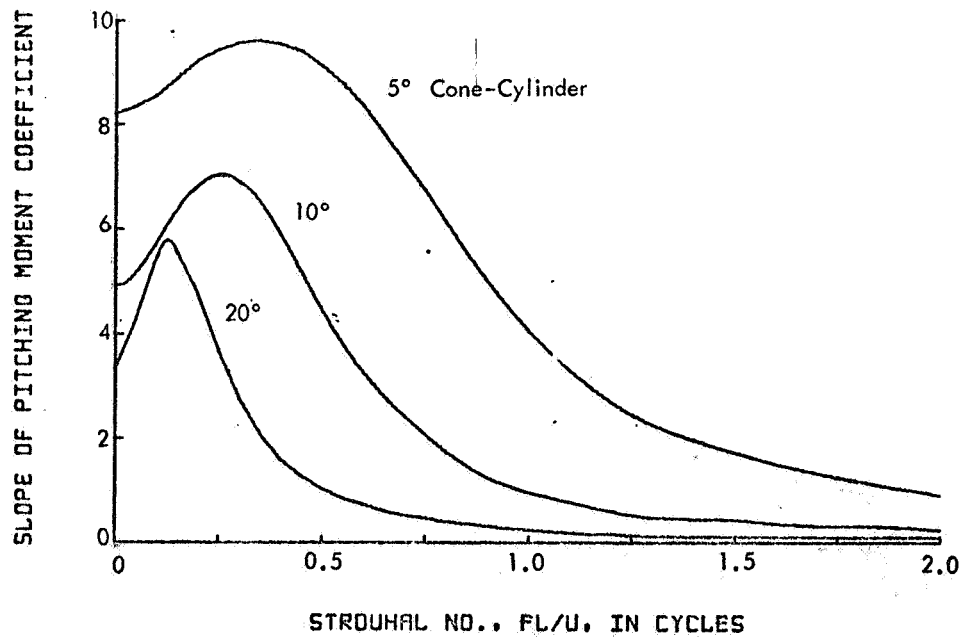


Figure 19 - Unsteady Normal Force for 15° Cone-Cylinder at  $M = 1.35$



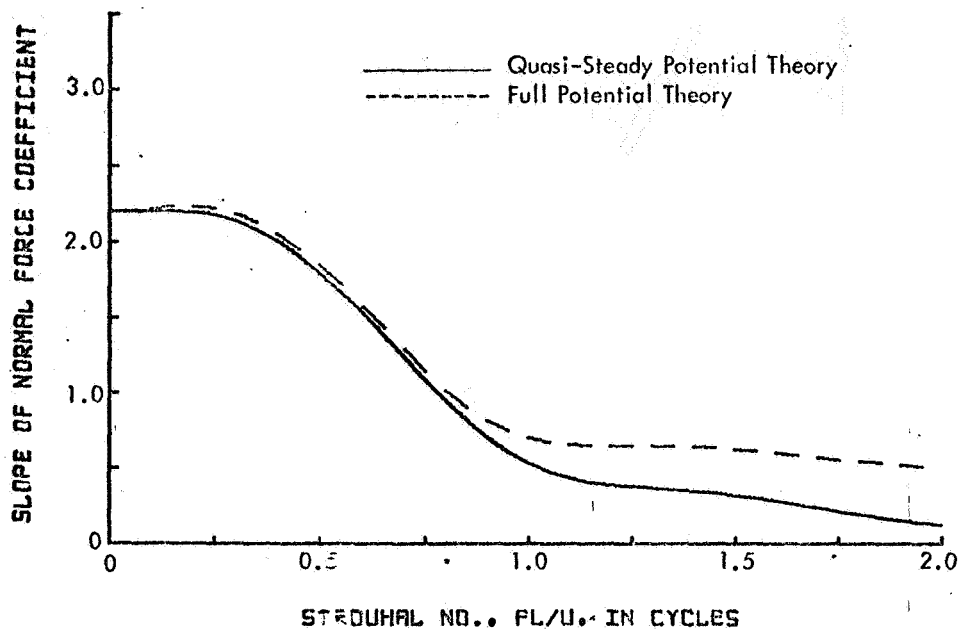


(a) Slope of Normal Force Coefficient

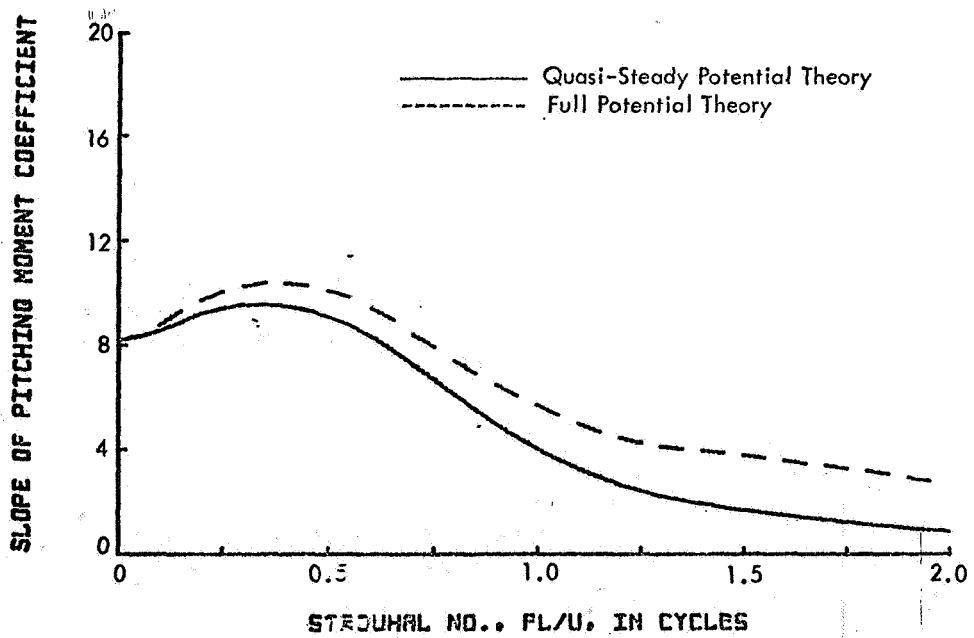


(b) Slope of Pitching Moment Coefficient

Figure 20 - Aerodynamic Frequency Responses for Various Cone-Cylinders at  $M = 2.0$  as Predicted by Quasi-Steady Potential Theory

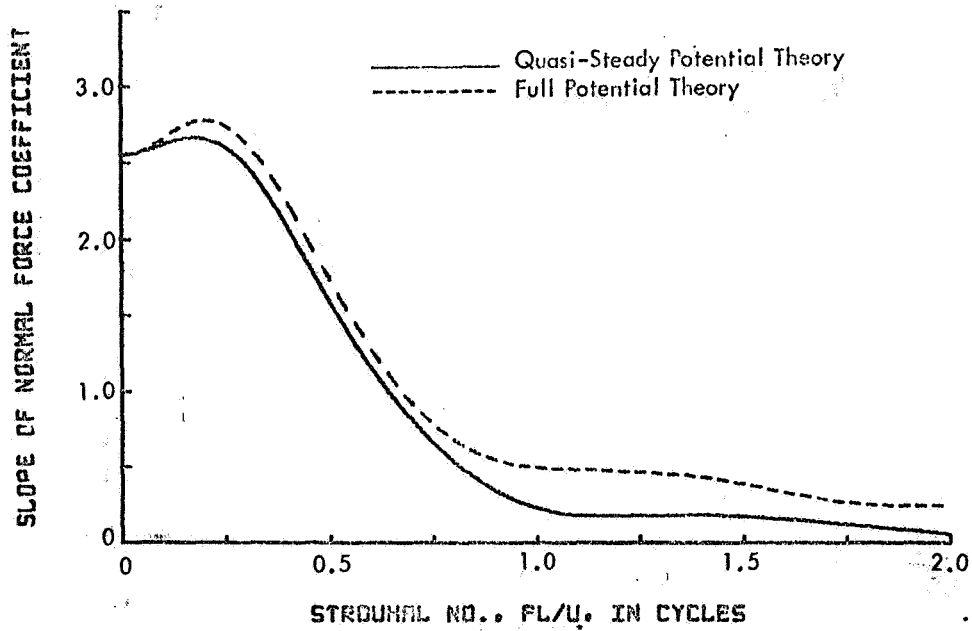


(a) Slope of Normal Force Coefficient

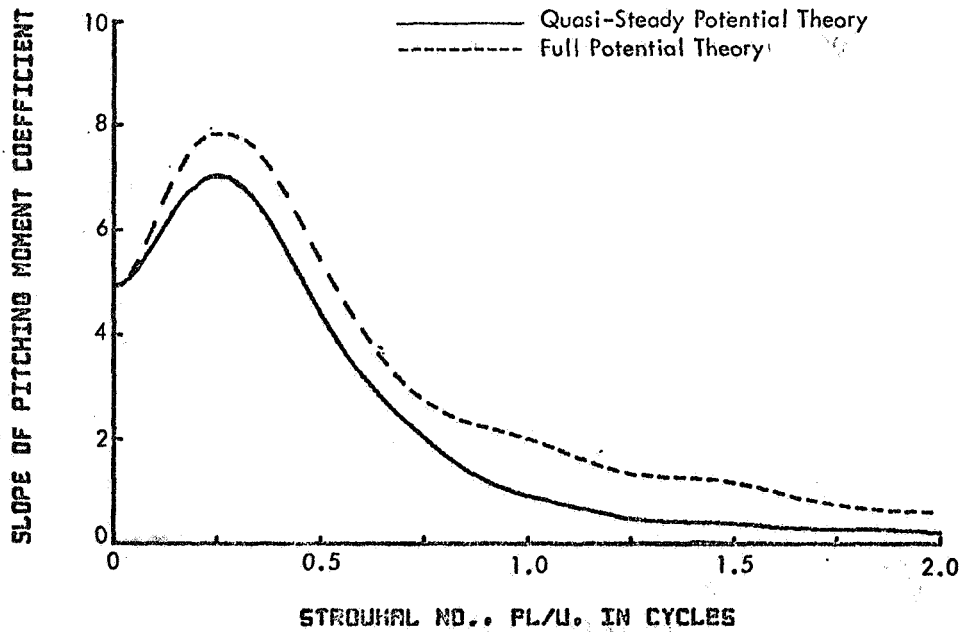


(b) Slope of Pitching Moment Coefficient

Figure 21 - Aerodynamic Frequency Responses for a 5° Cone-Cylinder at  $M = 2.0$

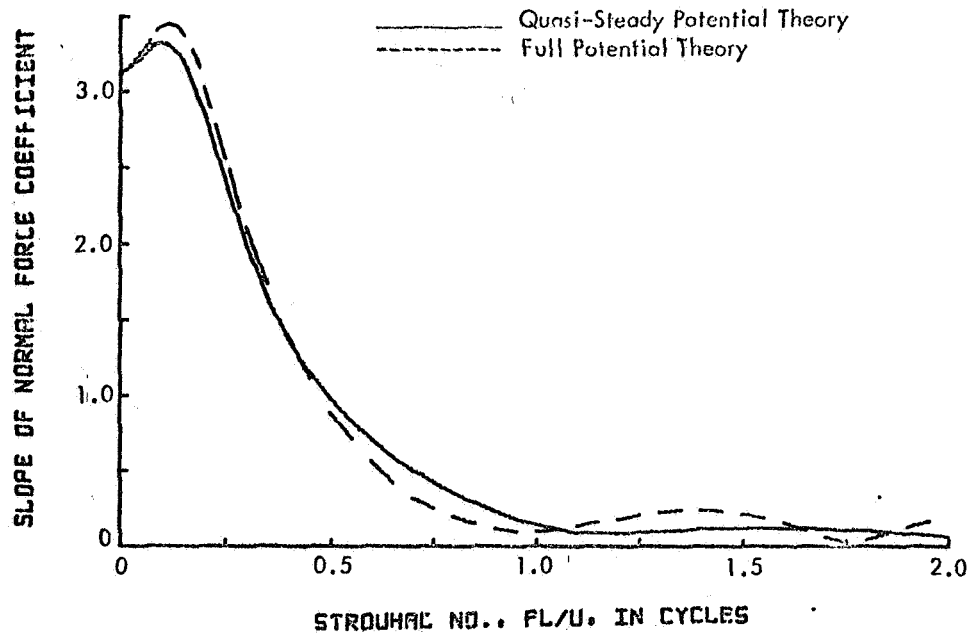


(a) Slope of Normal Force Coefficient

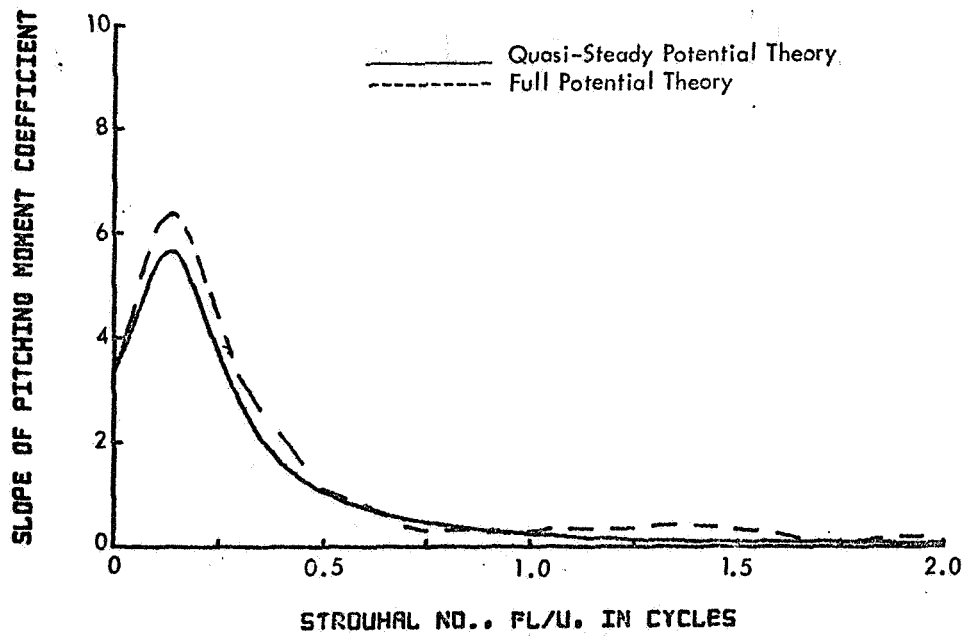


(b) Slope of Pitching Moment Coefficient

Figure 22 - Aerodynamic Frequency Responses for a  $10^\circ$  Cone-Cylinder at  $M = 2.0$

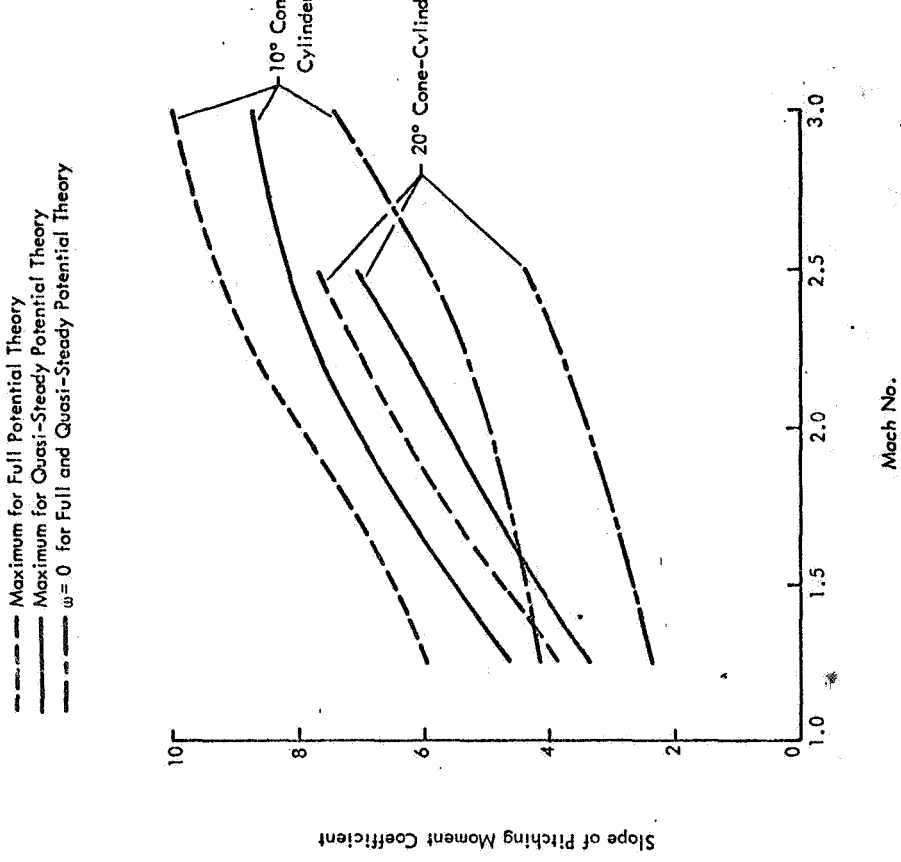


(a) Slope of Normal Force Coefficient

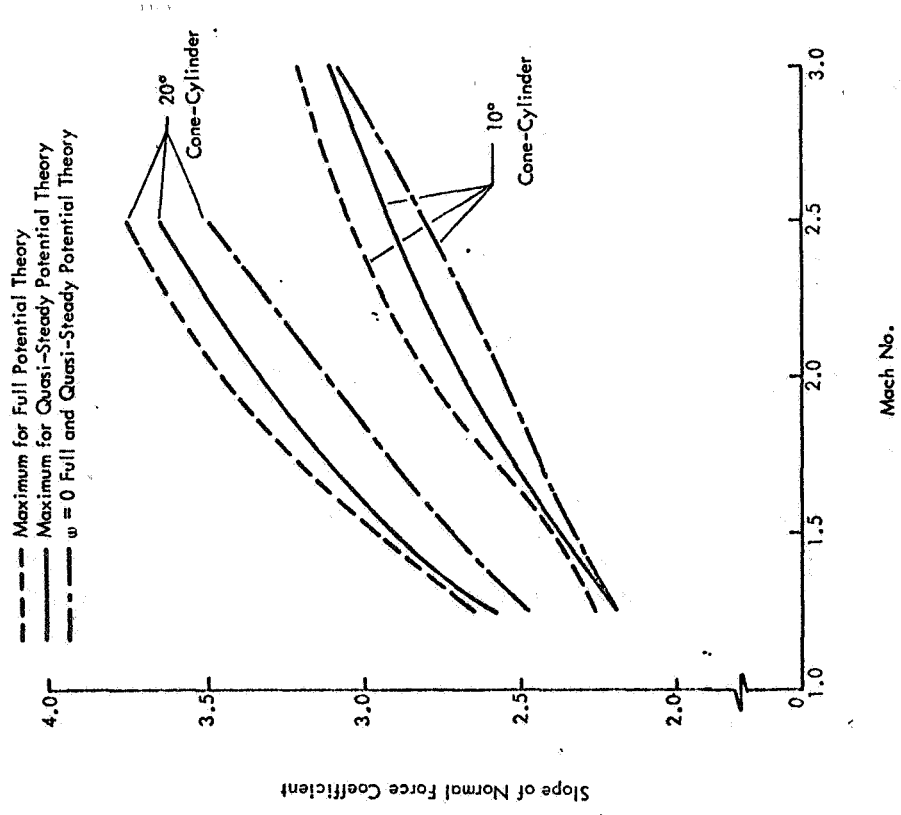


(b) Slope of Pitching Moment Coefficient

Figure 23 - Aerodynamic Frequency Responses for a  $20^\circ$  Cone-Cylinder at  $M = 2.0$



(a) Slope of Normal Force Coefficient



(b) Slope of Pitching Moment Coefficient

Figure 24 - Effects of Mach Number on Maximum Responses of 10° and 20° Cone-Cylinders

In these figures, the peak response values (irrespective of frequency) are compared with the zero-frequency (steady-state) data for the Mach number range investigated. Here it is further illustrated that the maximum  $K = 5$  responses are larger than the corresponding peak values for  $K = 3$  for both  $C_{N\alpha}$  and  $C_{M\alpha}$ . The vertical deviations of the  $K = 3$  and 5 maximum frequency response curves from the zero-frequency curves is a measure of the overshoot.

Ratios of maximum frequency response to zero-frequency response of the cone-cylinder stability derivatives were computed and the results are shown in Table V.

TABLE V

RATIOS OF MAXIMUM FREQUENCY RESPONSE TO ZERO-FREQUENCY  
RESPONSE FOR CONE CYLINDERS

Semi-Vertex Angle	Mach No.	$C_{N\alpha}$		$C_{M\alpha}$	
		<u>K = 3</u>	<u>K = 5</u>	<u>K = 3</u>	<u>K = 5</u>
5°	2.0	1.0052	1.0174	1.1697	1.2652
10°	1.25	1.0004	1.0318	1.1136	1.4361
	1.50	1.0191	1.0325	1.2652	1.4842
	1.75	1.0386	1.0669	1.3723	1.5503
	2.0	1.0489	1.0923	1.4378	1.6075
	2.5	1.0349	1.0846	1.3733	1.5707
	3.0	1.0033	1.0363	1.1748	1.3413
20°	1.25	1.0428	1.0704	1.4127	1.6425
	1.50	1.0686	1.0854	1.5768	1.7864
	1.75	1.0679	1.1076	1.6647	1.9013
	2.0	1.0722	1.1091	1.6856	1.9189
	2.5	1.0440	1.0724	1.6236	1.7572

From this table it is again seen that the maximum  $K = 5$  frequency responses are larger than the  $K = 3$  responses for both  $C_{N\alpha}$  and  $C_{M\alpha}$ . Furthermore, for each cone-cylinder, the magnitude of the resonance is a maximum, for both  $C_{N\alpha}$  and  $C_{M\alpha}$ , at (or about)  $M = 2.0$ . Also, higher resonances are noted for  $C_{N\alpha}$  than for  $C_{M\alpha}$ .

Frequency response curves of the local normal force are presented in Figure 25 for stations 1 through 4 of the 5° cone-cylinder at  $M = 2^*$ . Stations 2 and 3 bracket the maximum negative indicial potential  $dC_{N\alpha}/d(x/D)$  value. It is seen that the frequency response curve for station 1 is of type 1. The other curves shown are of type 2 with the station 2 curve showing the largest relative response at resonance. This is also the station closest to the point of maximum negative  $dC_{N\alpha}/d(x/D)$ . The frequency response curves for stations 5 through 8 are not presented since they have nearly zero magnitude.

The local frequency response results shown for the 5° cone-cylinder are indicative of the results for the other cone-cylinders. For a given station location, the maximum  $dC_{N\alpha}/d(x/D)$  value tends to increase with both Mach number and cone angle. This is especially true for the frequency response right at the shoulder.

The cone-cylinder data presented exhibit a resonance in the frequency response behavior. The presence of a maximum frequency response at nonzero impressed frequency is extremely important in that an underestimation of the aerodynamic coefficients could ensue if a low order frequency expansion theory were used to calculate cone-cylinder stability derivatives. Ogive cylinders, being similar to cone-cylinders, might also be expected to exhibit a resonance phenomena in their frequency responses. The next section shows comparisons which bear out this hypothesis.

#### E. Ogive-Cylinder Results

The numerical results for the frequency response of an ogive-cylinder are presented in this section. The body geometry is the same as that used by Platzter and Sherer<sup>26/</sup> and Bond and Packard<sup>27/</sup>:

$$R(x) = \frac{x}{3} (1 - 0.5 x) \quad 0 \leq x \leq 1$$

$$R(x) = 0.16667 \quad 1 \leq x \leq 3.3333$$

For this configuration, the fineness ratio,  $\epsilon$ , is 0.05 and the body is 10 calibers long. Frequency response calculations for the total aerodynamic characteristics were carried out over a Mach number range from 1.1 to 2.6. The pitching moment data used the body diameter as a reference length. Local normal force coefficients were evaluated for the above Mach number range at various body stations from the end of the ogive ( $x = 1$ ) to the end of the configuration.

\* See Figure 18 for the station locations.

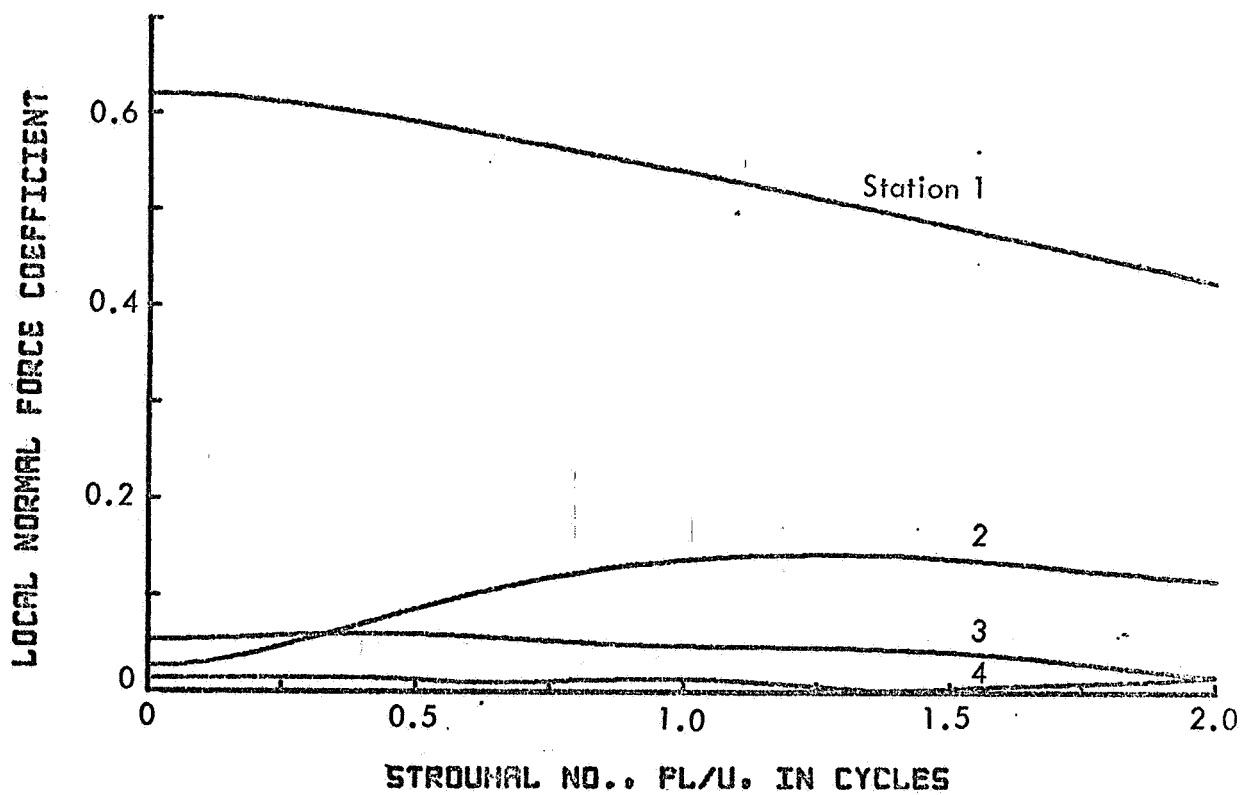


Figure 25 - Aerodynamic Frequency Responses of the Local Normal Force Coefficient at Various Station Locations for a 5° Cone-Cylinder at  $M = 2.0$



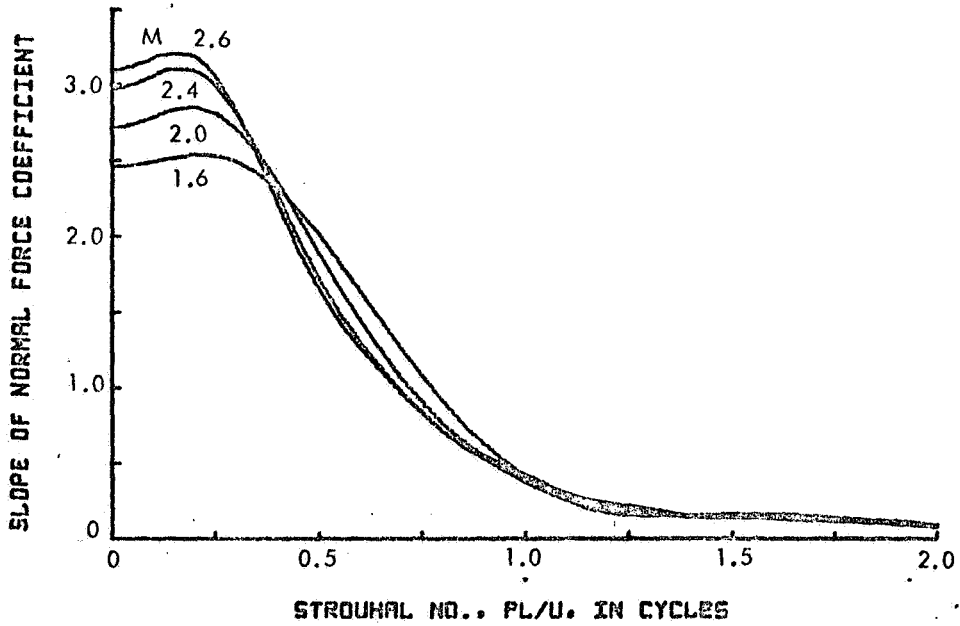
The frequency response results obtained for the  $\epsilon = 0.05$  ogive-cylinder show many similarities to those presented for the cone-cylinder configurations. That is, the frequency response of  $C_{N_\alpha}$  and  $C_{M_\alpha}$  undergo a maximum response at a nonzero impressed frequency. This is exemplified in Figures 26 through 28.

Plots of the frequency response of  $C_{N_\alpha}$  and  $C_{M_\alpha}$  are presented in Figures 26a and 26b for several Mach numbers. These results utilize the quasi-steady theory. It can be seen that the maximum response values increase while the frequency at maximum response tends to decrease with increasing Mach number, in this Mach number range. A few small resonances are also noted in the higher Mach number curves as frequency increases.

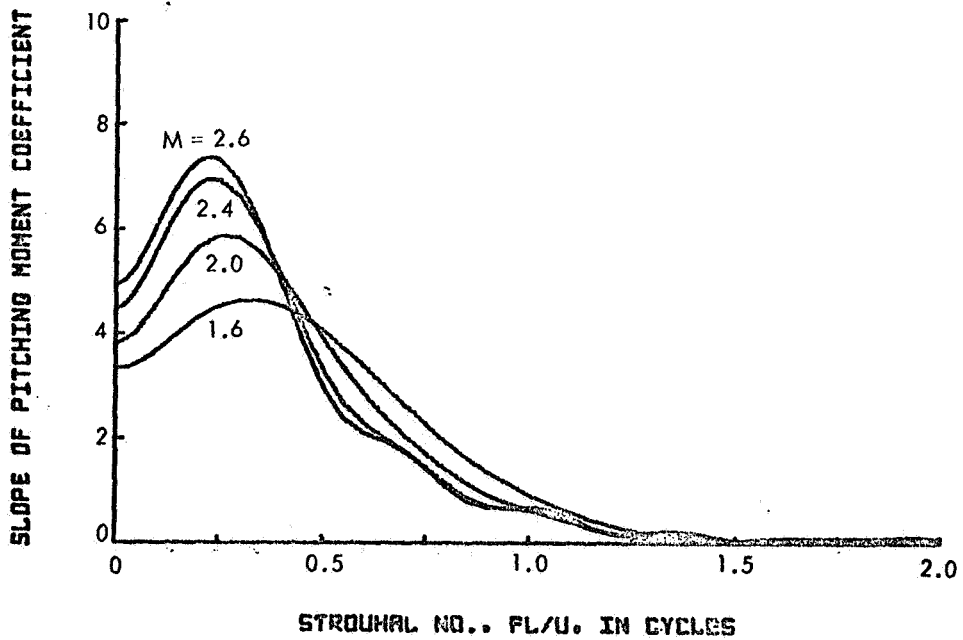
The effects of the aerodynamic representation on the frequency response of  $C_{N_\alpha}$  and  $C_{M_\alpha}$  for  $M = 1.6$  and  $2.6$  are shown in Figures 27a through 28b. In general, the full indicial theory results for both  $C_{N_\alpha}$  and  $C_{M_\alpha}$  are larger than their quasi-steady theory counterparts for the frequency range considered.

The dominant features of the ogive-cylinder  $C_{N_\alpha}$  and  $C_{M_\alpha}$  frequency response data are presented in Figures 29a and 29b. In these figures, the maximum  $C_{N_\alpha}$  and  $C_{M_\alpha}$  frequency response values are compared with the zero-frequency (steady-state) data for the Mach number range investigated. The maximum  $K = 5$  frequency response values are larger than the maximum  $K = 3$  values for both  $C_{N_\alpha}$  and  $C_{M_\alpha}$ . For  $C_{N_\alpha}$  the percentage difference is 5 percent or less over the entire Mach number range. For  $C_{M_\alpha}$  the full indicial theory predicts maximums which are 15 percent higher than those from the simpler theory for Mach numbers over 1.6. The difference increases to 30 percent at Mach numbers of 1.1 and 1.2.

Ratios of maximum frequency response to zero-frequency response of the ogive-cylinder stability derivatives are presented in Table VI. The trends evident in this table are very similar to those mentioned in the discussion of the cone-cylinder results. In particular, the maximum resonance again occurs at or near  $M = 2.0$ . It is interesting to note that the  $C_{N_\alpha}$  ( $K = 3$ ) maximum frequency response for  $M = 1.1, 1.2$  occurs at or near zero frequency (i.e., there is no resonance).

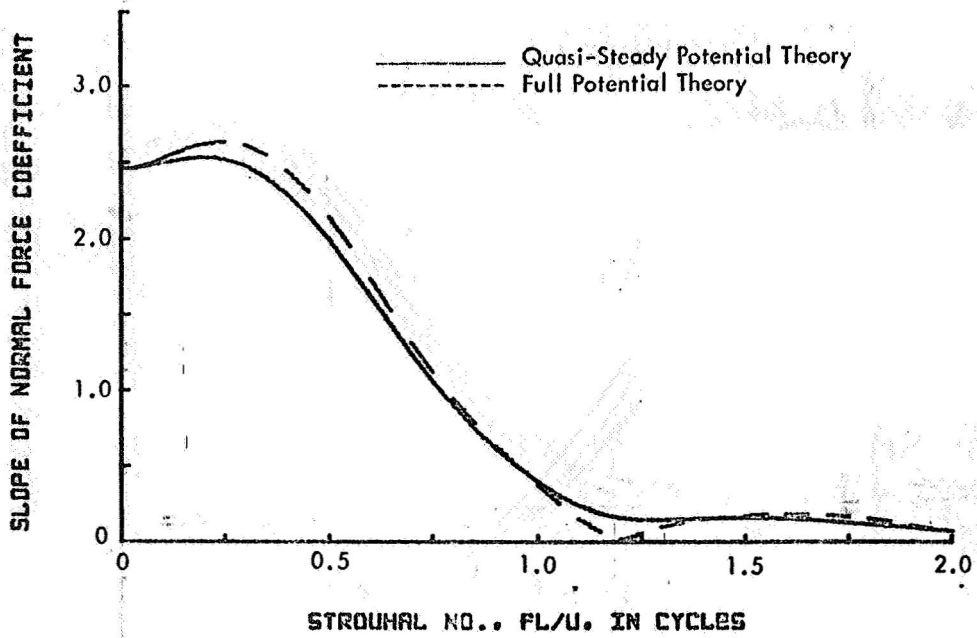


(a) Slope of Normal Force Coefficient

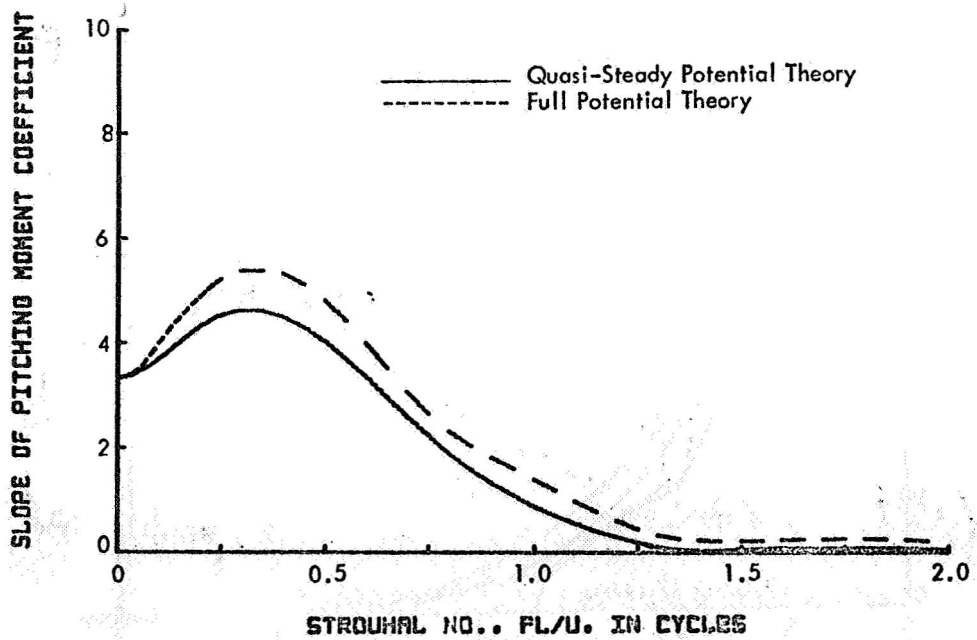


(b) Slope of Pitching Moment Coefficient

Figure 26 - Aerodynamic Frequency Responses for an  $\epsilon = 0.05$  Ogive-Cylinder at Various Mach Numbers as Predicted by Quasi-Steady Potential Theory

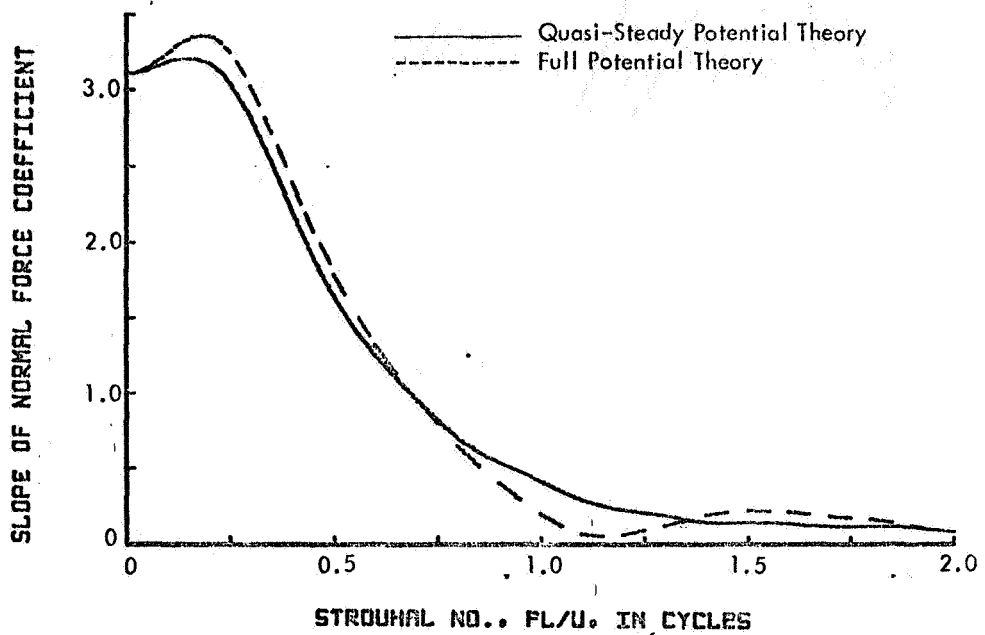


(a) Slope of Normal Force Coefficient

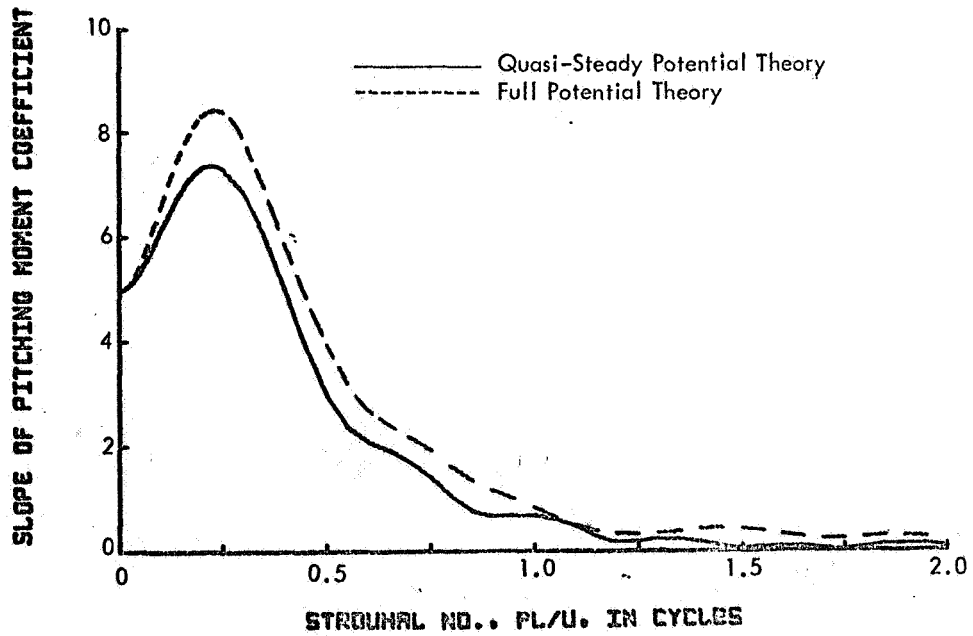


(b) Slope of Pitching Moment Coefficient

Figure 27 - Aerodynamic Frequency Responses for an  $\epsilon = 0.05$  Ogive-Cylinder at  $M = 1.6$



(a) Slope of Normal Force Coefficient

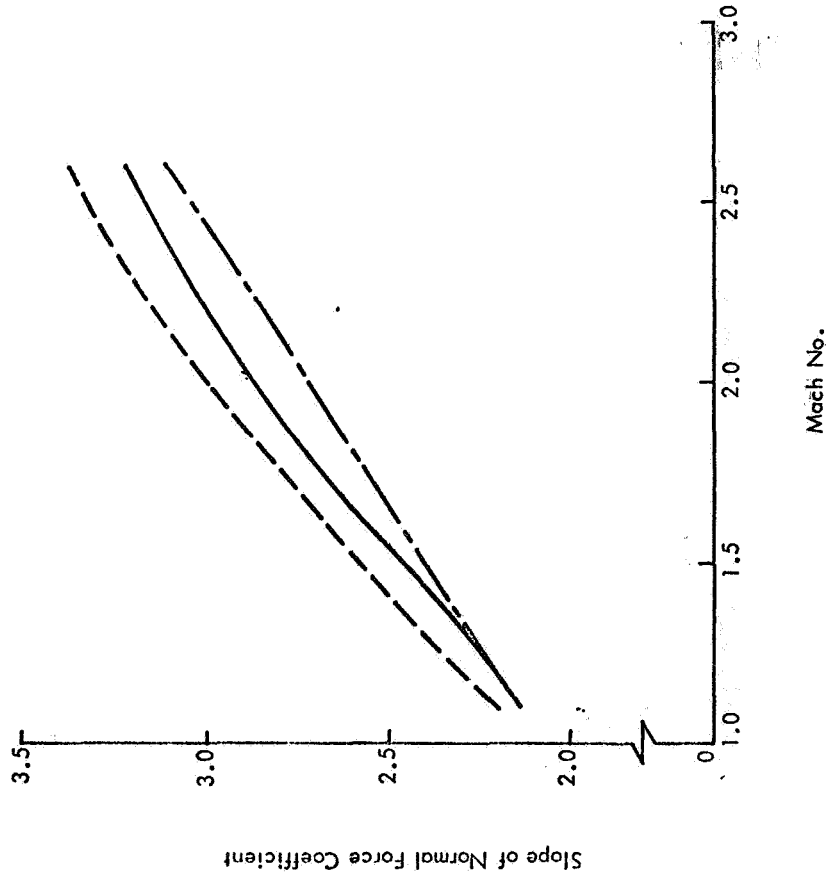


(b) Slope of Pitching Moment Coefficient

Figure 28 - Aerodynamic Frequency Responses for an  $\epsilon = 0.05$  Ogive-Cylinder at  $M = 2.6$

$\epsilon = 0.05$  Ogive-Cylinder

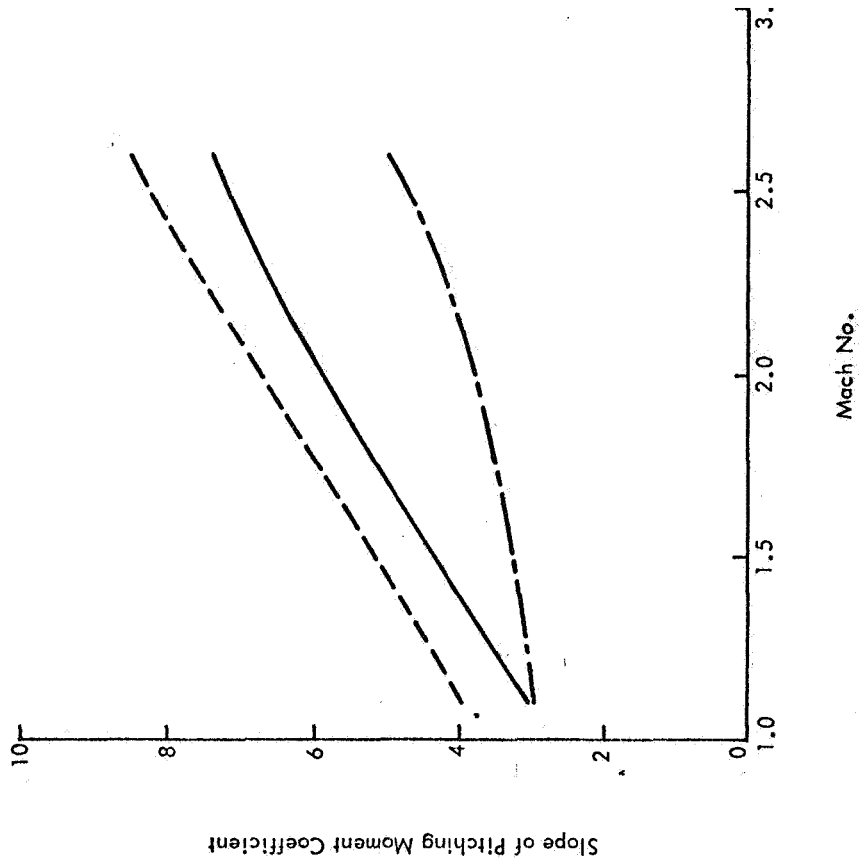
- Maximum for Full Potential Theory
- Maximum for Quasi-Steady Potential Theory
- - -  $u = 0$  Full and Quasi-Steady Potential Theory



(a) Slope of Normal Force Coefficient

$\epsilon = 0.05$  Ogive-Cylinder

- Maximum for Full Potential Theory
- Maximum for Quasi-Steady Potential Theory
- - -  $u = 0$  Full and Quasi-Steady Potential Theory



(b) Slope of Pitching Moment Coefficient

Figure 29 - Effects of Mach Number on Maximum Responses of  $\epsilon = 0.05$  Ogive-Cylinder

TABLE VI

RATIOS OF MAXIMUM FREQUENCY RESPONSE TO ZERO-FREQUENCY  
RESPONSE FOR  $\epsilon = 0.05$  OGIVE CYLINDER

Mach No.	$C_{N_\alpha}$		$C_{M_\alpha}$	
	<u>K = 3</u>	<u>K = 5</u>	<u>K = 3</u>	<u>K = 5</u>
1.1	1.0000	1.0270	1.0187	1.3174
1.2	1.0000	1.0465	1.0941	1.4251
1.6	1.0315	1.0731	1.3945	1.6237
2.0	1.0518	1.1013	1.5558	1.7701
2.4	1.0472	1.0974	1.5547	1.7778
2.6	1.0363	1.0826	1.4840	1.6978

A comparison is given in Figures 30 and 31 of the present potential (gust) theory results with oscillating body results of Bond and Packard,<sup>27/</sup> the apparent mass theory, and experiment.<sup>27/</sup> The frequency response of  $C_{M_\alpha}$  versus Strouhal number is presented in Figure 30 about an axis at the midpoint of the vehicle length ( $x_g = 0.5$ ).  $C_{M_\alpha}$  values about several axes versus Mach number at 10 Hz. are shown in Figure 31. Bond and Packard's results are based on the solution to the time-dependent linearized potential equation using linearized approximations for both the boundary conditions and pressure coefficient. The apparent mass theory is a low order, frequency-dependent slender-body theory.

The difference between the present potential theory and the other two theories (and experiments) was explained in Section III-J. Briefly, the indicial gust technique is the approach used in this investigation to compute the aerodynamic frequency responses to a prescribed sinusoidal (with axial position) cross wind. The other two theories presented (Bond and Packard and apparent mass) and the experimental results correspond to an oscillating body placed in a steady flow. The transient effects in the two cases are different. Thus, the only legitimate comparison is at zero frequency. However, the trends of the two physical situations with increasing frequency are of interest.

From Figure 30 it is seen that the trend of the present gust theory and frequency is opposite to that of the Bond and Packard and apparent mass theory. Near zero frequency, potential theory is conservative compared to the other theories and experimental results.

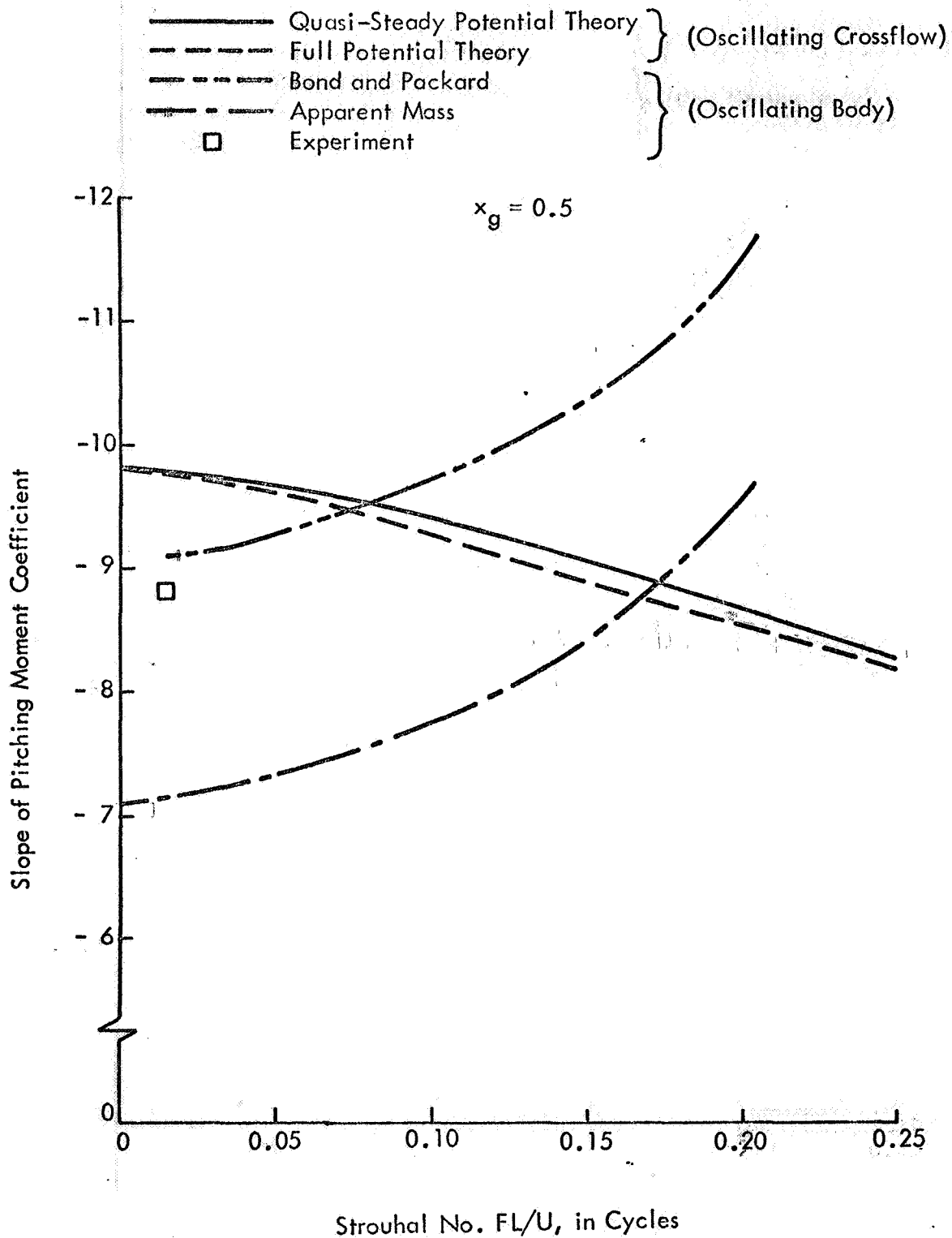
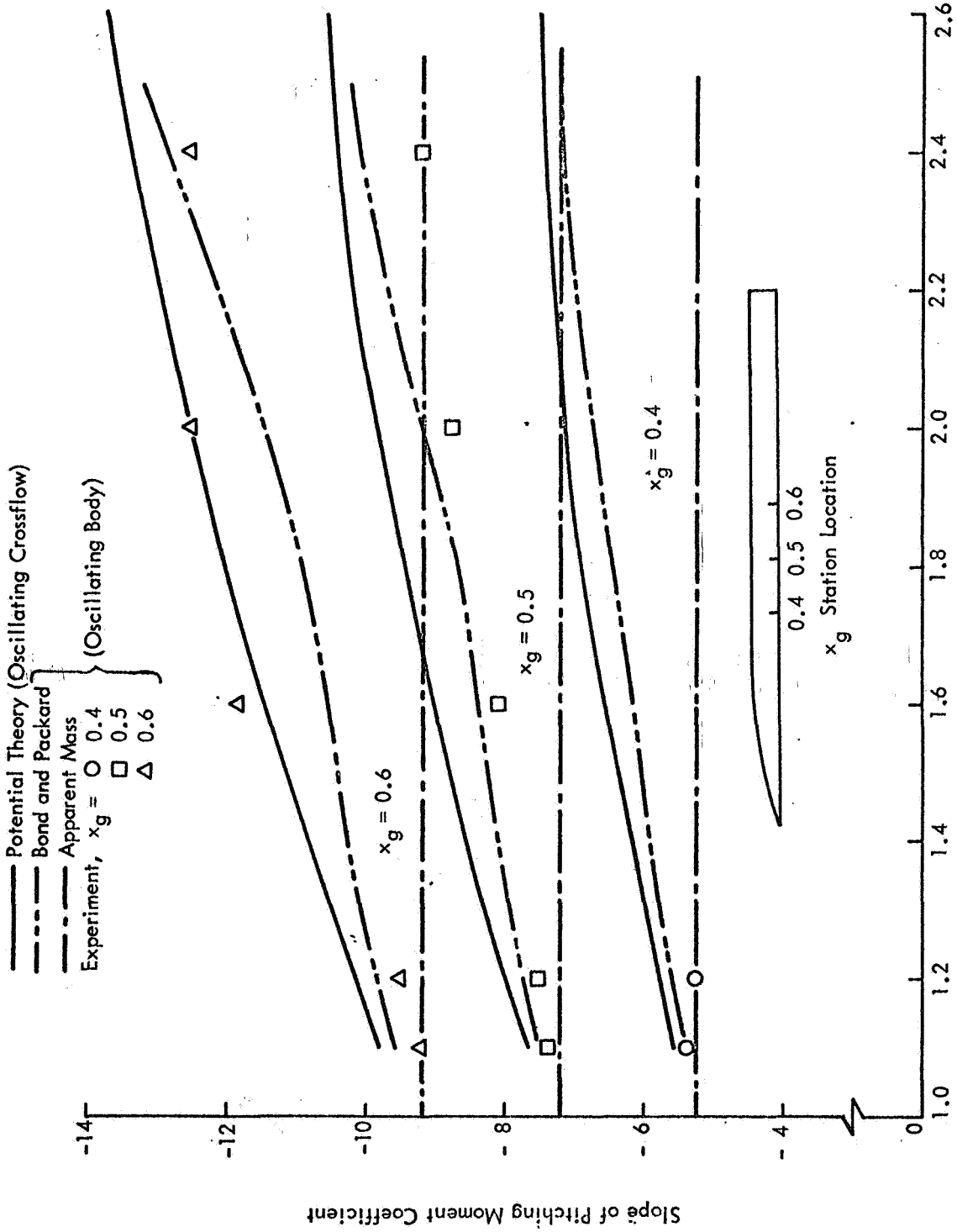


Figure 30 - Frequency Response of the Slope of the Pitching Moment Coefficient for an  $\epsilon = 0.05$  Ogive-Cylinder at  $M = 2.0$



Mach No.

Figure 31 - Slope of Pitching Moment Coefficient Versus Mach Number for  $\epsilon = 0.05$  Ogive-Cylinder and  $\omega = 10$  Hz.



From Figure 31 it is seen that for  $f = 10$  Hz. potential theory yields the same trend with Mach number as do both the experiment and Bond and Packard's results.

The results concerning the frequency response of the local normal force coefficient for ogive-cylinders are similar to those obtained for the cone-cylinders. The response curves (not presented) for  $M = 1.1, 1.2$  and  $1.6$  are of type 2 (contain a resonance) for all stations considered. For  $M = 2$  and larger, the responses at  $x = 1$  are of type 1, while the responses at the remaining stations are of type 2. For all Mach numbers considered, the maximum response value at each station decreased as distance increased downstream from the ogive-cylinder junction. For  $M \geq 1.2$  and any given station location, the maximum frequency response of  $dC_{N\alpha}/d(x/D)$  increased with Mach number.

## V. FREQUENCY RESPONSE OF AERODYNAMIC FORCES FOR SATURN V

The frequency responses for total normal force and pitching moment and the local normal forces for the Saturn V are presented in this section. The Mach number range considered was 1.3 to 1.8, while the frequencies ranged from 0 to 10 Hz for all cases, and extended to beyond 25 Hz in many instances. The corresponding Strouhal numbers,  $S = fL/U$ , ranged from about 0 to 3, or 0 to 7, respectively.\* The actual upper limit of  $S$  is Mach number dependent, since  $U$  is nearly proportional to  $M$ . See Section VI for the Mach number - density relationships used.

Figure 32 shows the local normal force distribution (at  $M = 1.3$ ) for the vehicle geometry used in this study. The vehicle geometry was that specified in MSFC drawing 10M04106, rev. M (the SA501). The local normal force over the fin-shroud region is an approximation, based on using an "equivalent" conic section for the body shape. This approximation leads to the correct total (integrated) normal force in this region. See Section III-H for additional discussion of the approximation. Also indicated in the figure are the locations of the 17 stations at which local normal force frequency responses were calculated.

The indicial normal force and pitching moment coefficients are shown in Figure 33 for a Mach number,  $M$ , of 1.3. These are the coefficients,  $C_{N\alpha}$  and  $C_{M\alpha}$ , which indicate the response to a step wind gust, and are expressed in  $\text{rad}^{-1}$ . The nondimensionalizing length used is the vehicle diameter of 10.058 meters (33 ft.). The results obtained from the full potential theory are indicated by the solid lines, whereas the simpler, quasi-steady potential theory yields the dashed curves. The time required for steady-state conditions to occur is about 0.27 sec. for the quasi-steady theory and over 1.1 sec. for the full potential theory. In the latter case, however, nearly steady conditions have been obtained after 0.41 sec. The full potential theory response, as a function of time, appears to have more higher-frequency content than the simpler theory, as evidenced by the peaks and valleys associated with the vehicle staging. The wavelengths

---

\* The integration step for calculating frequency responses is affected by the time interval used in the indicial response calculations. Assuming that five points per cycle are required to maintain acceptable accuracy, all of the results calculated to 25 Hz were not considered valid. In particular, the total responses are valid only up to  $S = 3$  for  $M = 1.5, 1.6, 1.7, 1.8$  ( $K = 3$ ) and  $M = 1.3$  ( $K = 5$ ).

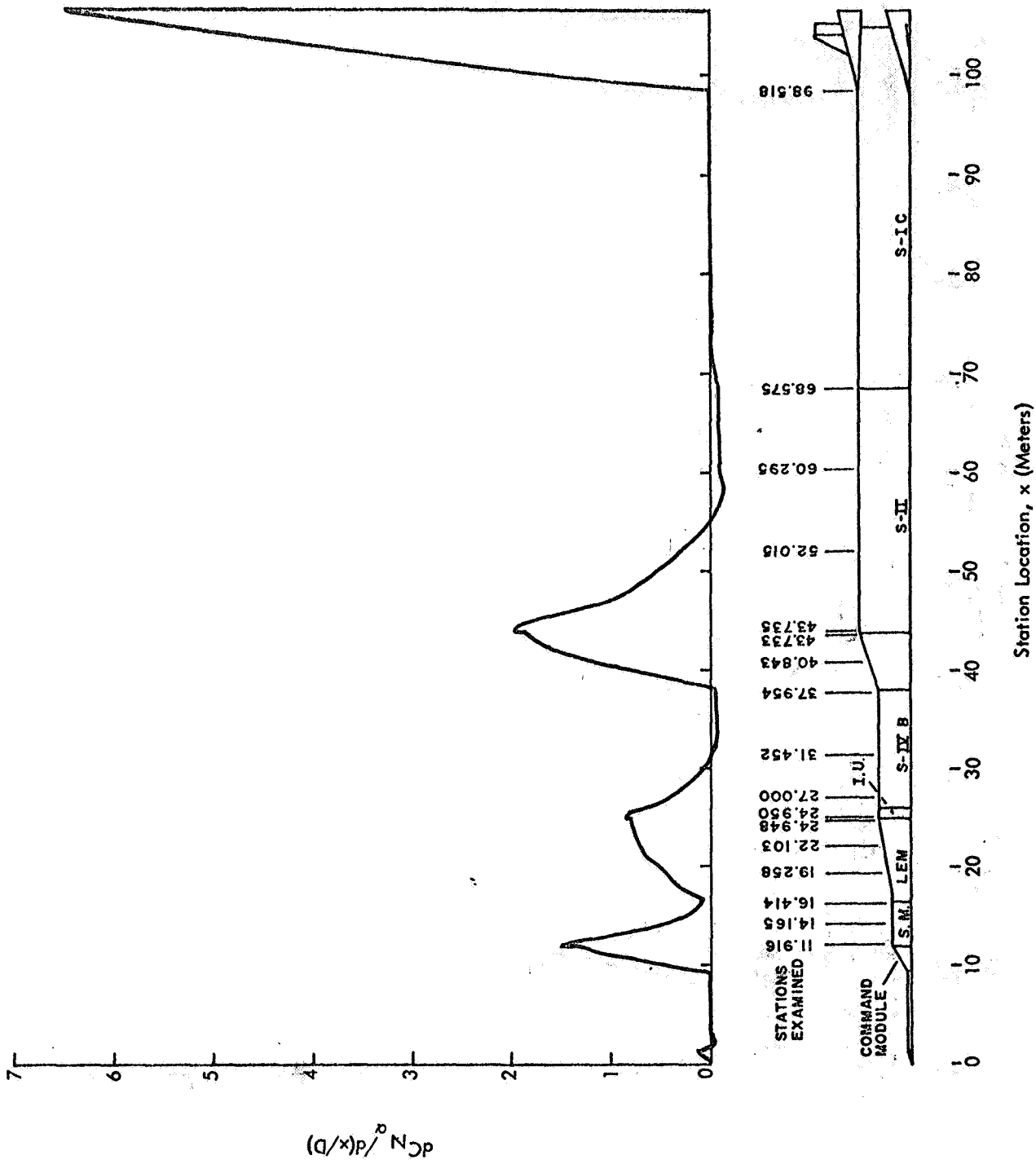
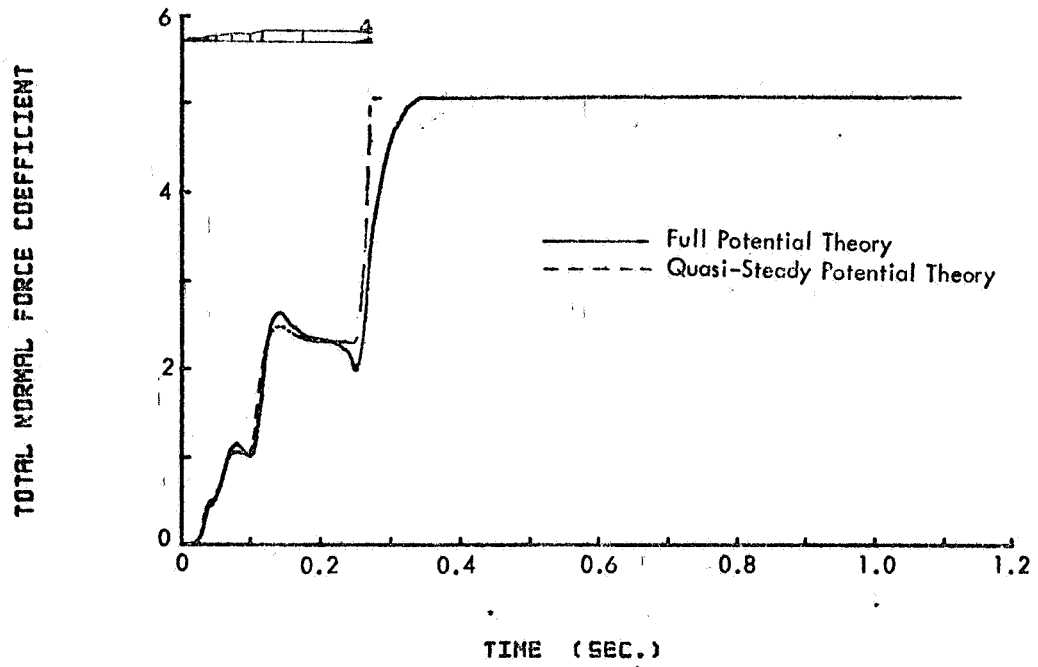
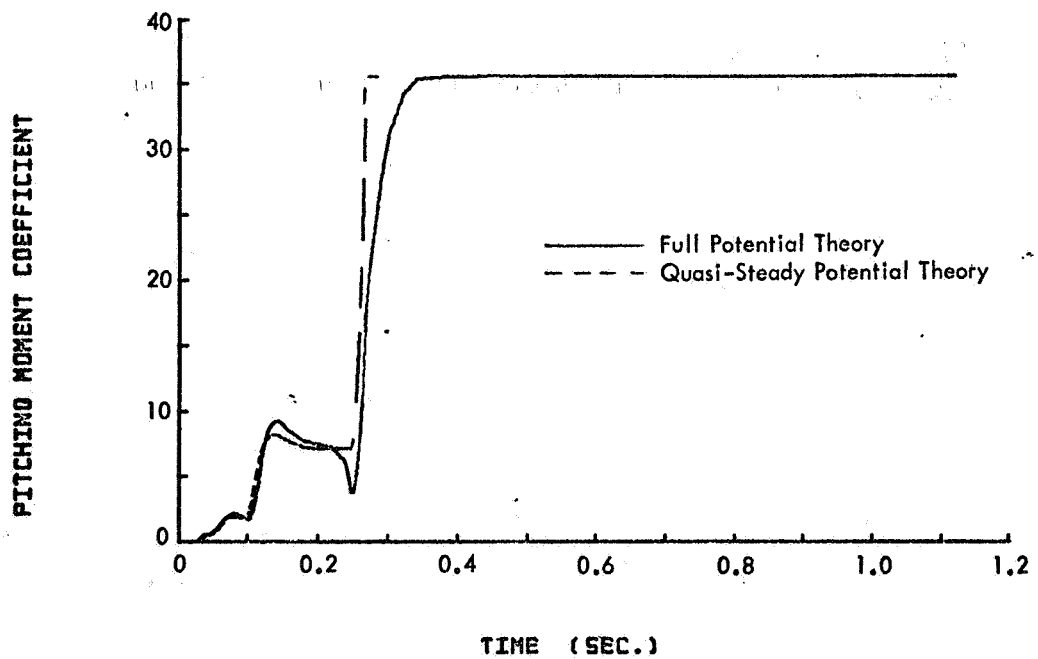


Figure 32 - Steady Local Normal Force Coefficient for Saturn V at M = 1.3



(a) Normal Force Coefficient



(b) Pitching Moment Coefficient

Figure 33 - Responses of Saturn V at  $M = 1.3$  Entering a Unit Step Gust

associated with these peaks and valleys are very short, however, when compared with the vehicle length, so they would not be expected to have much influence on the frequency response curves until the Strouhal number exceeds, say, 5.

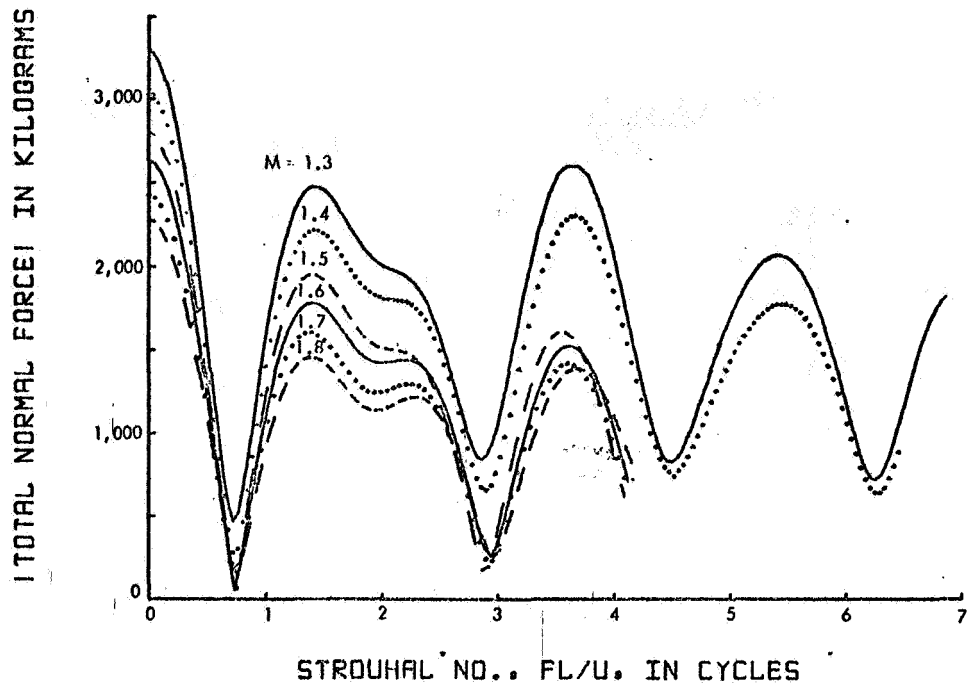
When the indicial responses, of which Figure 33 was an example, are integrated in the Duhamel sense, frequency response curves such as are shown in Figure 34 result.\* These curves were obtained from the quasi-steady theory, and clearly show several resonance frequencies which, when expressed in terms of the Strouhal number, are nearly independent of Mach number. In addition to the maximum at zero frequency, the normal force response clearly shows four resonances, with a fifth indicated at a Strouhal number of slightly over 7. The first two resonances are so close together that the peaks have overlapped. The true peaks, when separated (assuming separation to be possible) would be somewhat further apart than they appear in the figure. This may be readily shown by simply adding (either graphically or analytically) two curves (Gaussian, for instance) which overlap such that the respective peaks are relatively close together. The pitching moment results show the same resonances, at nearly the same frequencies, except that the first two peaks have coalesced into one.

It has been postulated that the staging of a launch vehicle such as the Saturn V might lead to a resonance-type of response for certain wavelengths. To examine this possibility, the resonance wavelengths indicated by Figure 34 were compared with the interstage distances. There are four conic sections which contribute to large normal forces: the command module; the Lunar Excursion Module; the interstaging between the S-IVB and the S-II; and the engine shroud region. Thus, six interstage distances can be ascertained. The aft end of each conic section was more or less arbitrarily selected for determining the interstage distances, since the local normal force is maximum there (see Figure 32). Table VII presents the results of this comparison.

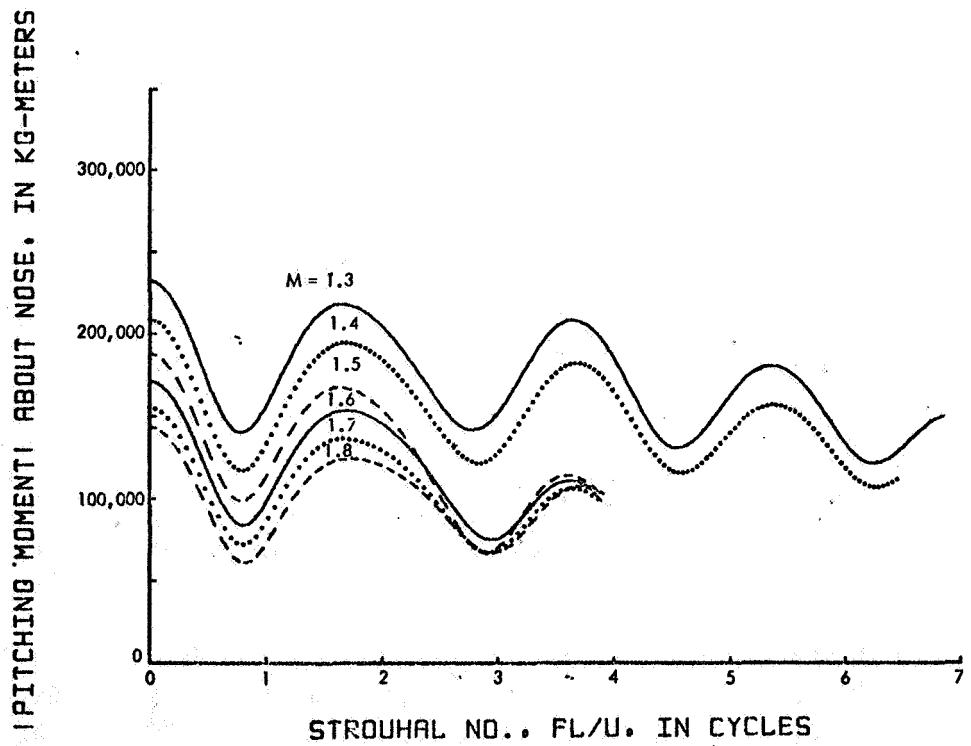
The comparison, although not conclusive, presents strong evidence that the resonances are correlated with the interstage lengths. It must be recognized in making any comparisons that each of the conic sections is of a different geometry with a different normal force distribution. Thus, one should not expect very "pure" results as concerns the frequency content.

---

\* These responses are dimensional, and correspond to a cross-wind half-amplitude of 1 meter/sec.



(a) Total Normal Force



(b) Pitching Moment

Figure 34 - Frequency Responses of Saturn V at Various Mach Numbers

TABLE VII

WAVELENGTHS OF MAXIMUM FREQUENCY RESPONSE OF TOTAL  
NORMAL FORCE FOR SATURN V

<u>Wavelength Number</u>	<u>S = fL/U (Approx.) (cycles)</u>	<u>Wavelength (Approx.) (meters)</u>	<u>Interstage Length (meters)</u>	<u>Location of Measurement</u>
1	Not Observed	Not Observed	94.6	C.M. to Shroud
2	1.3-1.4	76-82	81.6	L.E.M. to Shroud
3	2.2-2.4	44-48	62.8	S-II to Shroud
4	3.5-3.7	29-30	31.8	C.M. to S-II
5	5.4-5.5	19.4-19.7	18.8	L.E.M. to S-II
6	7.2?	14.8?	13.1	C.M. to L.E.M.

It can be rationalized that the first wavelength (94.6 meters) was not observed because (1) lift produced by the command module is very small; and/or (2) a resonance does occur but it is masked by the higher resonance at the nearby wavelength of about 82 meters (S values of 1.13 and 1.30, respectively). The poorest agreement is associated with the third wavelength (which is nearly obscured by the second in Figure 34) and the sixth wavelength (which unfortunately is not clearly defined by the available data). Nevertheless, we believe the comparison is meaningful and not due to chance. It would be of interest to modify the geometry (e.g., remove the fin and shroud conic section) to see if corresponding alterations in the frequency response were observed.

The amplitude of the resonances are, in all cases, less than the zero-frequency amplitude. Table VIII presents the ratio of peak response to zero-frequency response for the cases studied. It is seen that the so-defined relative response tends to decrease with increasing Mach number and with increasing frequency. The implication is that, although resonances do occur, the resulting aerodynamic forces are less than would be predicted by a steady flow theory. On the other hand, a frequency expansion theory would probably not show the resonances at all, so may underestimate responses at the higher frequencies.

One more point of interest in these response curves is the occurrence of the very low minimum near  $S = 0.75$ . This indicates a cancellation effect wherein the net aerodynamic responses are substantially lower than the zero-frequency responses. In particular, sinusoidal winds with a wavelength of 100-200 meters should cause negligible aerodynamic responses compared with longer wavelengths or wavelengths of around 80 meters. This is particularly true of the normal force and, to a lesser degree, of the pitching moment.

TABLE VIII

RELATIVE RESPONSE AMPLITUDES AT RESONANCE FOR SATURN V

Wavelength Number	<u>Max. Force/Force (<math>\omega = 0</math>)</u>					
	<u>M = 1.8</u>	<u>M = 1.7</u>	<u>M = 1.6</u>	<u>M = 1.5</u>	<u>M = 1.4</u>	<u>M = 1.3</u>
1	-	-	-	-	-	-
2	0.64	0.66	0.69	0.70	0.73	0.75
3	0.54	0.54	0.55	-	-	-
4	0.61*	0.59*	0.58*	0.57*	0.76	0.80
5	-	-	-	-	0.59	0.63
6	-	-	-	-	-	> 0.56

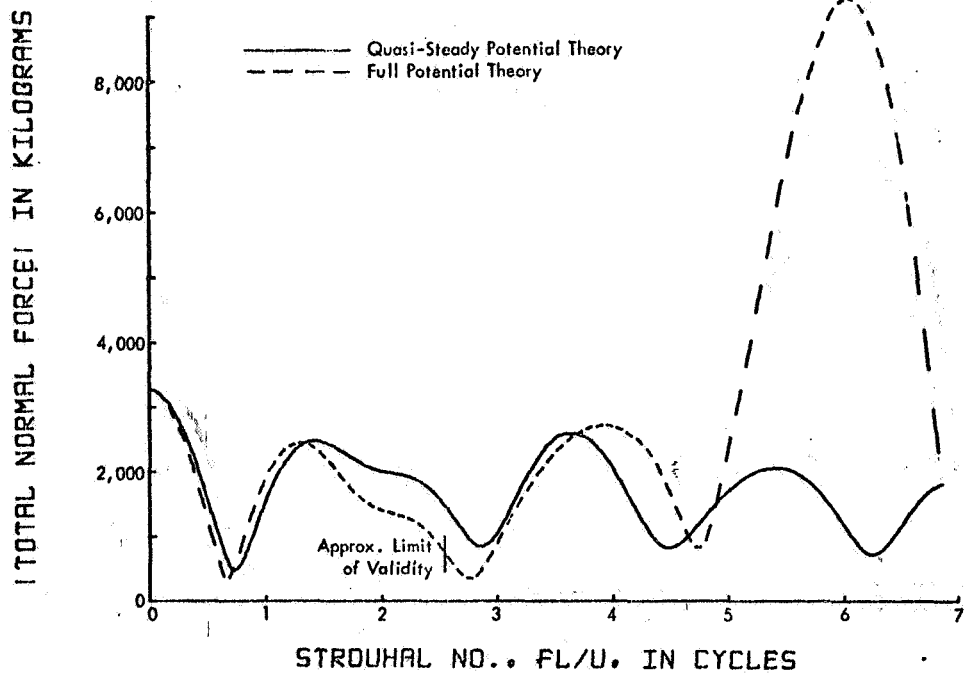
Wavelength Number	<u>Max. Moment/Moment (<math>\omega = 0</math>)</u>					
	<u>M = 1.8</u>	<u>M = 1.7</u>	<u>M = 1.6</u>	<u>M = 1.5</u>	<u>M = 1.4</u>	<u>M = 1.3</u>
1	-	-	-	-	-	-
2	0.87	0.88	0.90	0.89	0.93	0.94
3	-	-	-	-	-	-
4	0.75*	0.68*	0.65*	0.60*	0.87	0.89
5	-	-	-	-	0.75	0.78
6	-	-	-	-	-	> 0.64

\* Frequency exceeds approximate limit of validity.

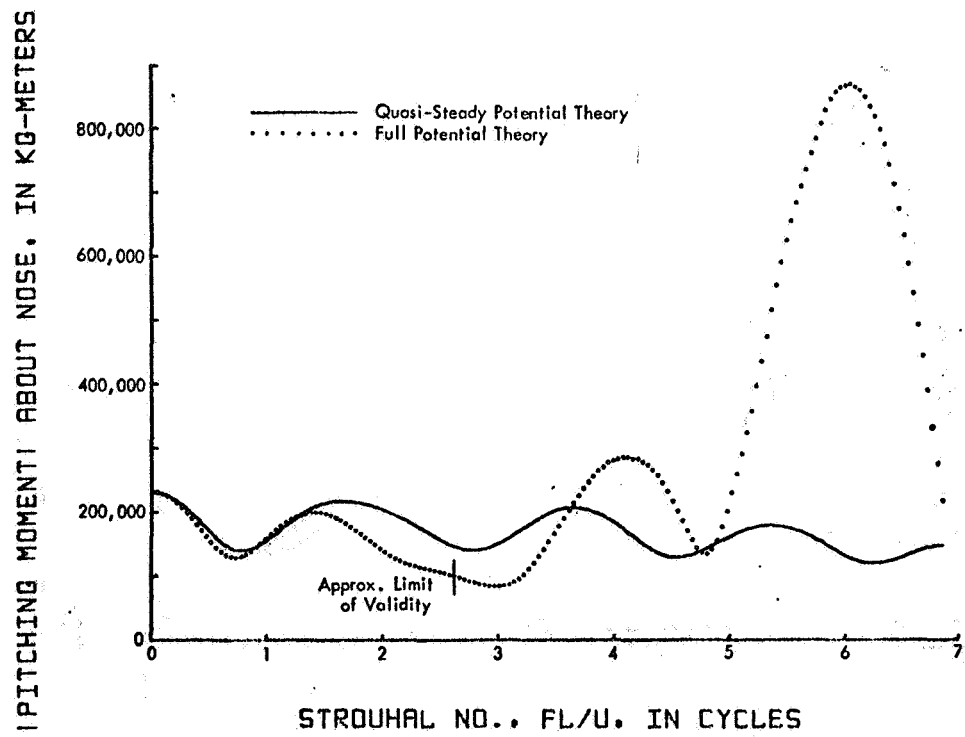
Figure 35 shows the comparison of the quasi-steady theory with the full potential theory, for a Mach number of 1.3. Within the range of validity the theories show the same general trends, although the full potential theory indicates resonance at a somewhat lower frequency.

The large peak at  $S = 6$  for the full potential theory is possibly just an indication that the numerical solution is, in fact, invalid at this high frequency. On the other hand, there may be some physical significance to this peak. There is evidence of a nearly periodic buildup of lift from the command module to the forward portion of the S-II stage (see Figure 33). During this time, two clearly defined oscillatory cycles are seen, for  $K = 5$ . This agrees nominally with the occurrence of a high frequency response at  $S \sim 6$ . A lift buildup also occurs for the quasi-steady theory but the curve lacks the distant oscillatory character associated with the overshoots and undershoots characteristic of the other theory.





(a) Total Normal Force



(b) Pitching Moment

Figure 35 - Frequency Responses of Saturn V at  $M = 1.3$  Using Two Aerodynamic Representations

Thus, many of the frequency response results for total normal forces and pitching moments can be easily related to the physical geometry and phenomena. The frequency responses of local normal forces, discussed next, are more difficult to interpret.

The frequency response of the local normal force was computed at several vehicle stations and Mach numbers for  $0 \leq f \leq 25$  Hz. The type of responses obtained are indicated by Table IX. Several trends are noted. First, a resonance condition is not apt to occur at a station on a conic section, but is likely at locations on the cylindrical portions. (See Figure 32 for station locations.) In addition, more resonances on the cylindrical portion are likely to occur at large distances downstream from a cone-cylinder junction, although they may be less important since the magnitude of the aerodynamic force (steady-state) decreases rapidly with this distance (again, see Figure 32). Finally, the number of resonances is Mach-number dependent, usually (but not always) decreasing at the higher Mach numbers.

Examples of the local normal force frequency response curves are presented in Figure 36, at  $M = 1.3$ , for six selected stations. It is interesting that the responses at 43.733 and 43.735 are so different. These stations are located either side of the cone-cylinder junction at the forward end of the S-II stage. Of course, viscous flow effects, separation, and/or shock wave effects would be expected to alter the situation, perhaps greatly. However, the basic difference in the flow, which is being slowed and compressed over the conic section and being accelerated and expanded over the cylindrical portion, must be acknowledged. It is thus not too surprising that the frequency responses are quite different.

Figures 37-39 show the Mach-number dependence of these frequency response curves for stations 43.735, 68.575, and 27.000, respectively. In the first case (Figure 37) the response is nearly independent of Mach number (except for a scale factor) for frequencies up to 10 to 15 Hz., leading to an aesthetic set of curves. However, at station 68.575 (Figure 38), the responses are not as clean. This may be explained, in part, by the fact that the steady local normal force distribution varies with Mach number. The maximum negative local normal force on the cylindrical portion is aft of station 68.575 at  $M = 1.3$  (see Figure 32) and forward of the station at  $M = 1.8$ . In any case, the resonant frequencies are not grossly affected by Mach number.

The situation is quite different at station 27.000 (Figure 39). Here the character is greatly changed by increasing Mach number, where the resonances shift upward in frequency. This phenomenon does not appear to be easily explainable, although recourse to the associated indicial response

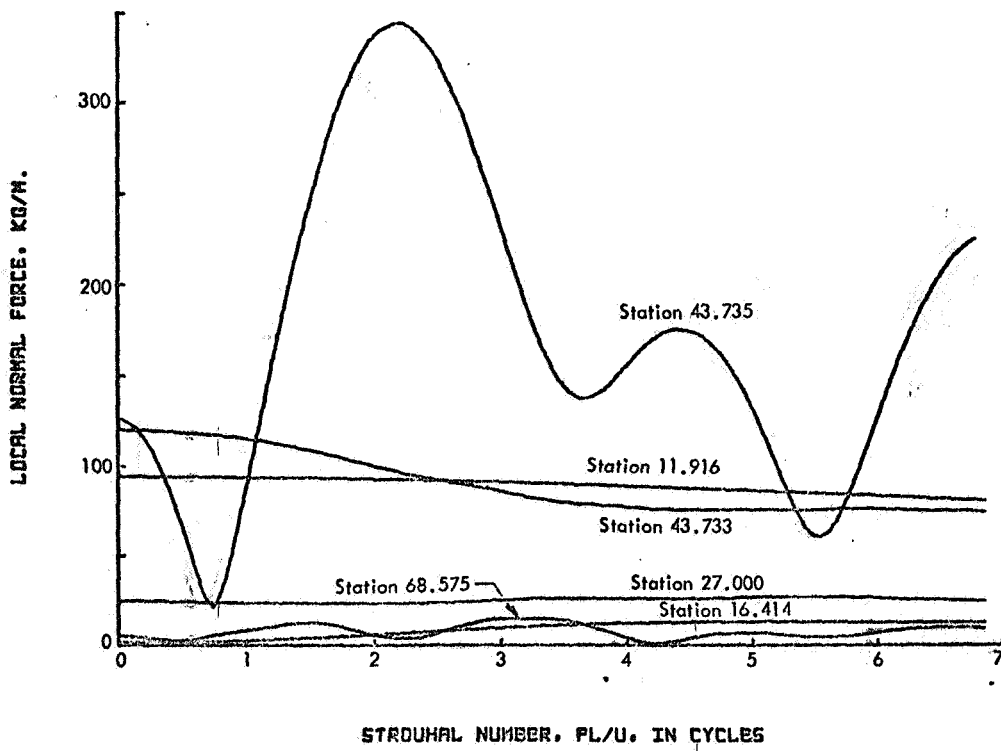


Figure 36 - Frequency Response of Local Normal Force on Saturn V at Several Stations at  $M = 1.3$  for Wind Half-Amplitude of 1 M/Sec

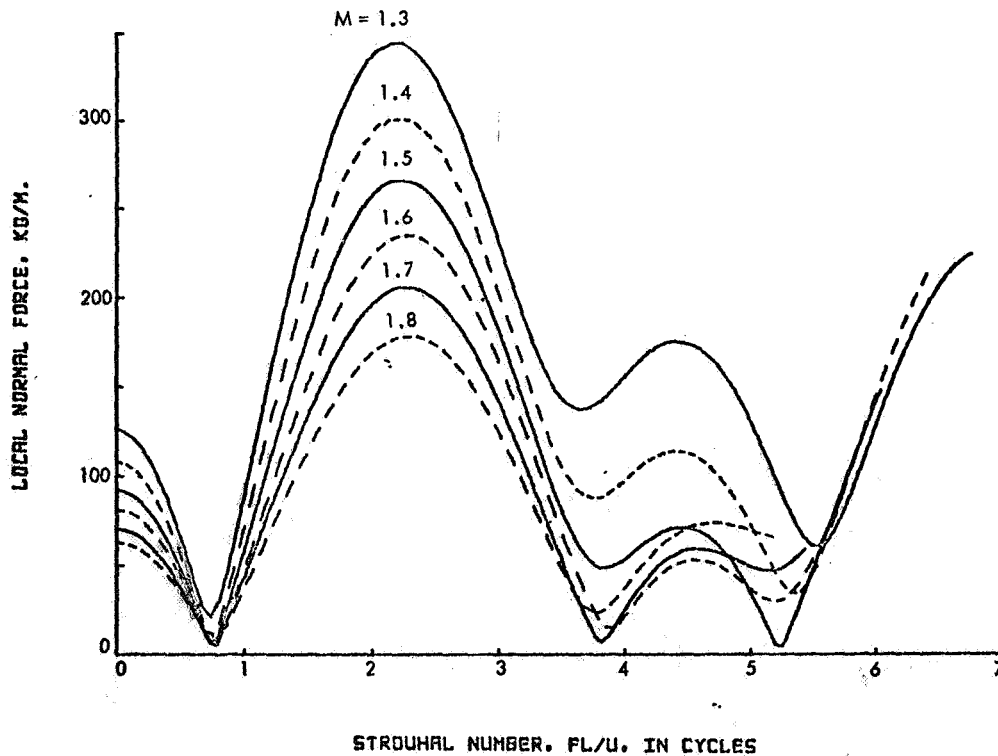


Figure 37 - Frequency Response of Local Normal Force on Saturn V at Station 43.735 Meters at Various Mach Numbers for Wind Half-Amplitude of 1 M/Sec

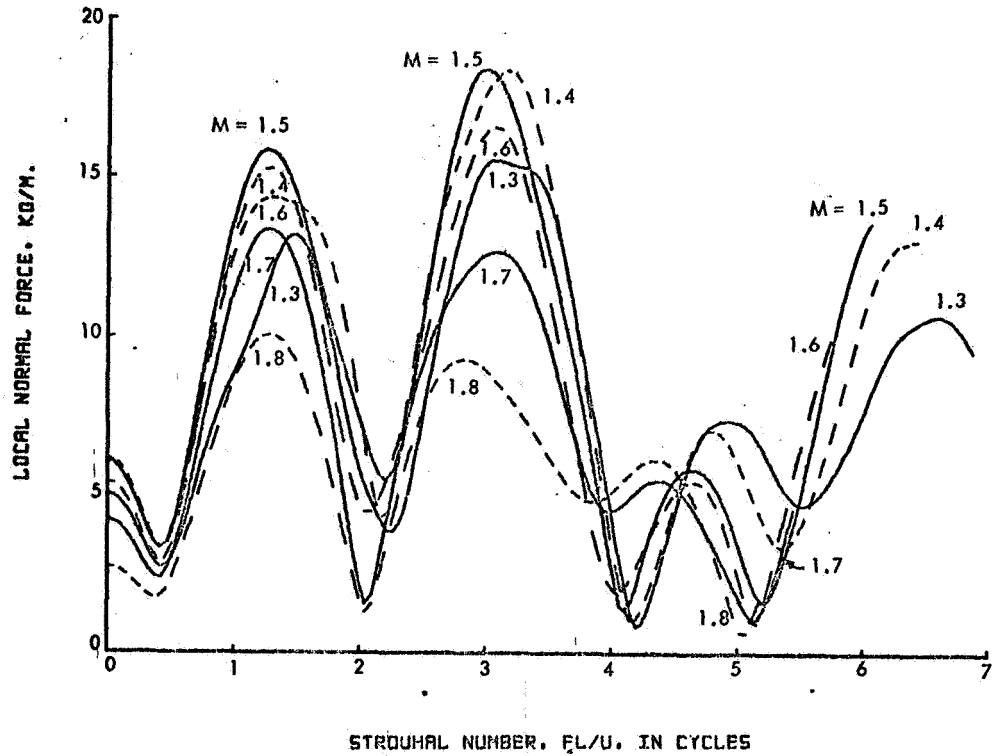


Figure 38 - Frequency Response of Local Normal Force on Saturn V at Station 68.575 Meters at Various Mach Numbers for Wind Half-Amplitude of 1 M/Sec

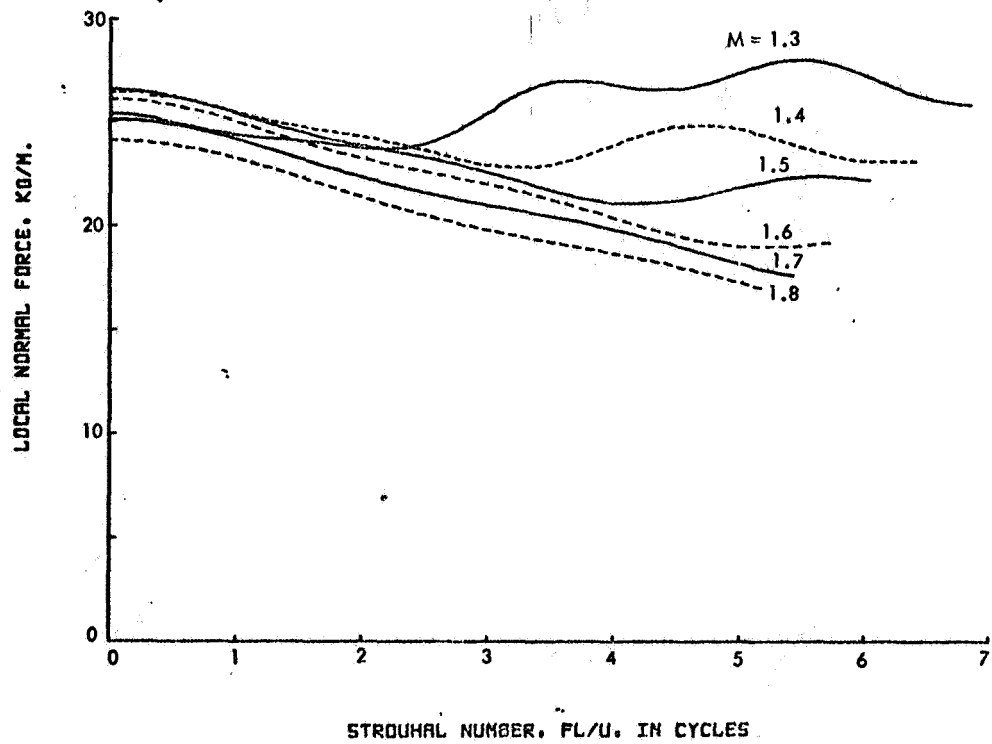


Figure 39 - Frequency Response of Local Normal Force on Saturn V at Station 27.000 Meters at Various Mach Numbers for Wind Half-Amplitude of 1 M/Sec

TABLE IX

FREQUENCY RESPONSE TYPE OF LOCAL NORMAL FORCES  
FOR SELECTED STATIONS OF SATURN V

<u>Station</u> <u>(meters)</u>	<u>Mach Number</u>					
	<u>1.3</u>	<u>1.4</u>	<u>1.5</u>	<u>1.6</u>	<u>1.7</u>	<u>1.8</u>
11.916	1	1	1	1	1	1
14.165	2(1)	2(1)				
16.414	2(2)	2(1)				
19.258	1	1				
22.103	1	1	1	1	1	1
24.948	1	1				
24.950	1	1	1	1	1	1
27.000	2(2)	2(2)	2(1)	2(1)	1	1
31.452	2(3)	2(2)				
37.354	2(5)	2(4)				
40.843	1	2(1)	2(2)	2(2)	2(1)	2(1)
43.733	2(2)	2(1)				
43.735	2(3)	2(3)	2(3)	2(3)	2(3)	2(2)
50.015	2(3)	2(3)	2(3)	2(3)	2(3)	2(3)
60.295	2(4)	2(4)				
68.575	2(4)	2(4)	2(4)	2(4)	2(4)	2(4)
98.518	2(many)	2(many)				

NOTE: Type 1 has no resonance for  $f < 25$  Hz.

Type 2 has one or more resonances for  $f < 25$  Hz. The number of such resonances is indicated in parentheses, and may include a resonance indicated by an increasing response at 25 Hz., although peak occurs for  $f > 25$  Hz.

does clarify the situation somewhat. Figure 40 shows the growth of lift at this station for the two extremes of the Mach number range considered. (The transition with Mach number is continuous.) The curves have been offset for clarity. The oscillatory character at the lower speed is clearly apparent, as compared to the Mach 1.8 curve which tends to have a "damped" character.

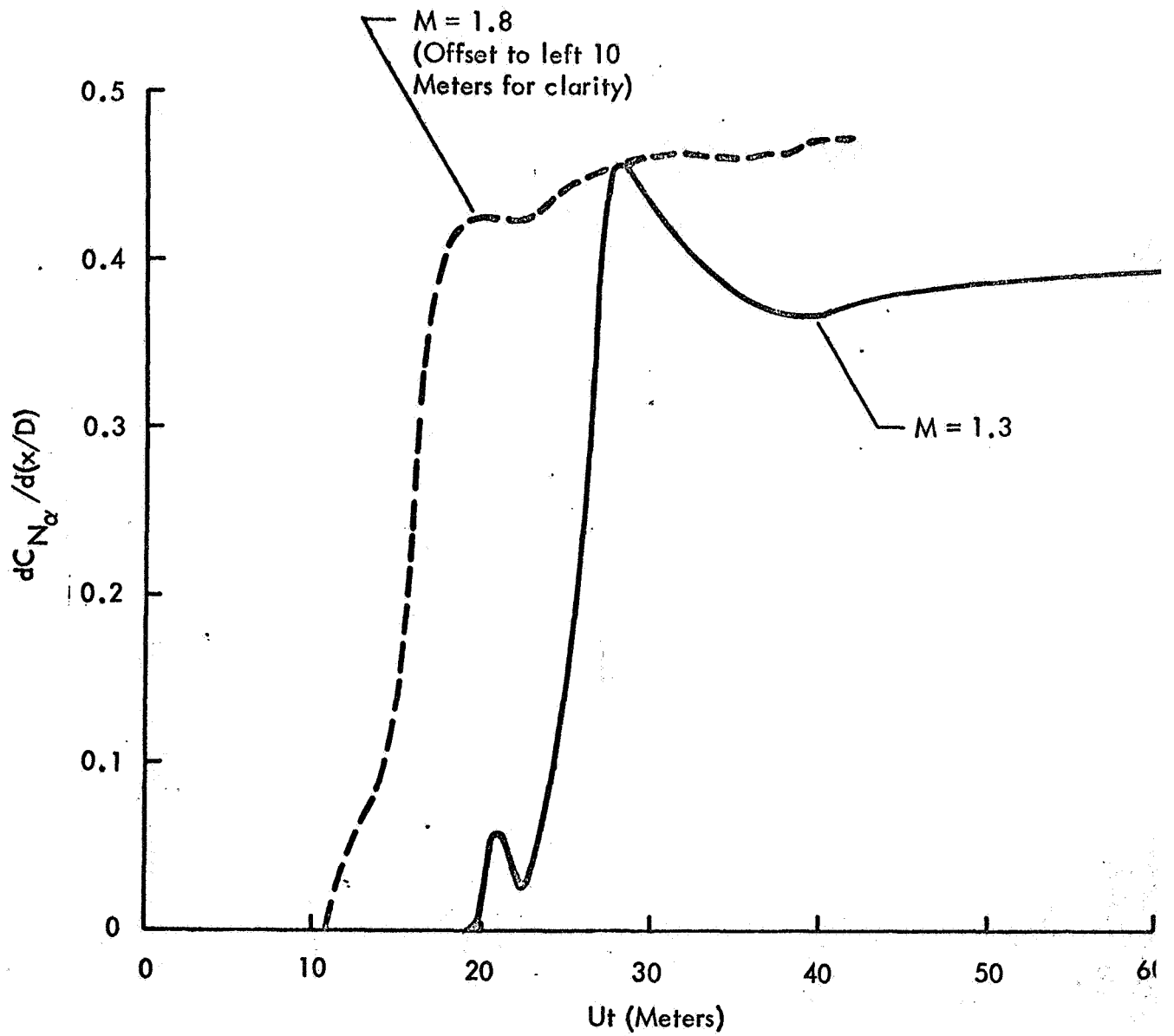


Figure 40 - Growth of Lift at Station 27.000 Meters of Saturn V at Different Mach Numbers

VI. RESPONSE OF AERODYNAMIC FORCES ON SATURN V  
TO INFLIGHT WINDS

In this section, we present and discuss the aerodynamic forces on the Saturn V vehicle which arise from penetration of horizontal winds. First, however, the winds and the vehicle trajectory are discussed.

The wind data were taken from the data of Scoggins et al.<sup>16/</sup> These data were obtained by observing the rise of a special balloon by radar (the FPS-16 Radar/Jimsphere technique). The data, after reduction, are given as winds at 25-meter altitude increments. For this study the "scalar winds" were used. That is, the magnitude of the horizontal wind, independent of direction, was selected for input data to the present wind integration routine.

The following wind profiles were initially selected for analysis, and placed on punched cards: test numbers 0734, 1999, 2378, 2652-1, 2579, and 2936. After initial running of the computer program, it was decided to limit the full analysis to two of the winds: 2652-1 and 2579. These winds had high frequency components and large shears. Typical results are presented in this report for the winds of test number 2652-1.

Since the winds are given as a function of altitude, it is necessary to relate the vehicle speed, etc., to altitude. For this purpose, the nominal trajectory of vehicle AS504 was used.<sup>28/</sup> The key data from this are given in Table X.

TABLE X

SATURN V NOMINAL TRAJECTORY DATA

<u>Flight Time</u> <u>(sec.)</u>	<u>Altitude</u> <u>(km.)</u>	<u>Mach No.</u>	<u>Velocity</u> <u>(m/sec)</u>	<u>Dynamic Pressure</u> <u>(kg/m<sup>2</sup>)</u>
72.	9.0408	1.140	354.471	3013.17
74.992	10.0000	1.254	383.947	3175.69
80.	11.7316	1.472	438.140	3370.53
84.	13.2299	1.667	486.112	3413.45
85.955	14.0000	1.767	511.134	3387.47
88.	14.8325	1.875	538.434	3323.71
96.	18.3533	2.281	656.597	2733.29

Quadratic interpolation was used to obtain information between tabulated values. Furthermore it was assumed, for this study, that the winds were normal to the vehicle axis; this would be true only if the vehicle were flying vertically, which is not the case. Since our purpose was merely to test the computer program and gain insight into basic phenomena which might exist, there was nothing to be gained by unduly complicating the picture by correcting the winds for vehicle trajectory angle.

Appendix II contains a description of the method used to compute wind shears from the wind data.

Figure 41 shows the total aerodynamic forces in response to the winds in a normalized form, which must be clarified. First of all, the measured scalar wind velocity at the 25-meter increments are indicated by the plotted points. The responses followed the trends of the wind, so a normalized scheme was employed to enable better comparison of results. Each response value was divided by the steady-state response of the same quantity (e.g., force, moment, etc.) to a 1 m/sec wind. Thus, if the vehicle responded to the wind instantly with a steady-state response (e.g., the so-called instantaneous immersion case), the normalized response would exactly duplicate the wind data.

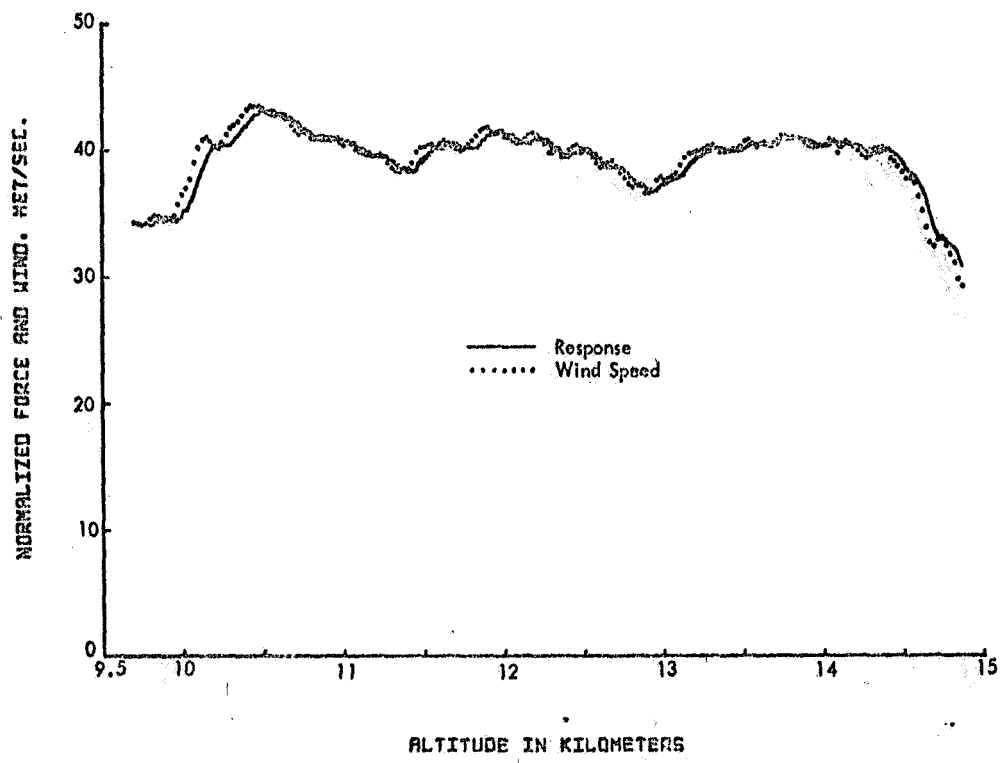
The Mach number range shown is from 1.3 to 1.8. For each Mach number considered (1.3, 1.4, 1.5, 1.6, 1.7 and 1.8) responses were computed over an altitude range corresponding roughly to a Mach number change of over 0.25, insuring a complete overlap of computed data. After normalizing each response by the associated steady-state response, no Mach number dependence remained which could be detected at this scale.

The responses display two important features which are indicative of the unsteady aerodynamics employed.\* First, an obvious time lag (or altitude lag as the results are plotted) exists between the wind and the response. The magnitude of this delay is about 100 meters, the length of the vehicle. Secondly, the "high frequency" components of the wind have been filtered out. In particular, the portion of the wind at 13.5 km., which has a major wavelength of about 240 meters and an additional component at about 120 meters is of interest. The response contains a subdued portion of the 240-meter wavelength but little evidence of the 120-meter wavelength. These results are in agreement with predictions based on the frequency response data of Figure 34. Also, a single cycle of the wind occurs at about 10.2 km. and again at 14.7 km. The normal force response contains no oscillation at these altitudes, whereas the pitching moment contains a small oscillation.

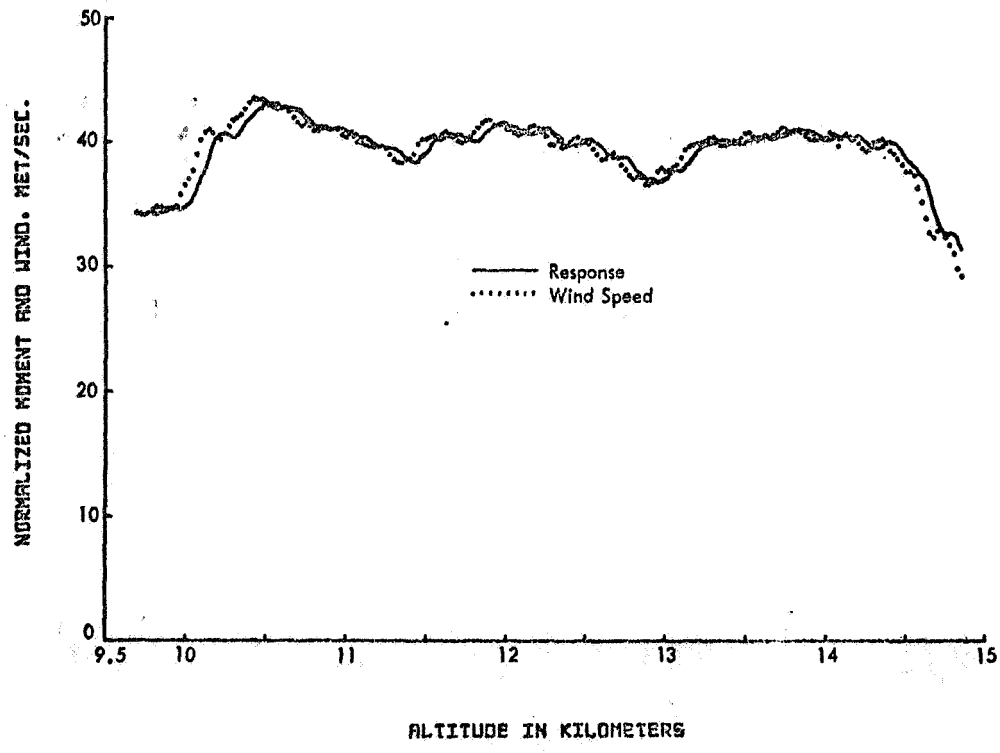
---

\* The quasi-steady theory was used here. No noticeable difference was detected utilizing the full potential theory.





(a) Total Normal Force



(b) Pitching Moment

Figure 41 - Normalized Responses of Saturn V to a Measured Wind Profile

The aerodynamic responses are affected not only by the wind magnitude but also, to a small degree, by the wind shear. To demonstrate this it is necessary to remove from the response the effect of the wind and the time lag associated with penetration; then the remaining portion of the response is examined.

Figure 42 illustrates this wind shear effect for a short altitude interval at station 43.735. The local normal force is shown as a function of altitude, but is normalized by dividing by the steady state response to a unit wind and by the local wind magnitude. The local wind magnitude, to account for the penetration lag, is taken at the altitude of the station in question -- in this case at 43.735 meters below the altitude of the nose of the vehicle. Thus, except for aerodynamic inertia effects, the normalized response should be identically equal to 1. Also shown in this figure is the wind shear at the station in question. The effect of wind shear on the response is thus seen to be obvious, regardless of Mach number, even though the magnitude of the effect is generally less than 0.5 percent.

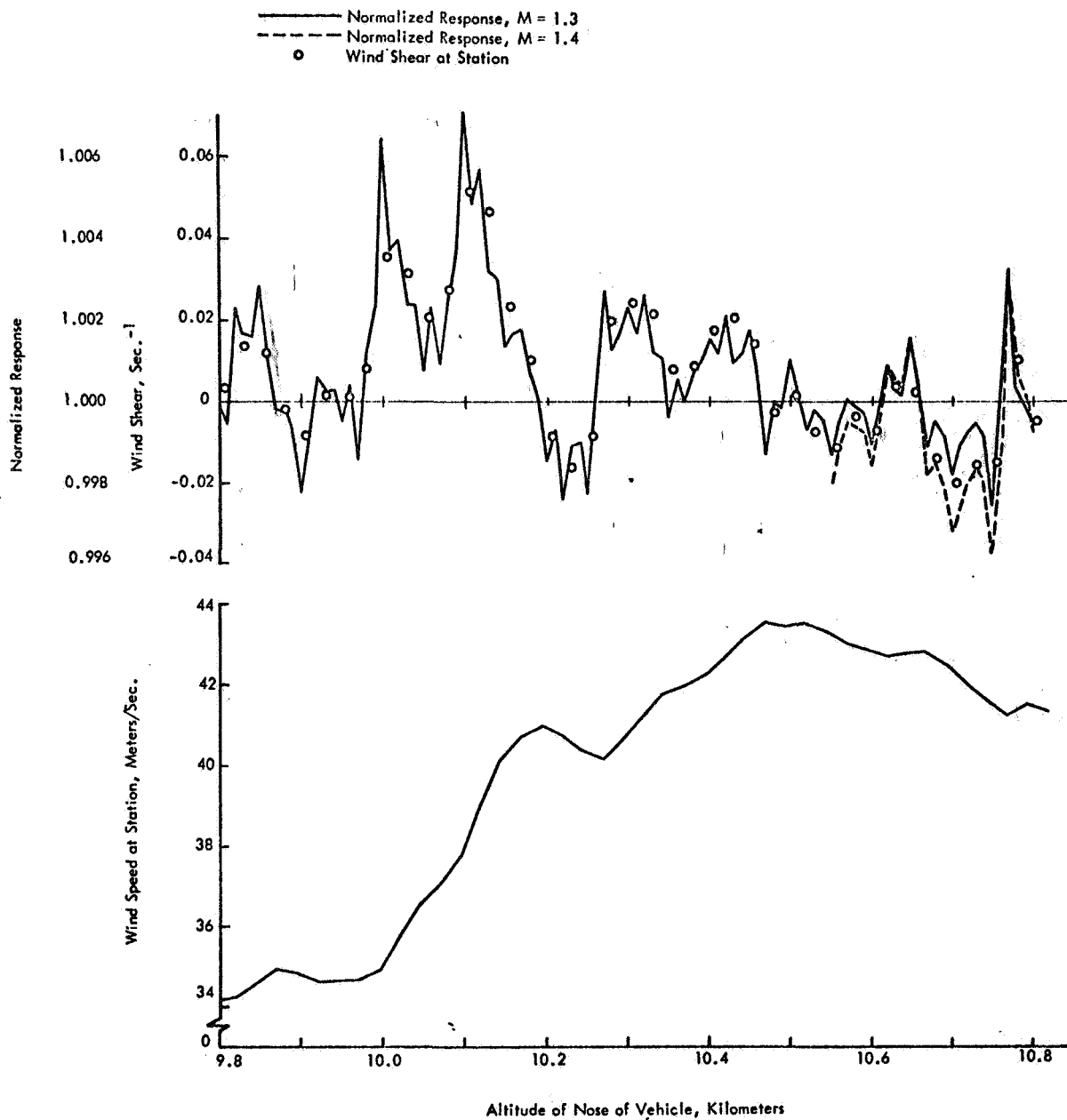


Figure 42 - Effect of Wind Shear and Aerodynamic Inertia  
on Local Normal Force at Station  
43.735 Meters of Saturn V

## APPENDIX I

### COMPARISON OF AERODYNAMIC FREQUENCY RESPONSE BEHAVIOR WITH A SIMPLE SPRING-MASS ANALOGY

An analysis of the frequency response data was undertaken to gain insight into complex behavior of the aerodynamic frequency responses. The results of this study are presented in this Appendix. The investigation of the sinusoidal response data is directed toward comparing these data to the results obtained from the indicial and frequency response of a simple spring-mass analogy. The simple analogy is tested to determine if the salient features of the indicial responses (maximum response and location of maximum response) can be used to predict the dominant features of the aerodynamic frequency response data.

Consider a simple one degree of freedom spring-mass-damper system (see Figure 43) being driven by an external force  $F(t)$ . The equation of motion of such a mechanical system with viscous damping is

$$m\ddot{x} + c\dot{x} + kx = F(t) \quad (I-1)$$

where  $m$  is the mass,  $c$  is the damping constant,  $k$  is the spring constant and  $x$  is the displacement.

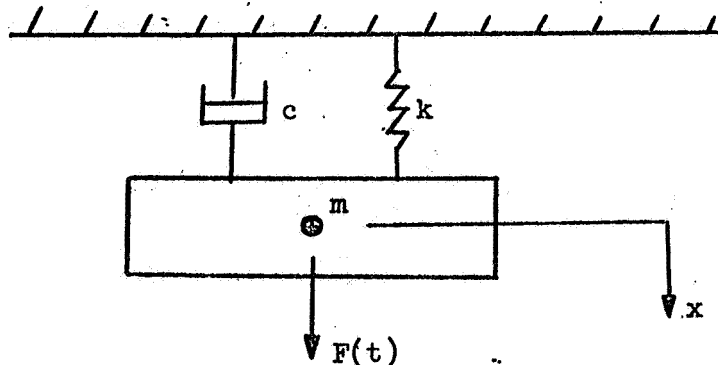


Figure 43 - Spring-Mass-Damper System

Dividing through by  $m$  and introducing

$$\omega_n^2 = k/m \quad ,$$

$$c_c = 2m\omega_n \quad ,$$

$$\zeta = c/c_c \quad ,$$

where  $\omega_n$  is the undamped natural frequency,  $c_c$  is the critical damping coefficient and  $\zeta$  is the damping factor, (I-1) becomes

$$\ddot{x} + 2\zeta\omega_n\dot{x} + \omega_n^2x = \frac{F(t)}{m} \quad . \quad (I-2)$$

We will first concentrate on the unit step solution. Specifying that  $F(t)/m = 1$  for  $t \geq 0$  and

$$x(0) = \dot{x}(0) = 0 \quad ,$$

the unit step solution of (I-2) becomes

$$x\omega_n^2 = 1 - e^{-\zeta\omega_n t} \left[ \frac{\zeta}{\sqrt{1-\zeta^2}} \sin \bar{\omega}t + \cos \bar{\omega}t \right] \quad , \quad (I-3)$$

where

$$\bar{\omega} = \omega_n \sqrt{1-\zeta^2} \quad . \quad (I-4)$$

$\bar{\omega}$  is the natural frequency of the damped system.

The maximum value of  $x\omega_n^2$  is found by differentiating (I-3) with respect to  $t$  and setting the result equal to zero:

$$\frac{d(x\omega_n^2)}{dt} = \sin \bar{\omega}t \left[ \omega_n / \sqrt{1-\zeta^2} \right] = 0 \quad . \quad (I-5)$$

The last relation is satisfied if

$$\bar{\omega}t = 0, \pi, 2\pi, \dots, \text{etc.}$$

For  $\bar{\omega}t = \pi$

$$t = t_1 = \pi / \omega_n \sqrt{1-\zeta^2} \quad , \quad (I-6)$$

and the maximum of (I-3) becomes

$$(x\omega_n^2)_{\max} = 1 + e^{-\pi\zeta / \sqrt{1-\zeta^2}} \quad . \quad (I-7)$$

The ratio,  $R$ , of the first maximum response to the steady-state value of (I-3) is

$$R = 1 + e^{-\pi\zeta / \sqrt{1-\zeta^2}} \quad . \quad (I-8)$$

Solving for the damping factor,  $\zeta$ , yields

$$\zeta = \left| \ln(R-1) / \sqrt{\pi^2 + \ln^2(R-1)} \right| \quad . \quad (I-9)$$

The natural frequency of the system,  $\omega_n$ , is obtained from (I-6)

$$\omega_n = \pi / t_1 \sqrt{1-\zeta^2} \quad , \quad (I-10)$$

where  $t_1$  is the time for the first maximum response. Thus, by knowing the maximum step response, the time at this maximum and the steady-state indicial response, the damping factor,  $\zeta$ , and the undamped natural frequency of the simple system,  $\omega_n$ , can be computed from (I-9) and (I-10).

The values of  $R$  range between 1 and 2.  $\zeta = 1$  at  $R = 1$  and the system is critically damped--producing no overshoot in the response curve.  $\zeta = 0$  at  $R = 2$  and the system contains no damping. For  $1 < R < 2$ , the response curve contains an overshoot and the system is underdamped.

We will now investigate the frequency response of the simple system. Specifying that

$$F(t) = F_0 \cos \omega t$$

in (I-1), then the steady-state solution is a sinusoidal oscillation of frequency  $\omega$  with amplitude  $x$  :

$$\frac{x}{x_0} = \frac{1}{\sqrt{\left[1 - \left(\frac{\omega}{\omega_n}\right)^2\right]^2 + \left[2\zeta \frac{\omega}{\omega_n}\right]^2}} \quad (\text{I-11})$$

where  $x_0 (= F_0/k)$  is the amplitude for  $\omega \rightarrow 0$ .

The maximum value of  $x/x_0$  is found upon differentiating (I-11) with respect to  $(x/x_0)$  and setting the results equal to zero. The location,  $\omega/\omega_n$ , for the maximum response is therefore

$$\omega/\omega_n = \sqrt{1-2\zeta^2} \quad (\text{I-12})$$

Substituting (I-12) into (I-11) yields

$$(x/x_0)_{\max} = 1/2\zeta \sqrt{1-\zeta^2} \quad (\text{I-13})$$

It should be noted that this last expression is only valid for  $\zeta < \sqrt{0.5}$ . In this case the amplitude response curves contain a resonant peak, while for  $\zeta \geq \sqrt{0.5}$  the amplitude response curves decrease steadily as  $\omega/\omega_n$  increases from zero, and  $(x/x_0)_{\max} = 1$  at  $\omega/\omega_n = 0$ .

Now setting

$$P = (x/x_0)_{\max} ,$$

the damping factor (for  $\zeta \geq \sqrt{0.5}$ ) is

$$\zeta = \sqrt{0.5 - 0.5 \sqrt{1 - 1/P^2}} , \quad (I-14)$$

and

$$\omega_n = \omega_1 / \sqrt{1 - 2\zeta^2} , \quad (I-15)$$

where  $\omega_1$  defines the location of  $(x/x_0)_{\max}$ . Thus, by knowing the maximum frequency response (and also the zero frequency response) and the frequency  $\omega_1$  at which this value occurs,\* the damping factor and undamped natural frequency of the system can be found from (I-14) and (I-15).

The expressions for the sinusoidal response characteristics are presented as a guide for testing the simple analogy to explain (or predict) the salient features of the more complex frequency responses presented in this report, from the corresponding indicial responses.

A numerical example is given below which shows a typical comparison between the simple analogy and the more complex aerodynamic frequency response behavior. The  $K = 5$  indicial and frequency response data of  $C_{M\alpha}$  for the  $\epsilon = 0.05$  ogive cylinder at  $M = 2$  are used in the example.

The indicial response data yield the following:

Steady state	$C_{M\alpha} = 3.7829$
Maximum	$C_{M\alpha} = 6.0497$
Time at maximum	$C_{M\alpha} = 0.0021 \text{ sec.}$

\* The frequency,  $\omega_1$ , at which the resonant aerodynamic frequency response occurs is known in this example. The unknown is  $\omega_n$ . This is opposite from the usual situation in which  $\omega_n$  is the known quantity.



From these, we calculate

$$R = 1.5992$$

$$\zeta = 0.1609$$

$$\omega_n = 1515.7 \text{ rad/sec}$$

The above values for  $\zeta$ ,  $\omega_n$  and steady state  $C_{M\alpha}$  were substituted into (I-11) and a predicted frequency response computed. The resulting single degree of freedom response is presented in Figure 44 compared to the actual frequency response of  $C_{M\alpha}$  (dashed curve).

From the actual frequency response data (see dashed curve in Figure 44), (I-14) and (I-15), the following are obtained:

Zero frequency (steady state)	$C_{M\alpha} = 3.7829$
Maximum	$C_{M\alpha} = 6.6972$
Frequency at maximum	$C_{M\alpha} = 1180 \text{ rad/sec}$
P	$= 1.7705$
$\zeta$	$= 0.2956$
$\omega_n$	$= 1299 \text{ rad/sec}$

The simple analogy gives a qualitative description of certain features of the aerodynamic responses. For this example, the simple analogy predicts a smaller damping factor and larger natural frequency than that found for the actual response. (The former is the reason for the larger resonance peak of the analogy.)

The most important result of the simple analogy approach is that it can be used fairly successfully to predict the gross behavior of the complicated aerodynamic frequency responses. It permits an interpretative bridge between the aerodynamic indicial and frequency response data.

$\epsilon = 0.05$  Ogive-Cylinder  $M = 2.0$   
 — Simple Spring - Mass Analogy Response  
 - - - Actual Aerodynamic Frequency Response

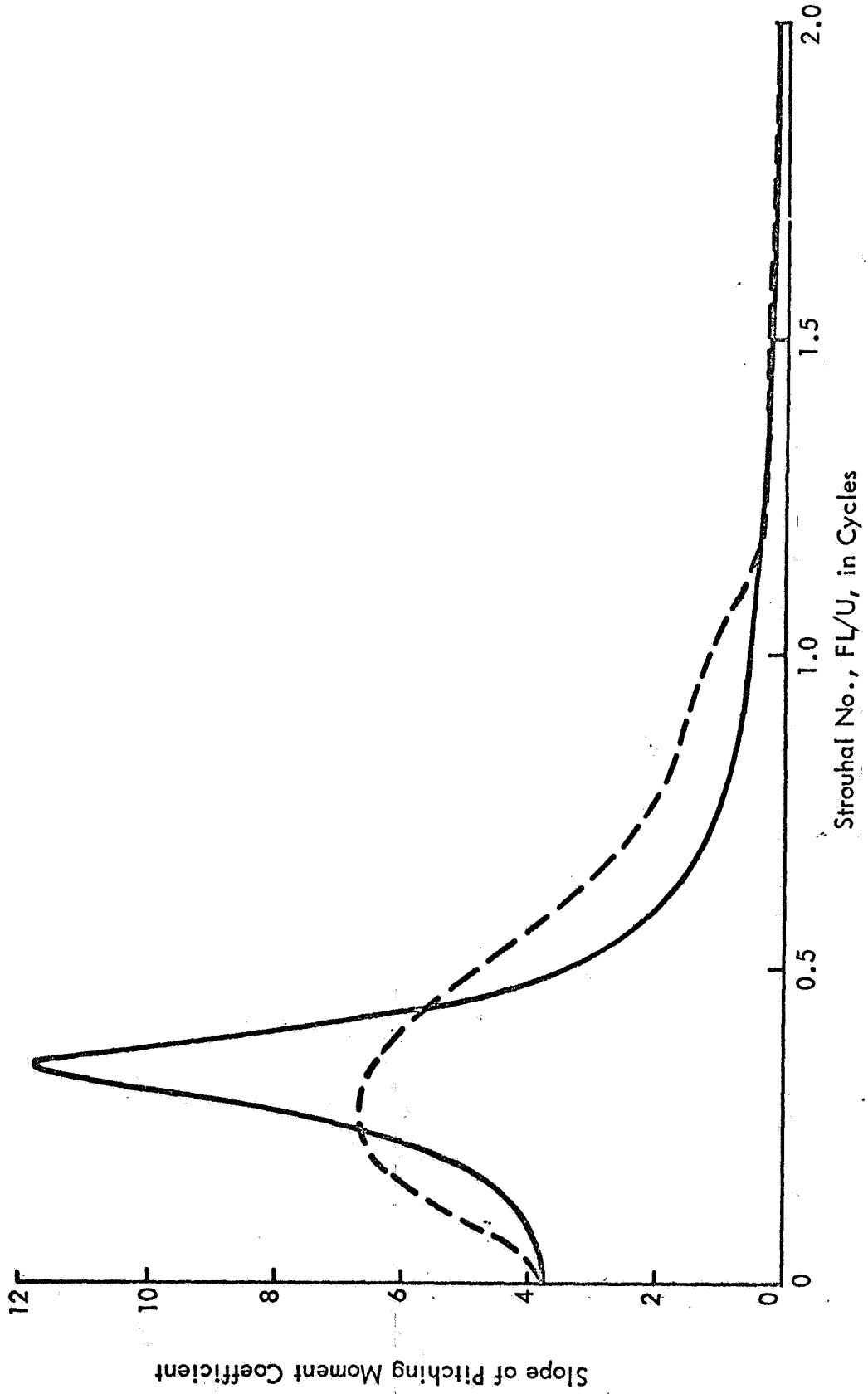


Figure 44 - Comparison of Frequency Response of Simple Spring-Mass Analogy with Actual Aerodynamic Frequency Response

The aerodynamic frequency response curves can be cast into two main types: (1) those curves which have a maximum response at zero impressed frequency ( $\zeta \geq \sqrt{0.5}$ ), and (2) those curves which have a resonance peak at a nonzero impressed frequency ( $\zeta < \sqrt{0.5}$ , i.e., underdamped). In general, the frequency response curves of the type 1 are associated with the indicial curves which reach steady-state values without undergoing an overshoot, while the type 2 curves are associated with the indicial curves which exhibit an overshoot. The simple analogy preserves this correspondence between the indicial and frequency responses. Thus, it is anticipated that the simple analogy can be successfully used, in conjunction with the indicial responses, to indicate those geometries and Mach number ranges for which frequency effects are important. Also, a rough indication of the first resonance frequency can often be obtained.

## APPENDIX II

### TECHNIQUE USED TO COMPUTE WIND SHEAR DATA

The computation of the aerodynamic response to an arbitrary wind profile (as presented in this report) requires that either the wind velocity or the indicial aerodynamics be differentiated once. It was established that, with care, the wind data<sup>16/</sup> could be differentiated once with adequate accuracy.\* Thus, the Duhamel integration for the response to the arbitrary wind profile was performed using the wind shears. (This is believed to be preferable to differentiating the aerodynamic data.)

During this project various approaches<sup>29-31/</sup> to the calculation of the wind shears were studied in detail. The technique chosen to compute the shears is presented in this Appendix along with some results used for substantiation. The wind data used are those documented in Ref. 16 which were obtained by employing the FPS-16 Radar/Jimsphere method. The data, which are presented at 25-meter altitude intervals, consist of zonal (W-E), meridional (S-N), scalar (magnitude of wind velocity), and wind direction profiles. Only the scalar winds were used in computing the wind shears in this study. The techniques presented below for calculating the wind shears are just as applicable to either the zonal or meridional wind components.

The wind shear data were computed by employing differentiation of a least squares quadratic curve fit of wind data.\*\* One example given here utilized a curve fit over eight successive data points (175-meter altitude intervals), while the other employed a curve fit (exact) over three successive data points (50-meter altitude intervals). The wind shears obtained from the eight-point fit will be discussed first.

The procedure followed will be to fit a least squares quadratic polynomial through eight successive wind velocity data points (given at 25-meter altitude increments). Upon differentiation of the polynomial, the wind shears will be computed only over the mid-interval of the seven intervals in the curve fit. The shears over the adjacent interval will be

---

\* This decision was reached early in the project as a result of a discussion with Dr. James Scoggins, formerly of the Aero-Astrodynamic Laboratory, MSFC, concerning the wind data listed in Ref. 16.

\*\* This technique implies that the shears may be considered to vary linearly with altitude over discrete 25-meter segments.

evaluated from a new curve fit obtained by advancing the approximation strip one increment. The process is to be repeated until the entire shear profile is computed.

Consider a typical wind distribution as shown in Figure 45.

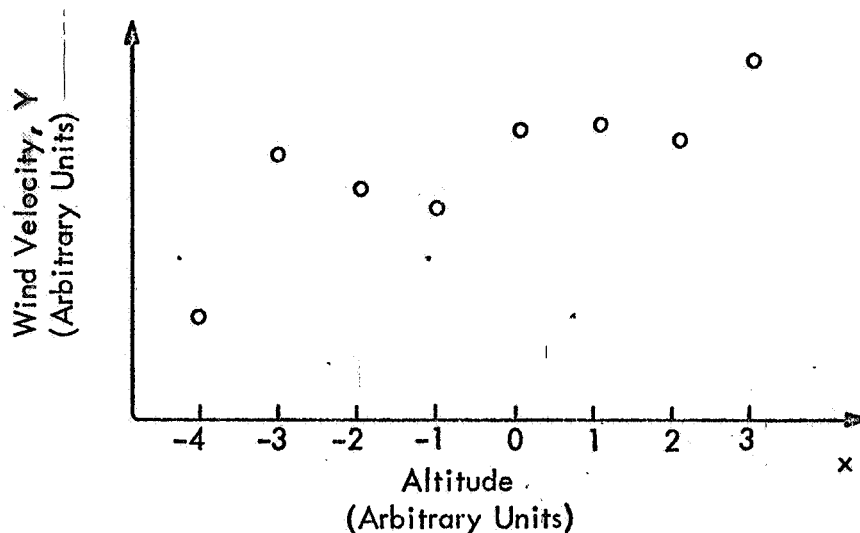


Figure 45 - Typical Wind Data for Eight-Point Fit

Some curve fitting techniques are particularly sensitive to numerical difficulty because of loss of significance. To avoid this pitfall it is best to reduce the magnitude spread of the data by an appropriate transformation. With this in mind, we will curve fit a modified form of the wind data given by

$$\bar{Y} = Y - NY \quad , \quad (II-1)$$

where

$$NY = \frac{Y(-4) + Y(3)}{2} \quad (II-2)$$

$NY$  is an average of the first and eighth wind velocity point.

Now assume that the resulting wind data can be curve fitted by

$$\bar{Y} = a\bar{x}^2 + b\bar{x} + c \quad , \quad (\text{II-3})$$

where the constants a, b, and c are determined by the method of least squares.<sup>31/</sup> The problem is to minimize  $\sum_1 (\bar{Y}_i - Y_i^*)^2$  where  $\bar{Y}_i$  are the actual data points (transformed wind speed) and  $Y_i^*$  are the curve fit points.

Thus, we need to minimize

$$\sum_1 [\bar{Y}_i - (a\bar{x}_i^2 + b\bar{x}_i + c)]^2$$

Differentiating, in turn, the above expression with respect to a, b, and c and setting the derivatives equal to zero yields the following:

$$ad = s_5(s_1s_3 - s_2^2) + s_6(s_1s_2 - 8s_3) + s_7(8s_2 - s_1^2)$$

$$bd = s_5(s_2s_3 - s_1s_4) + s_6(8s_4 - s_2^2) + s_7(s_1s_2 - 8s_3)$$

$$cd = s_5(s_2s_4 - s_3^2) + s_6(s_2s_3 - s_1s_4) + s_7(s_1s_3 - s_2^2)$$

$$s_1 = \sum_1 \bar{x}_i = -4$$

$$s_2 = \sum_1 \bar{x}_i^2 = 44$$

$$s_3 = \sum_1 \bar{x}_i^3 = -64$$

$$s_4 = \sum_1 \bar{x}_i^4 = 452$$

$$s_5 = \sum_1 \bar{Y}_i$$

(Eq. (II-4) concluded next page)

$$s_6 = \sum_1 \bar{x}_1 \bar{Y}_1$$

$$s_7 = \sum_1 \bar{x}_1^2 \bar{Y}_1$$

$$d = 8(s_2 s_4 - s_3^2) + 2s_1 s_2 s_3 - s_1^2 s_4 - s_2^3 = 56448 \quad (\text{II-4})$$

The standard error of the approximation is (in the case of eight data points)

$$E_{\text{RMS}} = \sqrt{\frac{\sum_1 \bar{Y}_1^2 - (as_7 + bs_6 + cs_5)}{7}} \quad (\text{II-5})$$

The curve fit is then written in terms of the actual wind ordinate values:

$$Y = ax^2 + bx + c + NY \quad (\text{II-6})$$

Now, transforming (II-6) to actual altitude stations,  $x_i$ , and noting that  $x_i - x_{i-1} = \Delta h = 25$  meters, yields

$$Y = Ax^2 + Bx + C \quad (\text{II-7})$$

where

$$A = \frac{a}{625}$$

$$B = \frac{b}{25} - \frac{2ax_5}{625}$$

$$C = c - \frac{bx_5}{25} + \frac{ax_5^2}{625} + NY \quad (\text{II-8})$$

The wind shear is found from (II-7):

$$\frac{dY}{dx} = Y' = 2Ax + B \quad , \quad (\text{II-9})$$

and is evaluated only over the midrange of the approximation (i.e.,  $x_4 \leq x \leq x_5$ ).

This approach gives rise to a double-valued wind shear at the beginning and end of each 25-meter altitude increment. In order to produce a continuous wind shear profile, straight line segments are used to connect the average shear at the midpoint of each 25-meter increment (see Figure 46).

This technique was tested by evaluating the wind shears over the 8.2 km. to 10 km. altitude range from the FPS-16 Radar/Jimsphere wind profile test number 2579 (27 April 1965).<sup>16/</sup> The midpoint shears were then integrated over a portion of this altitude range and the results compared to the original wind data. In general, the integrated wind shears and the RMS error associated with the quadratic curve fits were in the order of 0.1 to 0.3 m/sec which is the order of error reported for the tabulated data. (In a few isolated instances the RMS error of the approximation was as high as 0.6 to 0.8 m/sec.)

Another technique of curve fitting the wind data was undertaken because of (1) the arbitrary manner in which the eight-point wind shears were joined to produce a continuous shear profile; (2) the occasional high RMS error; and (3) the loss of high frequency components of the wind profile. This second technique, or three-point curve fit, was the one ultimately used in the wind response program. In this instance, a quadratic curve is fitted (exactly) over three successive data points (50-meter altitude intervals).

Consider a typical wind distribution as shown in Figure 47.



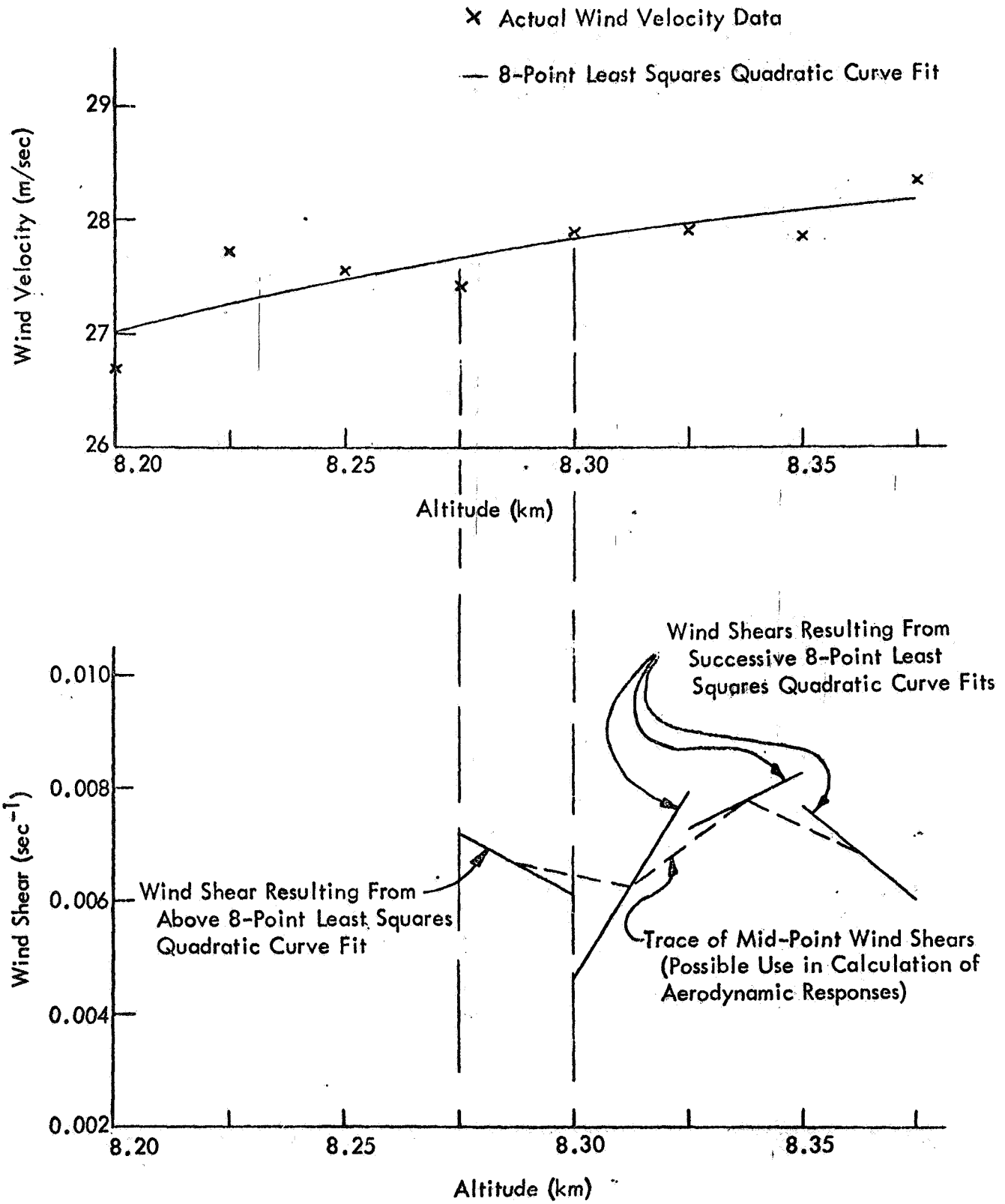


Figure 46 - Procedure Used to Calculate 8-Point Curve Fit Wind Shears

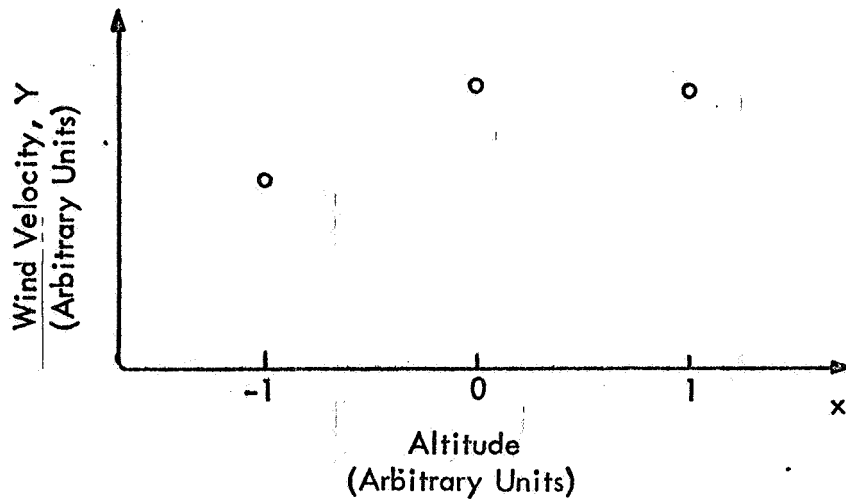


Figure 47 - Typical Wind Data for Three-Point Fit

Again let

$$\bar{Y} = Y - NY \quad , \quad (\text{II-10})$$

where

$$NY = \frac{Y(-1)+Y(1)}{2} \quad . \quad (\text{II-11})$$

Now assume that the resulting wind data can be curve fitted by

$$\bar{Y} = ax^2 + bx + c \quad , \quad (\text{II-12})$$

where the constants are evaluated as

$$a = \frac{Y(-1) - 2Y(0) + Y(1)}{2} ,$$

$$b = \frac{Y(0) - Y(-1)}{2} ,$$

and

$$c = Y(0) - NY \quad . \quad (II-13)$$

Now, transforming (II-12) to actual altitude stations,  $x_1$ , and noting that  $x_1 - x_{1-1} = \Delta h = 25$  meters, yields

$$Y = Ax^2 + Bx + C \quad , \quad (II-14)$$

where

$$A = \frac{a}{625} ,$$

$$B = \frac{b}{25} - \frac{2x_2 a}{625} ,$$

and

$$C = c - \frac{bx_2}{25} + \frac{ax_2^2}{625} + NY \quad . \quad (II-15)$$

The wind shear is found from (II-14) upon differentiation with respect to altitude,  $x$  :

$$\frac{dY}{dx} = Y' = 2Ax + B \quad , \quad (II-16)$$

and is valid for the interval range  $x_1 \leq x \leq x_3$ . The wind shear midway between  $x_1$  and  $x_2$  is

$$Y' = A(x_1+x_2) + B \quad (\text{II-17})$$

and midway between  $x_2$  and  $x_3$  is

$$Y' = A(x_2+x_3) + B \quad (\text{II-18})$$

The wind shears obtained from the three-point fit were computed over the midrange of the curve fits, i.e., between the one-quarter and three-quarter points (see Figure 48). The shears over the adjacent interval were evaluated similarly from a curve fit obtained by advancing the approximation strip one increment. A continuous wind shear profile is thus automatically obtained from the three-point curve fit techniques. (It can be proven that the shear at the three-quarter point of one curve fit is equal to the shear at the one-quarter point of the curve fit for the adjacent interval.)

The three-point curve fit wind shears were also computed over an altitude range of 8.2 km. to 10 km. using the FPS-16 Radar/Jimsphere wind profile test number 2579 (27 April 1965). These shears were then integrated and compared to the original wind data. A comparison of the integrated three-point curve fit shears with the actual wind data is shown in Figure 49. It can be seen that the agreement is excellent. The errors of the approximation are equal to or less than the 0.3 m/sec RMS error reported for the original wind data.

In comparing the two techniques, the eight-point curve fit shears did produce a smoother wind profile when integrated than did the three-point curve fit results. In this respect the eight-point curve fit will tend to inadvertently filter out some of the desired higher frequency components of the wind profile. (This filtering would be in addition to that already done in reducing the raw wind data obtained by the FPS-16 Radar/Jimsphere method.)<sup>29,30</sup> As a consequence, the three-point method of computing the wind shears is believed to be superior to the eight-point technique, and was used in this study.

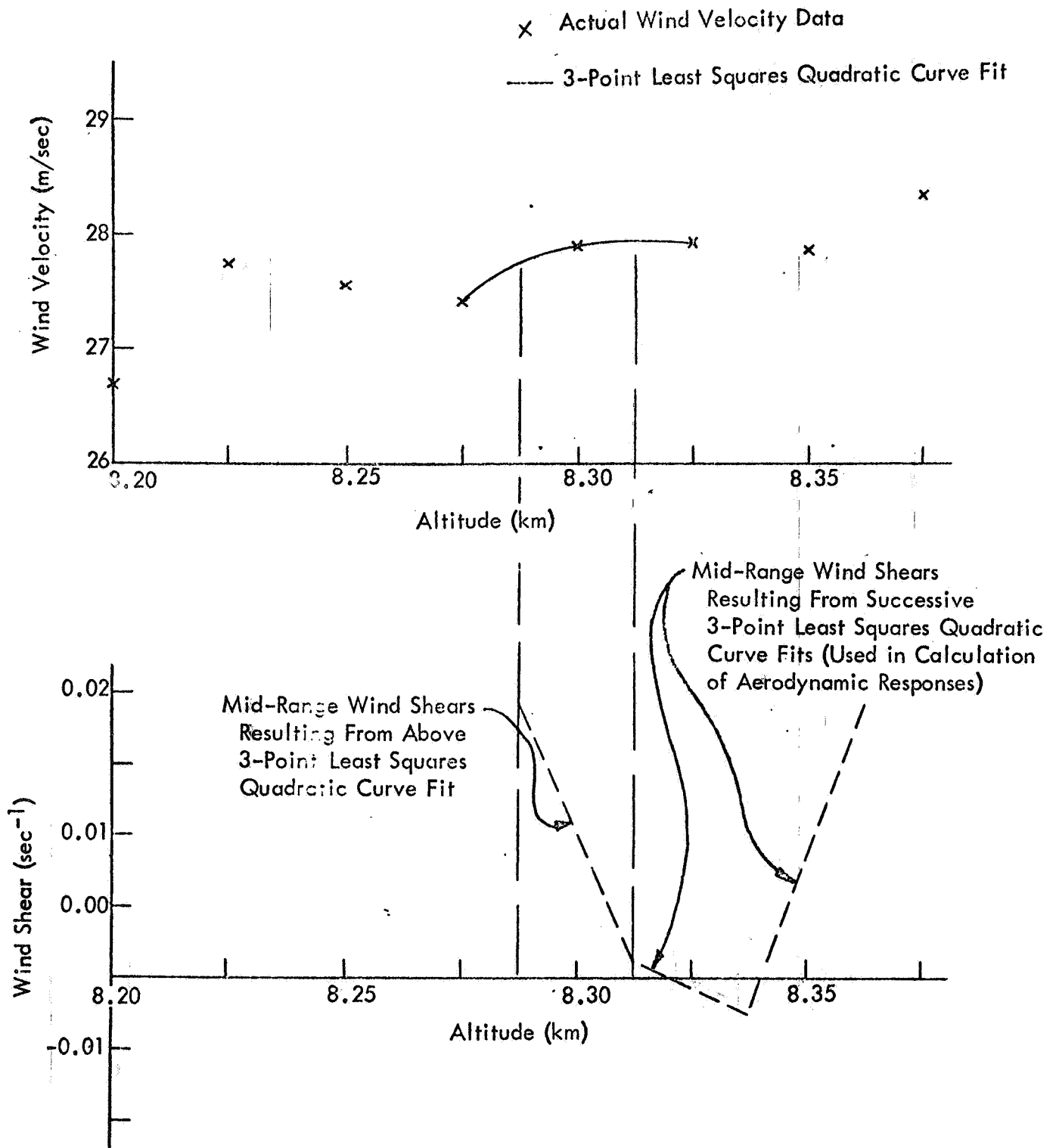


Figure 48 - Procedure Used to Calculate 3-Point Curve Fit Wind Shears

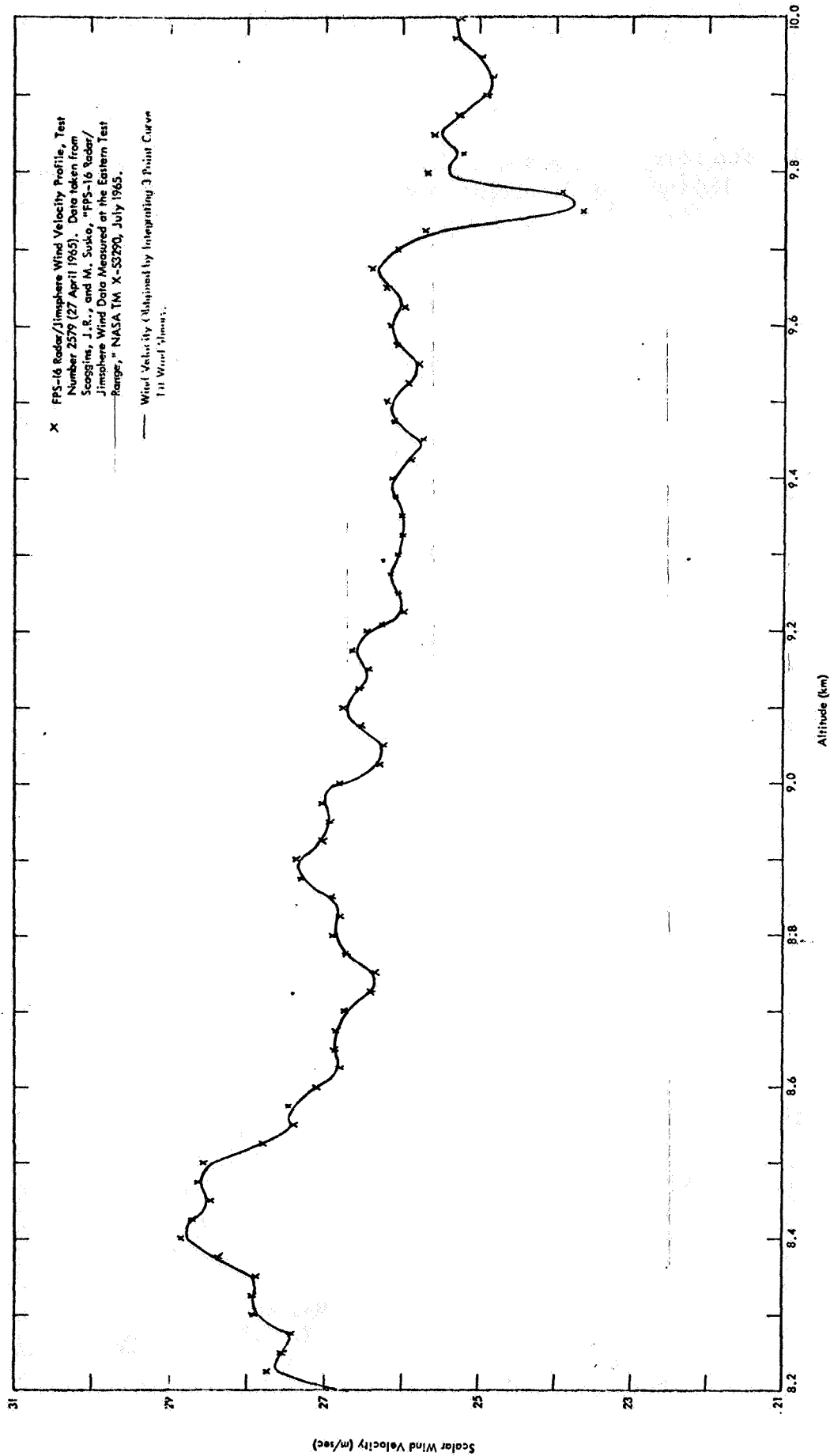


Figure 49 - Comparison of Integrated 3-Point Curve Fit Wind Shears with Actual Wind Data

## BIBLIOGRAPHY

1. Von Karman, Th., and N. B. Moore, "Resistance of Slender Bodies Moving with Supersonic Velocities, with Special Reference to Projectiles," Trans. ASME, 54, 303-310 (1932).
2. Tsien, H. S., "Supersonic Flow over an Inclined Body of Revolution," J. Aero. Sci., 5, 480-483 (1938).
3. Van Dyke, M. D., "First- and Second-Order Theory of Supersonic Flow Past Bodies of Revolution," J. Aero. Sci., 18, 161-178 (1951).
4. Lighthill, M. J., "Supersonic Flow Past Slender Bodies of Revolution the Slope of Whose Meridian Section is Discontinuous," Quart. J. Mech. and Appl. Math., I, 90-102 (1948).
5. Adams, M. C., and W. R. Sears, "Slender Body Theory - Review and Extension," J. Aero. Sci., 20, No. 2, 85-98, February, 1953.
6. Platzer, M. F., and G. H. Hoffman, "Quasi-Slender Body Theory for Slowly Oscillating Bodies of Revolution in Supersonic Flow," NASA TN D-3440, June 1966.
7. Platzer, M. F., "Aerodynamic Pitch Damping of Slowly Oscillating Pointed Bodies of Revolution in Linearized Supersonic Flow," George C. Marshall Space Flight Center, MTP-Aero-63-62 (1963).
8. Miles, J. W., The Potential Theory of Unsteady Supersonic Flow, Cambridge University Press (1959).
9. Yates, J. E., "Transient Aerodynamic Loading on Multi-Stage Missiles," Paper presented at the IAS National Summer Meeting, Los Angeles, California, 19-22 June 1962, IAS Paper No. 62-93.
10. Blackburn, R. R., and A. D. St. John, "Study for the Indicial Load Effects on Multi-Stage Space Vehicle Systems," Vol. II, "Effects and Importance of Penetration and Growth of Lift on Space Vehicle Response," Annual Summary Report, 21 June 1963 - 20 August 1964, Contract No. NAS8-11012, MRI Project No. 2715-P. (Also, NASA CR-326)
11. Strang, W., "Transient Source, Doublet, and Vortex Solutions of the Linearized Equations of Supersonic Flow," Proc. Roy. Soc. A, 202, 40-53 (1950).

12. Glauz, W. D., "Study for the Indicial Load Effects on Multi-Stage Space Vehicle Systems," Vol. I, "Linearized Indicial Aerodynamic Forces on Bodies of Revolution in Supersonic Flow," Annual Summary Report, 21 June 1963 - 20 August 1964, Contract No. NAS8-11012, MRI Project No. 2715-P.
13. Glauz, W. D., "Study for the Indicial Load Effects on Multi-Stage Space Vehicle Systems," Final Report, 20 September 1964 - 20 September 1965, Contract No. NAS8-11012, MRI Project No. 2715-P.
14. Glauz, W. D., and G. Coombs, "Users Manual for the Indicial Aerodynamics Computer Program," 24 September 1965, Contract No. NAS8-11012, MRI Project No. 2715-P.
15. Glauz, W. D., and G. Coombs, "Study of Indicial Aerodynamic Forces on Multi-Stage Space Vehicle Systems, Vol. II: Users Manual for the Aerodynamics Computer Programs," Final Report, 28 June 1967 - 27 September 1968, Contract No. NAS8-21167, MRI Project No. 3089-P.
16. Scoggins, J. R., M. Susko, "FPS-16 Radar/Jimsphere Wind Data Measured at the Eastern Test Range," NASA TMX-53290, July 1965.
17. Glauz, W. D., "Unsteady Aerodynamic Forces on Multi-Stage Space Vehicles," Paper presented at the AIAA Guidance, Control and Flight Dynamics Conference, Huntsville, Alabama, 14-16 August 1967, AIAA Paper No. 67-610.
18. Glauz, W. D., and R. R. Blackburn, "Study for the Indicial Load Effects on Multi-Stage Space Vehicle Systems," Final Report, 20 September 1965 - 20 December 1966, Contract No. NAS8-11012, MRI Project No. 2715-P.
19. Van Dyke, M. D., "Practical Calculation of Second-Order Supersonic Flow Past Nonlifting Bodies of Revolution," NACA TN 2744.
20. Air Load Manual, Saturn V Three Stage to Escape (LOR), prepared by Aerodynamics Division, Aero-Astrodynamic Laboratory, George C. Marshall Space Flight Center, NASA.
21. Tobak, M., "On the Use of the Indicial Function Concept in the Analysis of Unsteady Motions of Wings and Wing-Tail Combinations," NACA Report 1188, 1954.
22. Sims, J. L., "Supersonic Flow Around Right Circular Cones, Tables for Small Angle of Attack," NASA TN D-2004, 1964.



23. Tobak, M., and W. R. Wehrend, "Stability Derivatives of Cones at Supersonic Speeds," NACA TN 3788, September 1956.
24. Brong, E. A., "The Unsteady Flow Field about a Right Circular Cone in Unsteady Flight," Technical Report FDL-TDR-64-148, General Electric Company, January 1967. (Also AIAA Paper No. 65-398).
25. Sims, J. L., unpublished results, Aero-Astroynamics Laboratory, George C. Marshall Space Flight Center, Huntsville, Alabama.
26. Platzer, M. F., and A. D. Sherer, "A Linearized Characteristics Method for the Dynamic Stability Analysis of Bodies of Revolution in Supersonic Flow," AIAA Paper No. 67-607, presented at the AIAA Guidance, Control, and Flight Dynamics Conference, Huntsville, Alabama, 14-16 August 1967.
27. Bond, R., and B. B. Packard, "Unsteady Aerodynamic Forces on a Slender Body of Revolution in Supersonic Flow," NASA TN-D-859, May 1961.
28. Taken from data furnished by Richard Beranek, NASA-MSFC, Aero-Astroynamics Laboratory.
29. Scoggins, J. R., "Sphere Behavior and the Measurement of Wind Profiles," NASA TN D-3994, June 1967.
30. Jacobs, D. B., "Data Reduction Methods - FPS-16 Radar/Jimsphere," Boeing Document D5-15564, October 1966.
31. Hershey, H. C., J. L. Zakin, and R. Simha, "Numerical Differentiation of Equally Spaced and Not Equally Spaced Experimental Data," Industrial and Engineering Chemistry Fundamentals, Vol. 6, No. 3, August 1967.